Dottorato in Ingegneria Elettrica XXI Ciclo
Università Sapienza di Roma

Tesi di Dottorato

Tecniche di protezione da interferenze elettromagnetiche: modellistica e prove sperimentali in camera riverberante

EMI protection techniques: modelling and experimental testing in reverberation chamber

Dottoranda
Sandra Greco

Tutor
Prof. Maria Sabrina Sarto

Contents

Chapter 1

Introduction

Shielding effectiveness and electromagnetic protection Graf, W.; Vance, E.F. Electromagnetic Compatibility, IEEE Transactions on Volume 30, Issue 3, Aug 1988 Page(s):289 - 293 Digital Object Identifier 10.1109/15.3307

Electromagnetic interference and compatibility are problems that claim an increasing attention in many environments, all over the world. For electromagnetic interference it is intended a phenomenon that can occur when an electronic device undergoes the influence of an electromagnetic field, which may cause temporary or definitive malfunctioning of the device itself. Indeed, electromagnetic compatibility is the capacity of an electric device either to operate normally, without generating electromagnetic disturbances that may interfere with other devices or to operate without being influenced by electromagnetic field generated by other electric devices.

Electromagnetic fields have increased tremendously over the last decade and now distress more and more people. Electromagnetic radiation comes from mobile phones, wireless phones, wireless networks, microwave ovens, base stations, radio- and TV transmitters, radar systems, military surveillance and communication systems, high voltage lines, transformer stations, heating cables, electrical equipment, clock radios, low voltage lamps, computers and TVs, to mention the most common ones.

I disturbi dovuti alla compatibilità elettromagnetica possono essere distinti tra necessari ed inevitabili. Un esempio dei primi è il telefono cellulare, che quando si usa genera un'onda radio necessaria per il suo funzionamento. Quando invece il frigorifero stacca il compressore, si genera un picco di corrente ed un disturbo che non è necessario per la funzionalità del frigorifero ma è inevitabile. Per regolamentare l'esposizione ai campi elettromagnetici organismi internazionali come l'International Commission on Non-Ionizing Radiation Protection (ICNIRP), l'American National Standard Institutes (ANSI) e in Europa il Comitato per la Normalizzazione Elettrotecnica (CENELEC), hanno stabilito dei livelli limite di esposizione umana.

More and more aspects of our lives depend on the uninterrupted operation of electronic equipment and appliances. ”Drive by wire” and ”fly by wire” have become everyday realities. In automated plants especially, electronic equipment that fails to operate correctly can cause enormous damage.

The ideal electronic circuit should be free of active EMI (electromagnetic interference, also called RFI or radio frequency interference) sources and passively immune to disturbances from outside.

The task of minimizing active sources is probably easier than that of protection against interference. Common techniques are line filtering, power-supply design, proper layout, and shielding of the enclosure.

Electrical disturbances can be conducted by the power lines or conveyed through the air by capacitive, magnetic, or electromagnetic radiation. Most difficult to cope with (usually) is the interference conducted over signal lines connected to the equipment. In any case, one must distinguish between the need to protect against damage or malfunction, and the need to prevent signal or data distortion resulting from (for example) a disruption in the sequence of a microcontroller program. The first problem is attacked via hardware design, the second via software algorithms.

The scope of this chapter is to introduce reverberation chamber test facilities. In particular, peculiar aspects, parameters and statistics concerning the use of reverberation chambers are discussed and commented. In the following, the realization starting from a shielded room, the calibration and testing of the reverberation chamber of the EMC Lab of the Department of Electrical Engineering of the University of Rome “La Sapienza,” are fully detailed. Some problems encountered during the chamber realization, along with the adopted solutions are also described.

In Chapter 3, it is described as the existing shielded room of the EMC laboratory of the Department of Electrical Engineering of the University of Rome “La Sapienza,” was transformed into a low-Q reverberation chamber in order to perform EMC tests in an aircraft-like electromagnetic environment. The Q-factor was intentionally lowered to reproduce the typical electromagnetic environment aboard aircraft. The performances of the chamber were evaluated when an amplitude modulated signal excites the cavity.

Chapter 4 describes an innovative procedure for the characterization of a field sensor in an aircraft-like EM environment. The sensor prototype under investigation is sensitive only to amplitude modulated signals and it has been designed to be installed as sensing unit in an intelligent network for the localization of GSM cell phones operating aboard without authorization. The EM environment is simulated by means of a low-Q reverberation chamber as described in the previous chapter. The response of the sensor, expressed by the activation probability in a given operating condition, is obtained as a function of frequency, voltage supply, and incident field level.

The Chapter presents a new method for the measurement of the shielding effectiveness of geometrically “small”, but electrically “large” enclosures. The proposed technique implements a hybrid mode-stirring technique on nested reverberation chambers. Correction factors are considered to account for the effect of the inner chamber on the radiating antenna. Numerical simulation of a 0.3 m^3 box are carried out in order to investigate the feasibility of frequency-stirring the modes inside the enclosure and to excite a correct number of modes. At least, the the use of the nested RC hybrid approach is applied to evaluate the EM shielding performance of a small satellite, simulated by means of a nested chamber loaded with an increasing number of lossy units.

ITO transparent

Chapter 7 describes an equivalent circuit approach for the analysis and the electromagnetic design of innovative thin absorbers. The use of thin bilayers of metamaterials as spacer in dielectric Salisbury screen is discussed. It is demonstrated that narrow-band thin absorbers can be obtained using both positive and negative materials, whereas broad-band thin absorbing screen can be realized only with bilayer of epsilon-negative and mu-negative materials. An optimization tool based on genetic algorithms is developed in order to design electrically thin absorbing screens including metamaterials for electromagnetic interference suppression. The optimization procedure is fully detailed and some design solutions of sub-wavelength screens are proposed.

Chapter 2

Reverberation Chambers

The scope of this chapter is to introduce reverberation chamber test facilities. In particular, peculiar aspects, parameters and statistics concerning the use of reverberation chambers are discussed and commented. In the following, the realization starting from a shielded room, the calibration and testing of the reverberation chamber of the EMC Lab of the Department of Electrical Engineering of the University of Rome “La Sapienza,” are fully detailed. Some problems encountered during the chamber realization, along with the adopted solutions are also described.

2.1 Introduction

The increasing use of wireless communication systems introduces more and more problems related to the EMC of apparatus and systems. Analytical and experimental procedures should be developed in order to characterize the radiated susceptibility and immunity level of electronic devices and equipment operating in a complex electromagnetic environment. Traditional test methods are no longer efficient [1]. In fact, the properties that characterize the EM environment in anechoic chambers and open-test-sites, like far-field distribution, single polarization, plane wave configuration and direct coupling, do not apply to the practical operating conditions of electronic devices in the presence of wireless communication systems. At the contrary, testing into a reverberation chamber (RC) is more consistent than traditional procedures due to the presence of a more realistic EM environment [2], [3]. Actually, the characteristics of the EM field configuration in an RC in over-moded excitation, such as the isotropy, the random field polarization and the spatial uniformity, are much closer to the real operating situation. Radiated susceptibility (RS), radiated emission (RE) and shielding effectiveness (SE) tests can be performed in RC in order to investigate the EM interference and the immunity of the devices under test (DUT) [4].

The IEC 61000-4-21 is a comprehensive document covering both mode-tuned and mode-stirred procedures [5]. It has been developed by a joint task-force between the SC77B and CISPR Committees. This standard provides the calibration procedure of RCs, along with the measurement method for the immunity, radiated emission and shielding effectiveness effectiveness. Inside a RC the exciting field statistically comes from any possible direction, with any possible polarization and phase. This method is robust against DUT positioning and orientation inside the working volume.

2.2 Preliminary considerations

A reverberation chamber is an electrically large, highly conductive enclosed cavity or chamber used to perform electromagnetic (EM) measurements (both emissions and immunity) on electronic equipment. Any facility that fits this description can be considered a reverberation chamber (also called a mode-stirred chamber). Other conditions, however, may be required before such a facility can be used with acceptable uncertainty. In general, a reverberation chamber is a shielded enclosure with the smallest dimension being large with respect to the wavelength at the lowest useable frequency (LUF). The chamber is normally equipped with a mechanical tuning/stirring device whose dimensions are a significant fraction of the chamber dimensions and of the wavelength at the LUF. When the chamber is excited with RF energy, the resulting multi-mode electromagnetic environment can be “stirred” by the mechanical tuner/stirrer. The resulting environment is statistically uniform and statistically isotropic (i.e., the energy having arrived from all aspect angles and at all polarizations) when averaged over a sufficient number of positions of the mechanical tuner/ stirrer. By “sufficient number” we mean the number of tuner steps required to give the specified field uniformity. To achieve a statistically uniform and statistically isotropic environment also, means other than mechanical tuners may be acceptable. The chamber mode density and the effectiveness of the mechanical tuner/stirrer determine the LUF. The LUF is generally accepted to be the frequency at which the chamber meets operational requirements. This frequency generally occurs at a frequency slightly above three times the first chamber resonance. In practice the chamber size, tuner/stirrer effectiveness and the chamber quality factor determine the lowest useable frequency. For the reverberation chamber procedure described in the CISPR standard, the LUF is the lowest frequency at which, the specified field uniformity can be achieved over a volume defined by an 8-location calibration data set [5].

Quality factor is used to describe the ability of a chamber or cavity to store energy. The ability of a chamber to store energy is determined by the losses present in the chamber. The dominant loss in an empty chamber is the chamber walls. The higher the conductivity of the materials used to construct the chamber walls the lower the chamber losses. Materials such as copper and aluminium sheet offer the highest conductivity and therefore the lowest losses. Other materials such as bare or painted steel or galvanized sheet are also common. Copper and aluminium screen and flame spray, however, have large surface areas and do not result in high Q environments. Additional losses such as antennas, support structures and the equipment under test (EUT) also can affect the overall Q of the chamber.

The chamber input power (P_{Input}) is normally taken to be the forward power delivered to the antenna terminals. In some cases it is necessary to take into account the reflected power caused by antenna/excitation induced mismatch. In such cases the input power shall be the net input power which is equal to:

$$P_{\text{Net}} = P_{\text{Forward}} - P_{\text{Reflected}} \tag{2.1}$$

The amount of power needed to generate a specific field inside a chamber can be determined from the empty chamber calibration. However, the EUT, the required support equipment or any absorbing material present may load the chamber, reduce the chamber Q and hence reduce the test fields for the same input power. Therefore, the fields in a loaded chamber must be monitored and input power increased, if necessary, to compensate for this loading.

The tuners/stirrers should be adequate to provide the desired field uniformity. In some chambers, it may be necessary to use multiple tuners/stirrers to obtain the desired field uniformity at the required frequencies. Stepping motors or encoder-equipped servo-motors with computer control are recommended. Variable speed, continuous motors are acceptable, but the time response of the EUT must be fast relative to tuner/stirrer speed for this option to be viable. In the past, testing was performed using 200 samples or steps of the mechanical tuner. This resulted in uncertainties (i.e., statistical inhomogeneity) in the field that varied as a function of frequency due to the increase in modal density at the higher frequencies. The uncertainty for a typical chamber varied considerably as a function of frequency as the number of tuner steps remained constant. A chamber that passes the calibration procedure will have demonstrated its ability to generate the required field uniformity.

2.2.1 Cavity theory and reverberation chamber statistics

The modes in a cavity are determined by the boundary conditions. For an ideal, lossless, empty, rectangular cavity of dimensions L (length), W (width), and H (height), the mode frequencies $F_{l,m,n}$ in MHz, can be shown to be.

$$F_{l,m,n} = 150\sqrt{\left(\frac{l}{L}\right)^2 + \left(\frac{m}{W}\right)^2 + \left(\frac{n}{H}\right)^2} \tag{2.2}$$

where l, m, and n are the mode indices, and L, W, and H are the chamber dimensions in meters. Each mode represents a unique field variation (modal structure) as a function of spatial location throughout the cavity. The cavity quality factor bandwidth, BWQ, is defined as $F_{l,m,n}/Q$ at the 3 dB points of a second order distribution. Additional modes can be excited when the cavity is driven at the frequency of the 60th mode. The effective modal structure would be the vector sum of the excited modes with different amplitudes.

The spatial field variation will be different than that obtained with the higher Q cavity. Thus varying the cavity Q can change the “effective” modal structure. Note that if the frequency were increased, more modes would be available within a given BWQ (i.e., correlated). Again, the effective modal structure would be the vector sum of the modes. At the lower frequencies the modal population of a chamber is sparse. Also, as frequency is increased the number and density of the modes increases. The effective modal structure combined with the ability of the tuner to change the boundary conditions of the chamber determines how well a chamber will perform.

Chamber may be any arbitrary geometry. However, some shapes, such as spherical and circular cylindrical, are generally not used for reverberation chambers; because the curved surfaces can produce caustics (focusing of rays) that make it difficult to obtain spatial field uniformity.

The effective modal structure depends on both the theoretical mode density and the quality factor bandwidth at the frequency of interest. The number of modes, M, excited in a BWQ can be estimated by

$$M = \frac{8\pi V f^3}{c^3 Q} \tag{2.3}$$

where f is the frequency, in Hz, and V, is the cavity volume, in m^3. M is independent of the shape of the cavity. Second-order corrections to 2.3 for relatively low frequencies can be calculated for chambers of arbitrary geometry and are proportional to f. Theories at present suggest that an “overmoded” condition exists when a sufficient number of modes are excited. In the overmoded condition, the power distribution has been shown to fit a chi-squared (χ^2) distribution. At lower mode densities, the distributions of received power do not fit the χ^2 distribution but a more complicated compound exponential distribution.

Usually it is not practical to define a minimum size test chamber valid for every chamber. The critical factor is that if a chamber fulfils the calibration procedure, then this demonstrates that it will provide the required electromagnetic environment at the desired level of statistical confidence.

It has been experimentally validated that the fields in a reverberation chamber can be theoretically predicted using the appropriate statistical models. These models define distribution functions for

1. the received power by an antenna which is related to the chamber scalar power density and the electric field squared
2. the maximum received power or the maximum electric field squared
3. a rectangular component of the electric field
4. the maximum of a rectangular component of the electric field

These four distributions are different but relatable. There will be no attempt to cover reverberation chambers statistics in detail in this thesis although some specific properties of some of the distributions will be discussed below.

The function of a reverberation chamber is to generate a statistically uniform (i.e., statistically isotropic) test environment within acceptable uncertainty and confidence limits. This can be accomplished both mechanically and electronically. In particular, the RC of the EMC LAb was initially realized by introducing a mechanical tuner, into a shielded room, which is used to redistribute the field energy. The tuner is used to changes the boundary conditions within the chamber when it is moved or rotated. Once the tuner has been moved to a sufficient number of independent positions, the field variations resulting from rotating the tuner provide a set of fields covering almost all directions and polarizations. This implies that the magnitude and directionality of the fields was the same, within bounded uncertainty limits, for all points within the chamber.

The term “isotropic” is often used to refer to the environment generated by a reverberation chamber. This term is somewhat misleading since the environment did not arrive with equal magnitude from all directions and polarizations simultaneously. For this reason, the term should be used with caution when referring to reverberation chambers. For the following discussion, it is assumed that the chamber dimensions are large compared to the excitation wavelength (the chamber is overmoded and that the chamber has a complex geometry and configuration.

The introduction of antennas and tuners assure the required complexity in an otherwise regular cavity. The discussion is restricted to the fields within the working volume of the chamber. The working volume is defined as being at least at distance of $\lambda/4$ from the chamber walls and from any antenna, tuner, or other object at the lowest frequency of operation. For a chamber operating above 100 MHz, this would be 0.75 m. Anyway, the actual working volume can be defined only by the chamber calibration procedure, and is the volume in which the EM field respects given limits and statistics.

Since multipath scattering changes the phase and rotates the polarization many times, angular spectrum components with orthogonal polarizations or quadrature phase ought to be uncorrelated.

The statistical assumption for the angular spectrum have been used to derive a number of useful ensemble averages for the electric field properties and for antenna response [**?**]. These results have not required a knowledge of the particular form of the probability density function. However, such knowledge would be very useful for analysis of measured data which is always based on some limited number of samples due to stirrer positions. To derive the electric field probability density function we have to write the rectangular components in terms of their real and imaginary parts:

$$E_x = E_{xr} + E_{xi}, E_y = E_{yr} + E_{yi}, E_z = E_{zr} + E_{zi} \tag{2.4}$$

The mean value of all the real and imaginary part in (2.5) is zero [?]. The variance of the real and imaginary part can be shown to be [?]:

$$< E_{xr}^2 >=< E_{xi}^2 >=< E_{yr}^2 >=< E_{yi}^2 >=< E_{zr}^2 >=< E_{zi}^2 >= \frac{E_0^2}{6} = \sigma^2 \tag{2.5}$$

In [?], since the real and imaginary part of the rectangular components of the electric field have been shown to be normally distributed with zero mean and equal variance and are independent, then the probability density function of various electric field magnitudes or squared magnitudes are χ or χ^2 distributions with the appropriate number of degrees freedom.

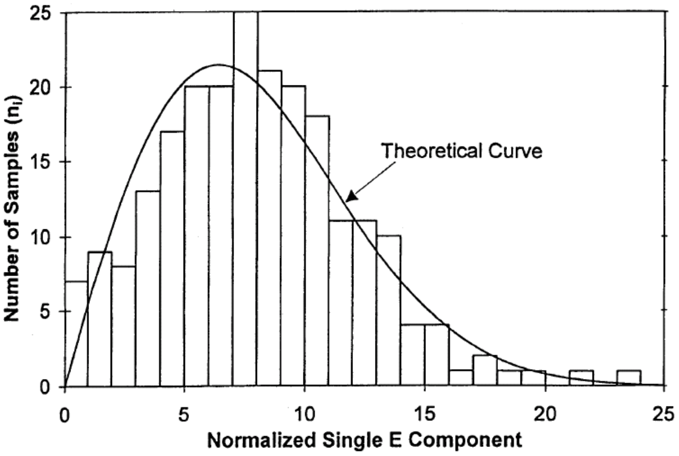

Figure 2.1: Comparison of the measured probability density function of a single rectangular component of the electric field with Rayleigh distribution.

The magnitude of any of the electric field components, is χ distributed with two degrees of freedom and consequently has a Rayleigh distribution:

$$f(|E_x|) = \frac{|E_x|}{\sigma^2} \exp\left[-\frac{|E_x|^2}{2\sigma^2}\right] \tag{2.6}$$

. Figure 2.1 shows a comparison of equation (2.6) with the measured data taken at 1 GHz in the NASA chamber [6]. The square magnitude of any of the electric field components, for example $|E_x|^2$ is χ^2 distributed with two degrees of freedom, and consequently it has an exponential distribution:

$$f(|E_x|^2) = \frac{1}{2\sigma^2} \exp\left[-\frac{|E_x|^2}{2\sigma^2}\right] \tag{2.7}$$

Kostas and Boverie [7] suggest that the exponential distribution in equation (2.7) is also applicable to the power received by any type of linearly polarized antenna.

The total electric field magnitude $|E|$ is χ^2 distributed with six degrees of freedom and has the following probability density function [7] [8]:

$$f(|E|) = \frac{|E|^5}{8\sigma^6} \exp\left[-\frac{|E|^2}{2\sigma^2}\right] \tag{2.8}$$

Figure 2.2 shows a comparison of equation (2.8) with measured data taken under the same condition as in figure 2.1 [6].

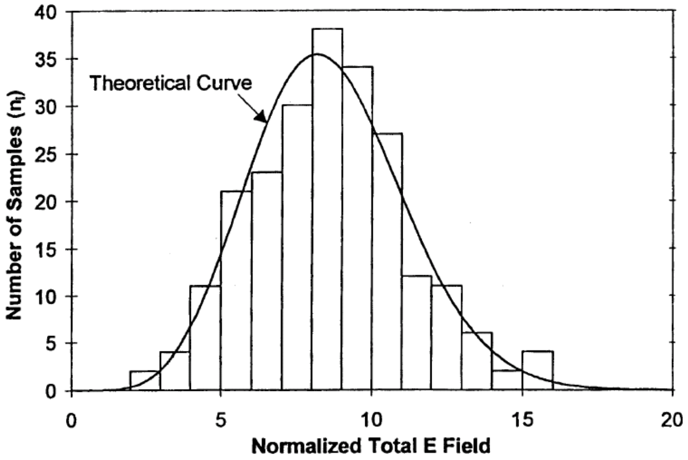

Figure 2.2: Comparison of the measured probability density function of the total electric field with χ^2 distribution with six degrees of freedom.

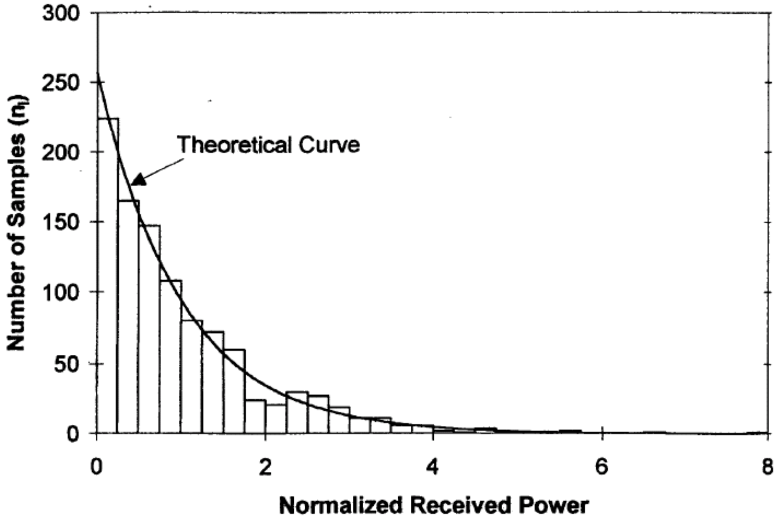

Figure 2.3: Comparison of the measured probability density function of received power with exponential distribution.

The squared magnitude of the total electric field is χ^2 distributed with six degrees of freedom and has the following probability density function [8]:

$$f(|E|^2) = \frac{|E|^4}{16\sigma^6} \exp\left[-\frac{|E|^2}{2\sigma^2}\right] \tag{2.9}$$

Similar techniques can be used to analyze the signal received by an antenna. Figure 2.3 shows a comparison between the exponential probability density function with data taken with a log-periodic dipole array at 1 GHz in the NASA chamber [6]. Also in figure 2.1 and 2.2 the antenna was a log-periodic dipole array.

2.2.2 Cavity quality factor

In general, the quality factor describes the ability of a EM system to store energy. Moreover, the bandwidth of a resonance depends on it:

$$\Delta f = \frac{f_0}{Q} \tag{2.10}$$

Although an analytical Q derivations for mono-mode resonators for each individual TE$_{mnp}$ and TM$_{mnp}$ mode is possible [9], such calculations are unpractical for highly overmoded RCs. A better approach is to use the definition of Q based on the steady-state energy stored in the cavity U_s and the dissipated power P_d and energy U_d:

$$Q = \omega\frac{U_s}{P_d} = 2\pi\frac{U_s}{U_d}. \tag{2.11}$$

Since in a RC the energy density W is uniform throughout the cavity volume V and equal for the electric and magnetic energies, $U_s = WV$ with

$$W = \varepsilon_0 E_0^2 \tag{2.12}$$

where ε_0 is the permittivity of free space, while the power density within the cavity

$$S = \frac{E_0^2}{\eta_0} = cW \tag{2.13}$$

should also be interpreted as an ensemble average. These relations give the expressions in (5.5), (5.6), and (5.8).

$$Q = \frac{16\pi^2 V}{\lambda^3}\frac{\langle P_{\mathrm{R}}\rangle}{\langle P_{\mathrm{T}}\rangle} = \frac{16\pi^2 V \langle P_r\rangle}{\lambda^3 \eta P_{in}(1-|S_{11_0}|^2)} \tag{2.14}$$

considering that $P_r = P_{in}|S_{21}|^2$.

The dissipated power is classically written as the sum of four terms

$$P_{\mathrm{d}} = P_{\mathrm{d1}} + P_{\mathrm{d2}} + P_{\mathrm{d3}} + P_{\mathrm{d4}} \tag{2.15}$$

corresponding to

$$\frac{1}{Q_{\mathrm{d}}} = \frac{1}{Q_{\mathrm{d1}}} + \frac{1}{Q_{\mathrm{d2}}} + \frac{1}{Q_{\mathrm{d3}}} + \frac{1}{Q_{\mathrm{d4}}} \tag{2.16}$$

where the terms as the following meaning:

1. P_{d1} is the power dissipated in the cavity walls, characterized by a permeability μ_{w} and a conductivity γ_{w}. The complete model for this effect can be found in [**?**], but for highly conducting walls the loss can be approximately determined from the skin depth

   $$\delta = \frac{1}{\sqrt{\mu_{\mathrm{s}}\pi f \gamma_{\mathrm{s}}}} = \sqrt{\frac{2}{\omega \mu_{\mathrm{s}}\gamma_{\mathrm{s}}}} \tag{2.17}$$

   leading to [**?**], [10]

   $$Q_1 = \frac{3V}{2\mu_{\mathrm{rw}}A_{\mathrm{c}}\delta}[1 + \frac{3}{16}\lambda(\frac{1}{L} + \frac{1}{W} + \frac{1}{H})]^{-1} \simeq \frac{3V}{2\mu_{\mathrm{rw}}A_{\mathrm{c}}\delta} \tag{2.18}$$

   where A_{c} is the chamber surface area. The expression (2.18) is very often utilized and is also the Q-factor estimate proposed in the IEC 61000-4-21 standard.

2. P_{d2} is the power absorbed in loading objects within the cavity. In general, the absorption cross section σ_{N} of a lossy object depends on the incidence angle and polarization of the incident plane wave. Hence, the absorbed power can be written as the product of the power density and the absorption cross section averaged over an incidence angle of 4π steradians and over all the polarizations

   $$P_{\mathrm{d2}} = S\langle\sigma_{\mathrm{N}}\rangle_{4\pi}, \qquad Q_2 = \frac{2\pi V}{\lambda\langle\sigma_{\mathrm{N}}\rangle_{4\pi}} \tag{2.19}$$

   The frequency dependence of Q_2 can be fairly complicated because of the frequency dependence of $\langle\sigma_{\mathrm{LO}}\rangle_{4\pi}$.

3. P_{d3} is the power lost through aperture leakage. The transmission cross-section σ_{T} of an aperture depends on the incidence angle and polarization of the incident plane wave, but only the plane waves that propagate toward the apertures contribute to the average cross-section

   $$\langle\sigma_{\mathrm{T}}\rangle_{2\pi} = \frac{\langle\sigma_{\mathrm{T}}\rangle_{4\pi}}{2} \tag{2.20}$$

   and then to the average transmitted power:

   $$P_{\mathrm{d3}} = S\langle\sigma_{\mathrm{T}}\rangle_{2\pi}, \qquad Q_3 = \frac{2\pi V}{\lambda\langle\sigma_{\mathrm{T}}\rangle_{2\pi}}. \tag{2.21}$$

   Since for electrically large apertures $\langle\sigma_{\mathrm{T}}\rangle_{2\pi}$ is independent of frequency, Q_3 is proportional to frequency. For small or resonant apertures, the frequency dependence of Q_3 is more complicated.

4. P_{d4} is the power dissipated in the loads of receiving antennas

   $$P_{\mathrm{d4}} = S\langle A_{\mathrm{eq}}\rangle, \qquad Q_4 = \frac{16\pi^2 V}{\lambda^3 m} \tag{2.22}$$

   deriving from the averaged effective area and from the impedance mismatch factor m of the receiving antennas, considering that the total power absorbed by all of the antennas is simply the sum of powers absorbed by the individual antennas. By superposition, the transmitting antenna will also act as a receiving antenna unless an external control system is used to maintain a constant net power into the chamber.

From (2.22), Q_4 is small and is the dominant contributor to the total Q for low frequencies, whereas the walls are the dominant loss mechanism at high frequencies.

A less used parameter that provides similar information is the chamber gain [6]

$$G_{\mathrm{C}} = \frac{\langle P_{\mathrm{R}}\rangle}{\langle P_{\mathrm{T}}\rangle} = \frac{\lambda^3 Q}{16\pi^2 V} \tag{2.23}$$

given the ratio of the power received by an ideal antenna to the transmitted power at any given paddle position? (whose inverse is the chamber loss). Knowing the characteristics of the antennas and of the walls, $\langle G_\mathrm{C} \rangle$ is predictable. Alternatively, they can be approximated by some measurements. If the permeability of the wall material is constant with frequency, Gc can be assumed as constant at low frequencies and decreasing for high frequencies, giving

$$\langle G_\mathrm{C} \rangle = \frac{\langle P_\mathrm{R} \rangle}{\langle P_\mathrm{T} \rangle} \simeq \left[N_a + \frac{4\omega^3 \delta(\omega) \mu_r A}{3c^3 \pi} \right]^{-1} \simeq \frac{1}{a + bf^{5/2}} \tag{2.24}$$

where b depends primarily on the characteristics of the walls and a replaces the number of receiving antennas in the chamber N_a to account for non-ideal antennas and for losses due to mechanisms other than the antennas.

2.3 Realization of the EMCLab reverberation chamber

In the EMC laboratory of the Department of Electrical Engineering of the University of Rome “La Sapienza,” the existing shielding room has been transformed into a reverberation chamber [11]. An aluminum stirrer and a stepping motor were installed in the existing chamber to provide an appropriate mechanical stirring of the EM field. The performances of the reverberation chamber have been characterized by means of calibrations and -factor calculations. In this the following section the details of the chamber realization, of the measurement set-up will be presented, and the early characterization tests reported.

2.3.1 Original structure

The chamber dimensions ($L \times W \times H$) are (3.52 m × 2.95 m × 2.49 m). The access door has dimensions (0.9 m × 2.24 m). The chamber walls are made of 2 mm thick painted stainless steel. The theoretical lowest usable frequency (LUF) for such structure is calculated to be three times the first resonance frequency, which is given by 2.2:

$$\omega_0 = 150 \sqrt{\left(\frac{1}{L}\right)^2 + \left(\frac{1}{W}\right)^2} \tag{2.25}$$

Figure 2.4: The RC with paddles, antenna and EM field sensor.

where L and W are the largest dimensions of the cavity and the first propagating mode is a TE_{110} mode. Operative measurements indicate that the LUF is 280 MHz. The inside of the actual RC is shown in Fig. 2.4.

2.3.2 Tuners and step-motor description

The mechanical tuner was designed and realized to obtain a non-symmetric mode agitator. The shape of the stirrer was chosen to reflect the incident waves in order to illuminate as many directions as possible and to obtain a RC with high stirring ratio (SR). For a fixed frequency, the SR is defined as the ratio between the maximum and the minimum power received by an antenna placed in a fixed point during a complete stirrer rotation [5]:

$$\text{SR} = \frac{P_{recMax}}{P_{recMin}}|_{1rotation} \tag{2.26}$$

where P_{recMax} and P_{recMin} are the maximum and minimum value of the received power, measured over a complete tuner revolution. The lower limit normally accepted for the SR is 20 dB. The SR takes into account both the over-moded condition and the stirrer effectiveness. However, over-moded condition is not sufficient for giving field uniformity. The size, the geometry and the position of the stirrer are fundamental for a correct stirring. Our stirrer is made of two hand-shaped, 2 mm aluminum plates, fastened on a brass mast and forming a $30°$ angle. The shape of the stirrer arms has been modified with respect to the first attempt in order to improve as much as possible the SR of the chamber. The initial and final stirrer shapes are shown in Figs. 2.5 and 2.6, respectively.

The stepping motor allows to realize a tuned-mode stirring. In this way the test environment is more stable and controlled than the one in the continuous stirring-mode [2]. Moreover the problems associated to time-varying fields are eliminated. The installed step-by-step motor is a Sanyo Denki 103H8221-62, with a Transtecno CM030 $1 : 50$ reduction gear. A programmable MIND T3 electrically operates the entire system. The use of the reduction gear allows to

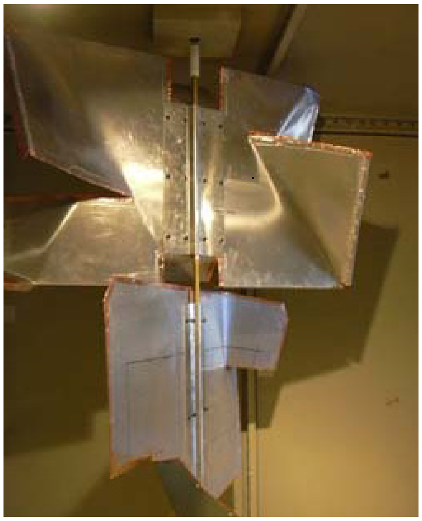

Figure 2.5: The stirrer before reshaping.

Figure 2.6: The new stirrer.

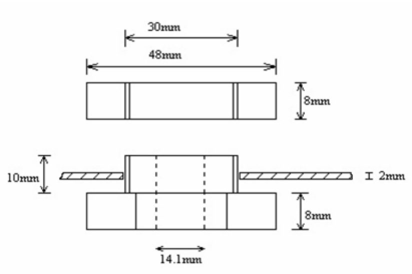

Figure 2.7: Details of the ball bearing/ceiling system

realize very accurate step resolution up to 50000 steps/revolution, that correspond to steps of $0.0072°$. The motor-reduction group is placed outside the chamber, over the roof. To avoid boring the ceiling, the motor-reduction group was bolted on a metallic plate, and attached to the top of the chamber by using a specific purpose glue. An acetalic resin coupler provides electrical isolation between the stirrer mast and the motor shaft. The shaft runs through a metallic ball bearing that is mechanically and electrically shorted to the chamber walls. Another flexible bearing block, attached to the floor, assures a correct support to the mast and, at the same time, it avoids forcing on the shaft in case of imperfect alignment. The details of the fixing system and of the coupler are shown in Figs. 2.7 and 2.8.

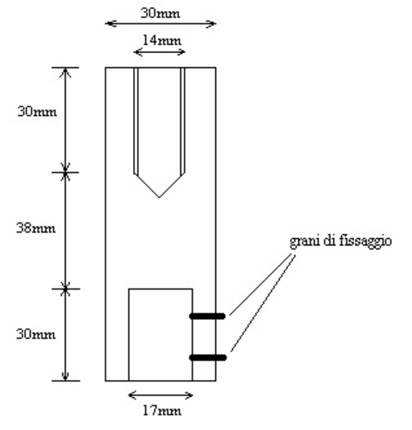

Figure 2.8: Details of the acetalic resin coupler

2.3.3 The measurement chain setup

According to the characteristics of the chamber, the minimum operating frequency range is estimated to be around 300 MHz-400 MHz. The upper frequency is limited by the available instrumentation, and reaches 18 GHz. The preliminary tests on the chamber presented in this paper refer to the frequency range up to 3 GHz. Such band is suitable to investigate the emission, the interference and the susceptibility of wireless systems, along with the effectiveness of volumetric shields in order to improve their immunity. In particular, the GSM operating frequencies (900, 1800 or 1900 MHz) are included. The measurement chain, sketched in Fig. 2.9 , is constituted by:

1. Two Electro-metrics 6961 horn antennas for the frequency range 1 GHz-18 GHz
2. Two log-periodic antennas: one Electro-metrics LPA-30 (200 MHz-1200 MHz) and one Electro-metrics 6951 (300 MHz-1200 MHz)
3. Two microwave amplifiers: an Amplifier Research 30W1000B and an Amplifier Research 25S1G4A
4. Anritsu 37369C Vector Network Analyzer (VNA)
5. PMM 8053A field meter for the field range 0.1-300V/m, with frequency range 100kHz-3GHz and 0.01 V/m sensitivity
6. Wandel&Goltermann EMR300 isotropic field sensor with a Type18 probe for field intensity 0.1-800V/m and frequency range 100kHz-3GHz, with 0.01V/m sensitivity

The vector network analyzer (VNA) was used to characterize the chamber performance pertaining the quality factor determination and the statistics of the received power, whereas the electric field sensor was used to characterize the field statistics. The chamber worked in the tuned-mode: the number of steps was initially set to 50 steps/revolution. Afterwards, it was found that 25 steps/revolution are sufficient to reach a good EM field stirring, leading to a considerable reduction

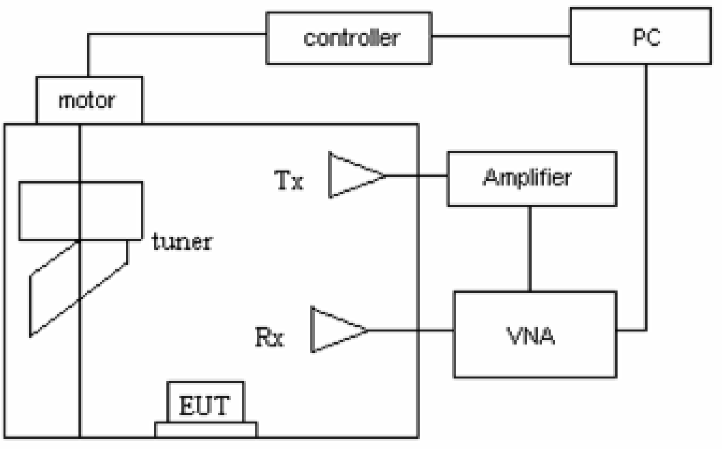

Figure 2.9: Schematic configuration of the measurement chain

of the measurement and testing time. The VNA was fixed to work with one frequency per time. The chamber performance has been tested within the operating frequency range.

A LabVIEW [12] virtual instrument (VI), custom developed and running on a dedicated PC, remotely controls the measurement system. The application is addressed to control the VNA, the program and to operate the motor, take measurements and store the results. The VNA control is operated by means of an IEEE-488 (GPIB) interface, while the motor actuator is fully operated by means of a RS-232 serial interface. In particular, if a synthesized signal generator (SG) is used to generate the modulated signal, on the receiving side a spectrum analyzer (SA) can be alternatively used to the VNA.

2.3.4 Calibration of the chamber

A direct method for uniformity evaluation consists in evaluating the maximum magnitude of each electric field rectangular component for a given number of positions within the chamber. This ensemble of data must fall inside a given uncertainty interval. This calibration method is based on field uniformity evaluation for the maximal values of the three electric field components at 8 calibration points. The field is considered uniform if the ensemble of maximum values falls inside

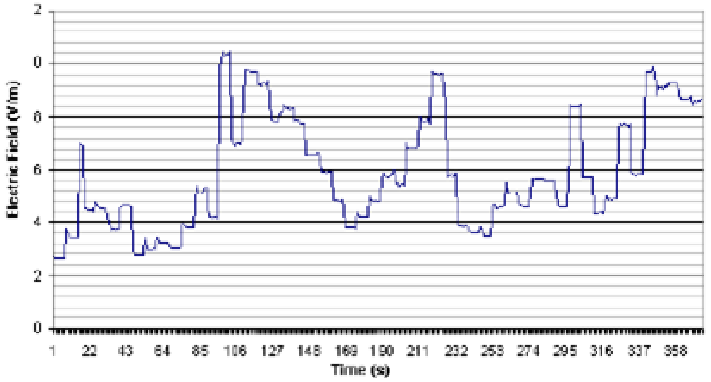

Figure 2.10: Electric field amplitude vs time during one tuner revolution at the frequency of 300 MHz

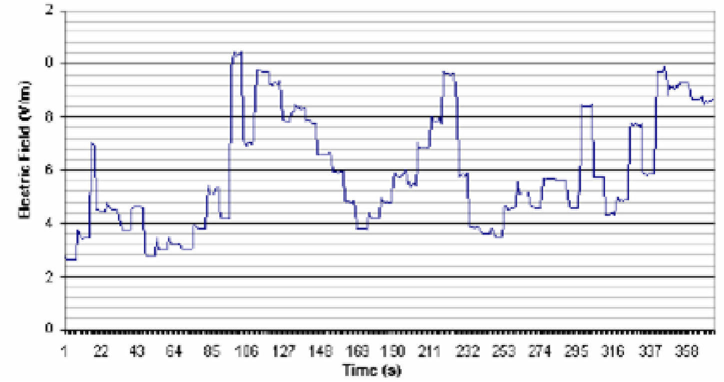

Figure 2.11: Electric field amplitude vs time during one tuner revolution at the frequency of 2 GHz

the -0 dB $+6$ dB interval around the mean value for the 75% of the entire volume (i.e., at least 18 among the 24 points of measurement). A tolerance reaching 10 dB is allowed for a maximum of three frequencies or for 3% of measurement frequencies. In order to ascertain the performances of the stirrer, the electric field amplitude has been recorded as function of time, during one complete tuner revolution. As an example, the waveforms measured at 300 MHz and at 2 GHz, 50 cm above the floor are reported in Figs. 2.10 and 2.11. It is observed that the RC performs better at lower frequencies.

It has been shown that inside a chamber, where fields are homogeneous, isotropic

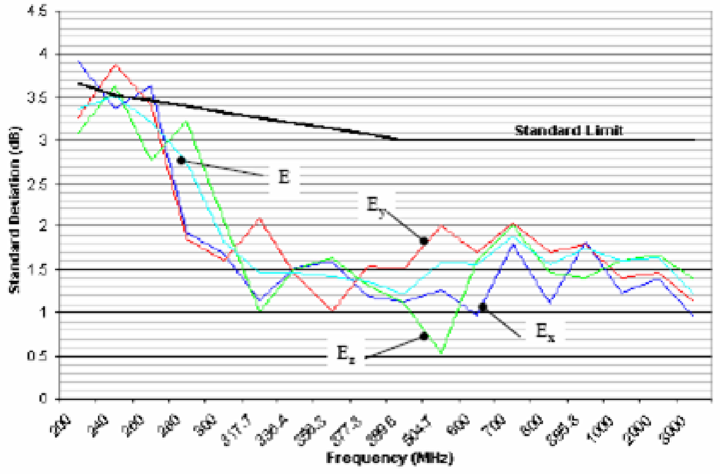

Figure 2.12: Standard deviations in dB of the three electric field components vs frequency for 50 steps/revolution, compared with the limit suggested by the standard.

and randomly polarized, the power received by any matched antenna is Chi-squared distributed with two degrees of freedom. Conversely, if power samples of a real chamber follow such a distribution, then statistical uniformity properties are verified. The measurement volume has been defined according to the procedure described in [5]. The minimum distance of 30 cm from the chamber wall has been considered. Due to the presence of the transmitting antenna, the resulting measurement volume measures about 4 m^3. The standard deviations of the three electric field components in the eight different measurement points inside the test volume are evaluated, according to [5]. The obtained results, expressed in decibel, are reported in Fig. 2.12. Figure 2.13 shows the standard deviation σ of the total electric field, calculated from measurements at nine probe positions inside the working volume.

2.3.5 Chamber quality factor

The quality factor (Q) indicates the ability of a cavity to store energy and it is determined by the chamber losses. At lower frequencies the chamber losses are due to the antenna losses, but at higher frequencies, the losses are definitely due

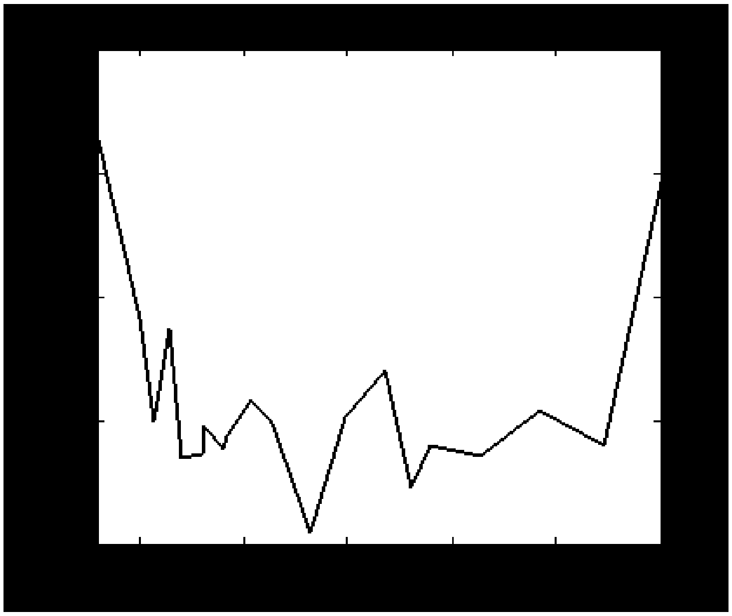

Figure 2.13: Standard deviation σ of the total electric field.

to the chamber characteristics. The Q factor is defined as [5]:

$$Q = \frac{\omega U}{P_d} \tag{2.27}$$

where U is the energy stored in the cavity and P_d is the dissipated power. Since the average energy density can be shown to be independent of position, the stored energy can be written as the product of the average energy density (W) and the chamber volume (V). The volume of the cavity is independent of the shape of the cavity. For steady state conditions, conservation of power requires that the dissipated power equals the transmitter power P_t, and since this one can be related to the power P_r received by a receiving antenna located in the chamber, then Q as regards an RC having volume $V(m^3)$, and for a given wavelength λ (m), it can be expressed as [13]:

$$Q = \frac{16\pi^2 V}{\lambda^3 \eta_{Tx}\eta_{Rx}} \left\langle \frac{P_{AveRec}}{P_{input}} \right\rangle_N \tag{2.28}$$

where $\left\langle P_{AveRec/Pinput} \right\rangle$ is the ratio of the average received power to the input power over one complete tuner/stirrer revolution, averaged over N antenna locations; η_{Tx}, η_{Rx} are the antenna efficiency factors for the transmitting (Tx) and

Figure 2.14: Experimental Q of the empty RC of the Department of Electrical Engineering of the University of Rome Sapienza.

receiving (Rx) antennas, respectively. Such factors can be assumed to be 0.75 and 0.9 for log-periodic and horn antennas respectively.

Figure 2.14 shows the quality factor (Q) of the empty chamber calculated from experimental data for the 300 MHz-3 GHz frequency range.

As a rule of thumb, another parameter MD_{BQ} is frequently used to estimate the number of modes simultaneously excited in a cavity with given quality factor Q and at a specific frequency f expressed in Hz. For a rectangular cavity MD_{BQ} is defined as:

$$MD_{BQ} = \frac{8\pi V f^3}{c^3 Q} \tag{2.29}$$

where c is the velocity of light.

In the transformation of the chamber lots of attention were dedicated in avoiding to introduce lossy materials. The original wooden floor protection was removed. All fissures and holes were filled with steel wool and covered with high conductive copper tape. Bulb lights were removed and fan conductors sealed. We chose brass for the stirrer mast and aluminum for the stirrer plates. The power supplies are filtered to the outside to avoid conductive emissions to the outside. Particular care was taken in designing the flange between the stirrer mast and the motor shaft, in order to avoid any possible leakage of radio frequency energy to the outside of the chamber. Although, the chamber was originally a shielding room and its walls are made of painted stainless steel. This results in a lossy cavity, with relative low quality factor.

2.4 Conclusion

This Chapters presented an introduction on reverberation chamber test facilities. Afterwards, the realization of a reverberation chamber starting from a shielded room, is fully detailed. The RC operates in tuned mode and the measurement chain is remotely controlled by a custom developed software tool. Details on the

LUF, Q factor and statistical behavior obtained by means of the standard calibration procedure are presented. Eventually, there is a discussion on the problems encountered along with the relative adopted solutions.

Chapter 3

Simulation of the EM Environment inside an Aircraft

The existing shielded room of the EMC laboratory of the Department of Electrical Engineering of the University of Rome “La Sapienza,” was transformed into a low-Q reverberation chamber in order to perform EMC tests in an aircraft-like electromagnetic environment. The Q-factor was intentionally lowered to reproduce the typical electromagnetic environment aboard aircraft. The performances of the chamber were evaluated when an amplitude modulated signal excites the cavity.

3.1 Introduction

A two-year research project involving four research units of three Universities in Italy is currently in progress. Its aim consists in the developing of a sensor network for the detection and localization of cellular phones and portable electronic devices (PEDs) operating without authorization onboard aircraft. Due to the unavailability of a real aircraft and the complexity to simulate the operating conditions, a proper alternative experimental set-up needs to be defined [14]- [15]. The environment inside an aircraft is characterized by multiple reflection and scattering, random polarization, multi-mode and multi-path propagation. The actual electromagnetic (EM) environment is characterized by stochastic field isotropy and uniformity due to the continuous changing of position of both emitting devices and people inside the cabin, acting as mode stirrer [16]. It can be assumed that a fuselage is similar to an enclosure with conductive walls containing lossy materials [15], [16], [17]. The lossy materials load the structure and cause the quality factor (Q) to decrease. Testing in a reveberation chamber (RC) can be described as a stochastic process in which the mechanical tuner "stirs" the modes excited inside the enclosure [18]. Typically, RCs are characterized by high Qs in the range of thousands. Low-Q RCs can be properly realized by introducing in the test volume a controlled amount of lossy material [18]. An aircraft can be definitely assumed to behave as a low-Q RC [16], [17], [19]. In our RC we reproduced the EM environment of an aircraft to investigate the effect of a cellular phone operating in a reverberating environment, with a Q very similar to the one of an aircraft [20]. This procedure was necessary to reproduce the EM environment onboard an aircraft to test a sensor for cellular phones to be used in a fuselage.

3.2 The Q-factor in the aircraft EM environment

As remarked in 2, the Q is an important characteristic of every resonant cavity. A high Q is desirable in many applications, for example when high field levels are required. In general, the number of excited modes in the chamber is reduced as the Q. However, a low-Q RC can be still effective if it meets the field statistical requirements. Recent studies report minimum acceptable values of Q for operating RCs [21]:

$$Q_{th} = \left(\frac{4\pi}{3}\right)^{\frac{2}{3}} \frac{V^{\frac{1}{3}}}{2\lambda} \tag{3.1}$$

and

$$Q_{thp} = 3Q_{th}. \tag{3.2}$$

Therefore, if the Q is several times greater than such threshold values, the RC can be considered effectively operating. Q_{th} is calculated starting from stirred and unstirred energy considerations, while Q_{thp} is obtained on the basis of probability density observations [21]. The two threshold values differ for a factor of three, and it can be noted from the comparison of 3.1 and 3.2, the probability density method leads to a more stringent limit than the power density approach. A peculiar consequence of having a low Q is that the chamber is less sensitive to the loading effects [14], [16]: it means that the Q does not decrease proportionally with the load of the RC. Such property is extremely important for the aim of this study considering that an aircraft does not have a constant "loading" in general, because people and cabin luggage are strongly variable. However an average load can be considered as representative without altering sensitively the EM environment.

In order to investigate the performances of field sensors for the detection of dual band cellular phones [22], we considered a discrete number of frequencies within the operation band of both the global system for mobile communication (GSM) and the 1800 digital cellular system (DCS), that are typical of European standards. The test frequencies are 890 MHz, 900 MHz, 915 MHz, and 1800 MHz. To exemplify the proposed approach, the results obtained at the frequency of 900 MHz are presented in the following. As regards our RC, at 900 MHz the threshold Qs, defined by 3.1 and 3.2 are respectively $Q_{th} = 11.53$ and $Q_{thp} = 34.58$. Such values are fairly lower than the Q of an aircraft at the same frequency. Originally, a relatively lower Q characterized our RC, but anyway too high to resemble the Q of an aircraft if compared with data presented in literature [14]. To reproduce the typical aircraft environment we decided to lower the Q by introducing some load units as suggested in [14], [21], [23]. Table I reports the average cavity Q in a Boeing 757 aircraft with 200 seats. Accordingly, the target value in the GSM band can be set to $Q_{des} = 350$.

The empty RC was characterized at the considered frequency of 900 MHz by means of key-parameters defined in [13]. The Q is 950. The uniformity of the chamber, which is expressed by the standard deviation

$$\Sigma = \frac{1}{\sqrt{N-1}}\sqrt{\sum_i \left(E_{MAXi} - \langle E_{MAXi} \rangle\right)^2} i = 1...N \tag{3.3}$$

assumes the value of 2.49 dB. The stirrer ratio, defined in 2.26 is 19 dB, in

Table 3.1: Typical Q for commercial aircraft [17].

Frequency (MHz)	Q
300	137
600	237
925	350
1000	375
1800	850
3200	1250

agreement with the minimum limit value of 20 dB [18], [19]. Fig. 3.1 shows the cumulative distribution function (cdf) of the received power for the empty chamber. This distribution was chosen to represent the good statistical behavior of the chamber. It shows the probability to find a value of the received power, at a fixed frequency, and a fixed test setup to be less than a given value.

3.3 RC Q-factor control to reproduce an aircraft-like EM environment

According to the considerations introduced above, it is assumed that in low Q reverberating environments small changes in the load do not affect considerably the Q because of the non linear dependence of the Q on the loads as in [17]. This characteristic of having a low Q is extremely important for the aim of this study considering that an aircraft does not have a constant “loading” in general, because people and cabin luggage are variable for shape, position, and “material”.

In order to simulate an aircraft EM behavior mainly by reproducing a reverberating environment having the Q factor of an empty fuselage [15], [14] and to obtain the Q value of our RC compliant with the data of Table 3.1, we loaded the cavity with a number n of chairs carrying absorbing materials. Of course,

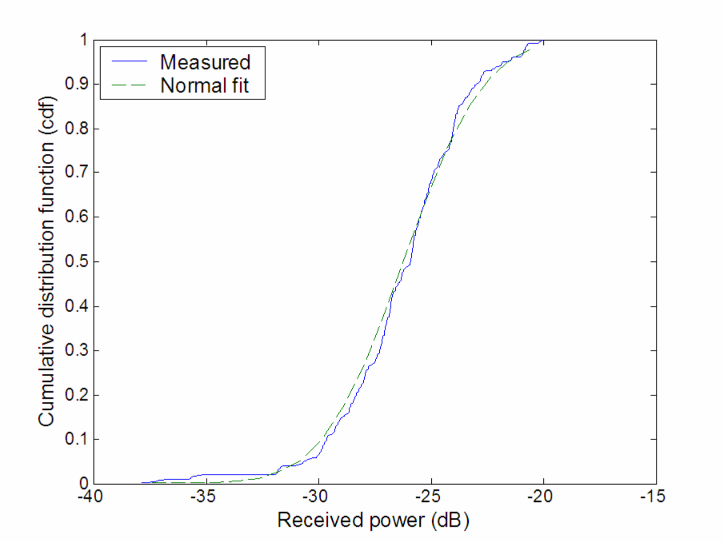

Figure 3.1: Cumulative distribution function (cdf) of the received power at 900 MHz for the empty chamber and P_{input} =0 dB.

the aim was to simulate the presence of airplane seats and people using cellular phones. The lossy seats (LSs) were placed within the working volume as shown in Fig. 3.2, the clearance recommended from [14] from conducting surfaces and antennas was respected and the introduced additional power loss was measured.

The inverse of the Q of the loaded RC (Q_{Total}) is given by the sum of the inverse of the Q_s of the empty chamber Q_0, and of the n loads intentionally placed inside the chamber (Q_{LS}/n) according to the following expression [22]:

$$\frac{1}{Q_{Total}} = \frac{1}{Q_0} + \frac{n}{Q_{LS}} \tag{3.4}$$

where Q_{LS} is associated to a single loss seat occupying the volume V_{LS}:

$$Q_{LS} = \frac{2\pi V_{LS}}{\lambda \langle \Sigma_a \rangle} \tag{3.5}$$

$\langle \Sigma_a \rangle$ being the absorption cross-section per LS. An estimation of Q_{LS} and $\langle \Sigma_a \rangle$ can be obtained from measurements of Q_0 and Q_{Total}:

$$\langle \Sigma_a \rangle = \frac{2\pi V_{LS}}{\lambda} \left(\frac{1}{Q_{Total}} - \frac{1}{Q_0} \right) \tag{3.6}$$

Figure 3.2: Experimental setup with two seats occupied by two “passengers” using a cellular phone.

By combining 3.4 and 3.5, Q_{Total} can be expressed as a function of the number of LSs:

$$Q_{Total} = \frac{Q_0}{1 + k_Q n} \tag{3.7}$$

with:

$$k_Q = \frac{Q_0}{Q_{LS}} \tag{3.8}$$

The minimum number of LSs to introduce in the RC in order to achieve the target value $Q_{Total} = Q_{des} = 350$ at 900 MHz, is finally given by:

$$n_{min} = int\left[\frac{Q_{LS}}{Q_{des}} - \frac{Q_{LS}}{Q_0}\right] = 3 \tag{3.9}$$

Fig. 3.3 shows the measured Q_{Total} as function of n.

Anyway, in both cases, it should be noted that the simulation of the aircraft environment is achievable only if the reduction in the Q_{Total} does not excessively degrade the isotropy and the uniformity of the field. Measurements were carried out in order to verify this condition [24] according to the guidelines in [13]. In

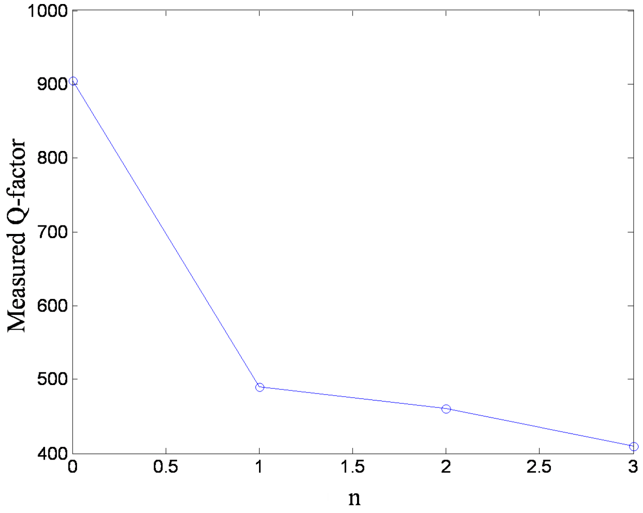

Figure 3.3: The experimental curve relative to the Q measured for increasing number of LSs.

particular, the graph in Fig. 3.4 represents the cdf of the chamber loaded with seats and polyfoam bricks. Notice that the obtained curve still fits satisfactory the theoretical cdf. The chamber loading factor (CLF) is given by the ratio of the average received power with the load in place (P_{RecEUT}) and the average received power, calculated during the calibration, of the empty chamber (P_{AveRec}):

$$CLF = \left\langle \frac{P_{RecEUT}}{P_{AveRec}} \right\rangle \tag{3.10}$$

where N is again the number of antenna locations. The CLF is usually an expression of how much a device under test loads the empty chamber. If we consider the LSs as part of the test setup, from 2.28 and 3.10, considered for the loaded and the empty chamber, it yields that for increasing number of LSs, the CLF of the loaded chamber follows the same trend of Q_{Total} shown in Fig. 3.3.

When an RC is being loaded, its working volume is reduced by the presence of the absorbing units (AUs), but it has to be still large enough to accommodate the AUs and all the devices under test (DUTs) with the necessary clearance. For this reason the use of compact and highly effective AUs is strongly desirable in order to control the Q_{Total} and, at the same time, to maximize the working volume

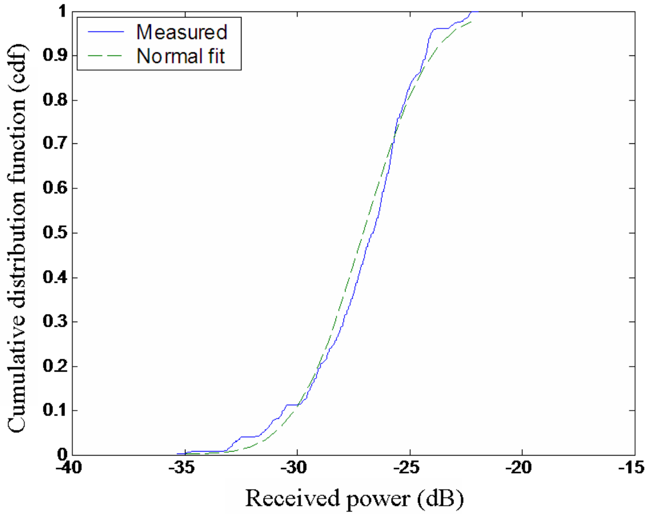

Figure 3.4: The cdf of the received power at 900 MHz for the RC loaded with three LSs and P_{input} =0 dB.

of the loaded RC.

Successively, in order to obtain a more controllable environment and at the same time to have more compact AUs, the chamber was loaded with a number n of AUs each consisting in three plastic bottles of 1.5 liters filled with water instead of the seats. The AUs were placed within the working volume, and the clearance recommended in [13] from conducting surfaces and antennas was respected. Beside the limited dimension of the introduced material, the main advantage of using this kind of AUs consists in the possibility to precisely evaluate V_{AU} which is necessary to estimate $< \Sigma_a >$ and Q_{AU} from **??** and 3.5, respectively. Before, by using the seats carrying polyfoam bricks, it was not not easy to perform an accurate evaluation of V_{AU} and $< \Sigma_a >$, k_Q and n_{th} were defined only on the basis of the numerical fit of the experimental curve.

Therefore all the considerations made above hold if we consider the contribution of n AUs intentionally placed inside the chamber instead of a lossy seat LS. Equations 3.4-3.9 can be modified by substituting the subscript AU to LS.

Equation 3.4 to 3.9 become respectively:

$$Q_{AU} = \frac{2\pi V_{AUS}}{\lambda \langle \Sigma_a \rangle} \tag{3.11}$$

$$\langle \Sigma_a \rangle = \frac{2\pi V_{AU}}{\lambda} \left(\frac{1}{Q_{Total}} - \frac{1}{Q_0} \right) \tag{3.12}$$

Q_{Total} is still a function of the number of AUs:

$$Q_{Total} = \frac{Q_0}{1 + k_Q n} \tag{3.13}$$

but, this time k_Q is calculated from:

$$k_Q = \frac{Q_0}{Q_{AU}}. \tag{3.14}$$

Therefore, the theoretical number of AUs necessary to obtain a desired Q_{des}, according to 3.9 is predicted by:

$$n_{th} = \frac{Q_0 - Q_{des}}{K_Q Q_{des}} = \frac{Q_{AU}}{Q_{des}} - \frac{Q_{AU}}{Q_0}. \tag{3.15}$$

Figure 3.5 shows the measured Q_{Total} as a function of n. Two different fit functions are proposed. The theoretical fit is the curve derived from 3.15 in which Q_{AU} is estimated by 3.5. The best-fit curve is obtained by estimating the parameters in 3.7 in order to achieve the best approximation of the experimental data. It can be noted that the two curves are very close to each other and to the measured values, thus indicating a good correlation between theoretical and experimental results.

3.4 The test signals

The chamber was excited with a continuous wave (CW) tuned at the fixed frequency of 900 MHz. Afterwards, we decided to investigate the behavior of the RC excited by a GSM modulated signal. This is fundamental for us, because one of our targets is to test and characterize a prototype of a sensor for the detection of cellular phones to be used onboard aircraft [22], [25]. This sensor is sensitive only

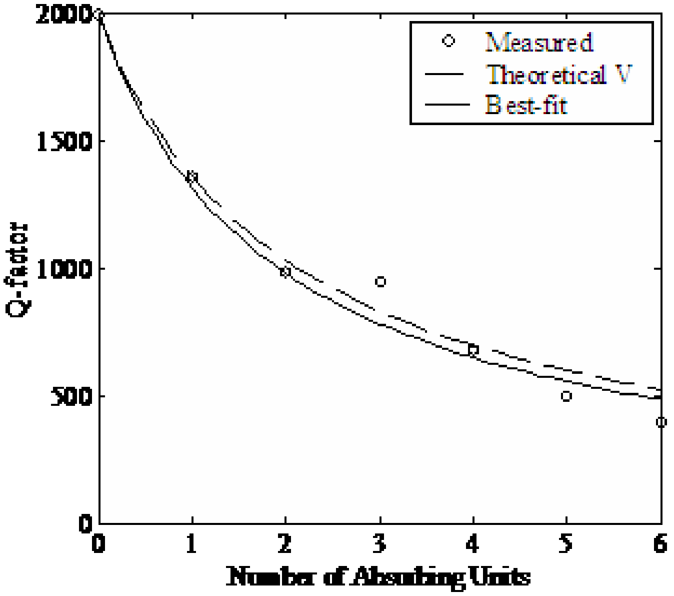

Figure 3.5: Quality factor as a function of increasing number of AUs.

to the GSM modulated signal. The aim is to verify whether the sensor operates correctly also in a realistic environment, when many sources of electromagnetic interference (EMI) are present contemporarily. Moreover sensitivity and immunity tests on the sensor should be performed. Since a real cellular phone does not radiate inside a shielded enclosure, we used a mock-up made at the Department of Electronic Engineering of our University (Fig. 3.6). Such mock-up consists of a metallic box, having the typical dimensions of a cellular phone, equipped with a helix antenna tuned at 900 MHz [26].

3.5 Experimental results

The power received by a reference antenna and the field level registered from a field meter, both placed inside the RC, where measured, according to the guidelines in [13], when the mock-up was fed with an amplitude modulated (AM) signal at 900 MHz that simulates the effects of a GSM-modulated signal. The signal generator was set to transmit with a depth rate of 100 %. It means that the total

Figure 3.6: The cellular phone mock-up with the antenna tuned at 900 MHz used as a transmitter inside the RC.

radiated power is split between the center frequency and the modulating signal. Therefore, the power received as in Fig. 3.7 shows an offset of -6 dB with respect to the one reported in Fig. 3.4.

An appropriate dwell time, covering at least two full cycles of modulation, was applied. Generally the dwell time at each test frequency shall be at least 0.5 s, exclusive of test equipment response time and the time required to rotate the tuner to a full stop. The acquisition system and the stepping motor are completely controlled by means of a virtual instrument developed in LabVIEW and running on a dedicated personal computer [11].

3.6 Conclusion

An RC having a low Q was realized in order to reproduce the electromagnetic environment aboard aircraft at the operating frequencies of dual-band cellular phones. The target value of Q, typical of the loaded fuselage of a commercial aircraft at 900 MHz, was achieved inside the RC by introducing up to three “lossy seats”. The Q of a single lossy load was derived from measurements. The preliminary results of the performed tests demonstrated that the statistical properties of the EM environment inside the low-Q RC are maintained. In order to generate the EM field produced typically by a cellular phone, a mock-up supplied by

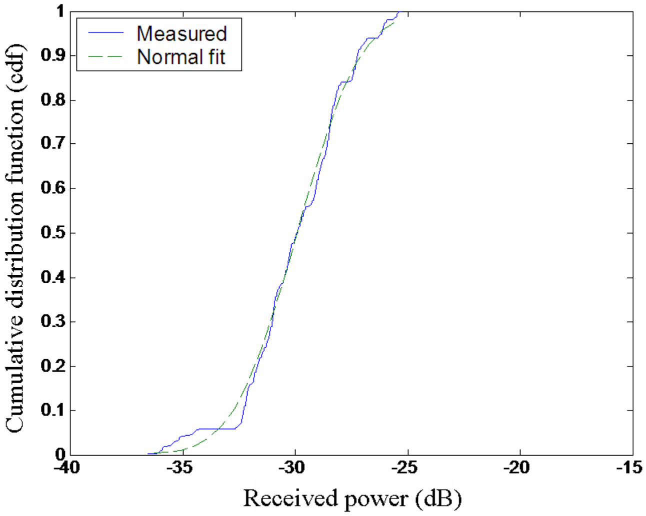

Figure 3.7: The cdf of the received power for the RC excited with an AM modulated signal at 900 MHz, P_{input} =0 dB and depth rate 100 %.

an AM signal at 900 MHz was used. The measured cdf of the received power with the AM excitation was calculated and compared to the one measured with the mock-up supplied by a CW at 900 MHz.

Chapter 4

Detection of Portable Electronic Devices aboard an Aircraft

This Chapter describes an innovative procedure for the characterization of a field sensor in an aircraft-like EM environment. The sensor prototype under investigation is sensitive only to amplitude modulated signals and it has been designed to be installed as sensing unit in an intelligent network for the localization of GSM cell phones operating aboard without authorization. The EM environment is simulated by means of a low-Q reverberation chamber as described in Chapter 3. The response of the sensor, expressed by the activation probability in a given operating condition, is obtained as a function of frequency, voltage supply, and incident field level.

4.1 Introduction

Mobile phones and portable electronic devices (PED) are increasingly pervading people's life, but their use is restricted in many indoor environments and situations. The influence of a commercial phone placed at few meters from an electronic system may exceed the limits for which the system is tested and certified according to the main electromagnetic compatibility (EMC) standards. Moreover, the actual field level is normally unpredictable, as the transmission frequency and the strength of a GSM device can continuously change and depend on many aspects, including the phone model and the cell coverage. As far as the characteristics of an indoor environment are concerned, this unpredictability is further enhanced by the effect of multiple reflection and scattering, random polarization, multi-mode and multi-path propagation, leading to constructive as well destructive interferences, especially when more than one phone is present. It is worth noticing that a low coverage and then the worst cases of emission are typical of the restricted areas, as the aircrafts. Strictly speaking, in particular conditions of altitude, velocity, temperature, and so on a cellular phone is supposed to not operate, but it is not excludable in practice, as confirmed by the common experience. During the last years, several studies highlighted that portable electronic devices (PEDs) can potentially disturb instrumentation and apparatus onboard aircraft with relevant consequences on the flight safety and security [27], [28], and [29]. Most of the PEDs are prohibited only during the most delicate phases of a flight, as take-off and landing, while the use of cellular phones is prohibited at every time when the doors of the aircraft are closed. Nowadays, the respect of these simple safety rules depends on passengers' responsibility, implying that an unintentional or malicious use of cellular phones may occur. For these reasons, according to the Radio Technical Commission for Aeronautics (RTCA) recommendations, many flying companies adopt special detection systems in order to avoid unauthorized use of PEDs onboard aircraft and consequent hazardous situations [30], [31], and [32]. However, the systems nowadays employed for the detection of mobile phones do not allow the identification of their exact position and generally fail when two sources are active.

Since 2004, a research project has been carried out by the EMC group of Sapienza University of Rome in order to develop a system for the detection and the localization of operating cellular phones aboard aircraft. The feasibility of such system has been investigated in [22] and [33]. The preliminary study on the radiated emissions and the propagation of the electromagnetic (EM) fields produced by commercial devices in aircraft environments [27], [22], [34], [35] were useful to derive specifications for the design of a localization system based on a grid of sensing units [36]. In particular, a single sensor can detect an emitting source, but it is not able to give sufficient information to estimate its exact position. This problem can be solved by implementing a distributed intelligent network of sensors that selectively adjusts the sensitivity of the sensor units and processes the information supplied by each detector. For example, the results obtained in [37] suggest that a first possible strategy to locate an emitting device inside an aircraft may consist in placing one sensor in correspondence of each passenger seat. In order to locate the position of an operating cell phone, it is necessary to identify which sensor receives the strongest signal from the phone. Then, if the minimum signal detectable from all the sensors is gradually decreased, some of the sensing units will turn off and only the sensor that receives the strongest signal will last, leading to the determination of the desired position [36]. Obviously, these operative principles and the necessary amount of sensor units to be installed in the network require the use of small, lightweight, and low cost sensing devices. Moreover, the detection sensitivity should be externally regulated through an automatic mechanism, for example by varying the voltage supply of the sensing unit.

Once the strategies for the detection are established, the response of a single sensing unit needs to be characterized in real operating conditions, i.e. in an EM environment that is similar to that aboard aircraft, and in such conditions the activation curve of the sensor should be defined as a function of frequency, voltage supply, and EM field level. To this purpose, an innovative testing procedure exploiting the properties of a reverberation chamber (RC) is developed in this paper.

In fact, the EM environment inside an aircraft is characterized by multiple reflection and scattering, random polarization, multi-mode and multi-path propagation. Moreover, the continuous changing of position of both emitting devices and people inside the cabin acts as mode stirrer and leads to the stochastic isotropy and uniformity of the field distribution [14]. Traditional test facilities, like open test sites (OATS) and anechoic chambers are generally inadequate for these types of tests because they offer a partial representation of the environment inside the fuselage, where the hypothesis of free space propagation is no longer consistent. Due to the unavailability of an actual aircraft, and the complexity to simulate the operating conditions, a proper alternative experimental set-up needs to be individuated. Several studies have demonstrated the similarity between the EM environment inside an aircraft fuselage and the one in a RC with low quality factor Q [14], [15]- [38].

Accordingly, in this Chapter the sensitivity of the sensor is statistically defined and experimentally estimated by means of a low-Q RC opportunely loaded in order to simulate the EM environment inside the aircraft as described in Chapter 3. Even if the characterization is applied on a particular EM sensor, the same procedure and approach can be easily extended to every EM detection device operating in a reverberating environment. To validate this approach, the operating conditions of the test facility need to be verified. In particular, the chamber has to be sufficiently overmoded and to respect the statistical behavior expected for an effective RC, especially in correspondence of the test frequencies [13], [3], [6], and [33]. Moreover, the adopted tests signals are modulated according to the Global System for Mobile Communication (GSM) and the 1800 Digital Cellular System (DCS) that are typical European standards.

4.2 GSM: the system for mobile communication

The GSM is a popular standard for mobile phones, originally from Groupe Spécial Mobile. The GSM system was firstly standardized around the 900 MHz frequency by allocating two distinct 25 MHz-wide bands divided in 124 radio channels with a 200 kHz capacity. The lower band, 890 MHz-915 MHz, is used for the uplink, the higher one, 935 MHz-960 MHz, for the downlink. The natural evolution of this standard, known as personal communications network (PCN) protocol, occupied a 75 MHz bandwidth around 1800 MHz or, due to the unavailability of such band as in North America, a 140 MHz band around 1900 MHz. A particular access technique allows several entities to share the same GSM media resources by combining the principles of the frequency division multiple access (FDMA) with the time division multiple access (TDMA). In this mixed approach, each mobile station (MS) uses a single assigned carrier but transmits by sending a series of bits (burst) only for a predefined time interval (timeslot). The sequence is made of a cyclically recurring frame of 8 timeslots. During the successive 7 timeslots the same carrier can be used by other MSs to transmit their bursts. According to the GSM standard, the duration of a frame coincides with the period $T = 1/F = 4.616$ ms, where F is the frequency of the signal emitted by a cellular phone and it corresponds to the output of the GSM detection unit while the duration of a timeslot $\tau = 577$ μs is the length of the phase-modulated transmission. One of the main peculiarities of the GSM system consists in the capability of varying the carrier frequency (frequency hopping) and the strength of the signal at every timeslot in order to optimize the transmitted power and to attenuate the fading effects. To support this mechanism the MS and the base station (BS) exchange information concerning the quality of the channel even during the ordinary communications. The choice of the signal parameters is due to the BS, but it has a relevant effect on the behavior of the cellular phone emission. Therefore, it is useless to develop a detection system that tracks the exact field and frequency of the emissions related to a GSM phone, especially in a complex and moving environment. Moreover, since the number of frames necessary for each phone operation (call, conversation, short message service, BS search, and so on) is different, the duration of a pulse series and its recurrence are totally unpredictable. It is then evident that this kind of problem can be approached only from a statistical point of view.

4.3 The sensor unit

Different technological solutions have been proposed for the detection of PEDs and cellular phones in critical environments, like for instance hospitals, inflammable sites, conference rooms, and theaters, even though in most of such situations a disturbing jammers may be sufficient to discourage the phone abuse. Some of the available techniques are inappropriate for the considered application as they are essentially designed for large and outdoor environments [39] or require to move the receiving antenna [40]. The most interesting systems are based on the estimation of the difference of the arrival time measured by two or more antennas [41] or on the comparison of frequency and strength of the waveform registered by a scanning radio receiver [42]. Other proposals may include simulated BSs that are also able to request the subscribers' data from the MS and to associate them to the passengers' list [41]. In [36] it is described a localization system based on a grid of sensors controlled by an intelligent network that has the double aim to process the information coming from the sensors and to adjust their sensitivity by varying the applied voltage supply. The core of such system, consisting in a low-cost prototype of EM sensor unit designed for the detection of cellular phones [22], is characterized in this paper. The fundamental element of the sensor unit is an active device, a BJT transistor. An external adjustable dc voltage source Vs, varying from 5 V to 12 V, can shift and control the bias and operating point of the transistor. In this way, the applied voltage allows to adjust the level of the minimum detectable signal and hence the sensor sensitivity against the EM field. Basically, the base-emitter junction of the sensor unit operates as a demodulator. For this reason, the sensing unit is able to reveal amplitude-modulated signals, while a continuous wave (CW) does not cause a meaningful response. The sensor output is the voltage induced between the transistor emitter and ground. Such voltage is revealed by a LED that switches on when the external EM field overcomes the given reference level. When the exciting source is a GSM modulated signal, the sensor output voltage is typically constituted by a sequence of pulses with frequency $F \approx 217$ Hz and duty cycle $\delta \approx 17\%$.

4.4 Characterization of the sensor unit

The design of the detection system requires at first the characterization of the response of the sensor unit when exposed to a GSM-type signal in an aircraft-like EM environment in order to determine its sensitivity. For this reasons, the EM environment inside an aircraft was simulated by means of a low-Q reverberation chamber as described in Chapter 3. In order to investigate the distribution of the EM field inside the fuselage of a commercial aircraft when a limited numbers

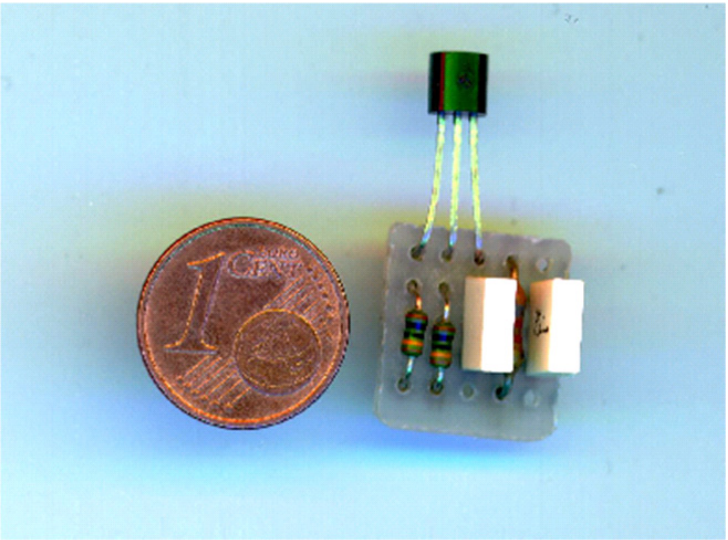

Figure 4.1: Prototype of sensing unit.

of devices are emitting at the same time, an EM simulation tool has been developed [37]. The results of the numerical simulations show that the detection and localization of an emitting device inside a reverberating environment is feasible by using a network of sensors with self-adapting field sensitivity level, as described in the previous section, and suggests the displacement of one detector in correspondence of each seat to efficiently locate an emitting device.

Figure 4.2 schematizes a possible application of the distributed network to monitor the presence of disturbing cellphones, by means of sensors opportunely placed under the aircraft seats.

4.4.1 Measurement setup and test signals

The preliminary characterizations of the sensor were performed in both indoor and outdoor environment using a commercial GSM phone to verify the response of the sensor unit to different emitting conditions like outgoing or incoming calls, messages and absence of the signal from the base station [22]. The results obtained even if interesting are not completely representative of the behavior of the sensor unit in the reverberating environment where the sensor will be operating. For this

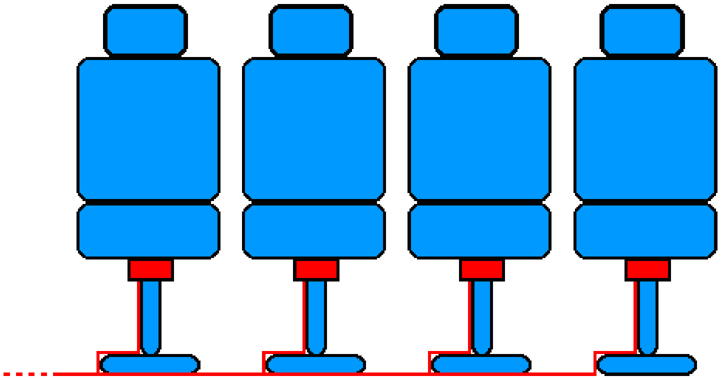

Figure 4.2: Possible configuration to monitor an environment using a grid of sensors placed under each seat.

reason the test was performed in a loaded RC, able to simulate the EM characteristics of the interior of an aircraft. The sensor is only able to reveal the presence of an incoming amplitude modulated signal, but it is not able to decode any information carried by the detected signal. For this reason, the applied exciting signal was a GSM waveform of period T, and pulse duration τ. To this purpose, we used a synthesized signal generator providing carriers at different frequencies modulated by a pulse having period $T = 4.615$ ms and duration $\tau = 577\mu$s. The sensor was tested in the RC loaded with six AUs in order to have Q equal to 350 at 900 MHz. The sensitivity curves were derived from the measurement of the received power and of the measured electric field components, obtained by means of a spectrum analyzer and a field meter respectively, for increasing values of the input power P_{input}.

4.4.2 Sensitivity as probability of activation

The characteristic curves of the sensor are estimated applying a statistical approach, according to RC testing methods. During a complete rotation of the stirrer obtained through N intermediate positions controlled by an accurate step-motor, it is possible to observe non activations of the sensor. In this sense, the "probability" of activation of the sensor is defined as:

$$\mathcal{P}_N(E) \triangleq \frac{n_{\text{on}}}{N}. \tag{4.1}$$

$P_N(E)$ depends on the average measured electric field E and on the selected number of tuner steps N. Due to the susceptibility of the sensor to the transient peaks produced by each discrete rotation it is necessary to take into account only the activation occurred after a reasonable dwell time.

4.4.3 Sensitivity as a function of frequency and voltage supply

In order to verify the operating bandwidth, the sensor was tested by applying exciting signals characterized by a central frequency varying from 500 MHz up to 1.8 GHz and for different values of Vs. The sensor sensitivity curve is given by the average electric field amplitude measured in the working volume of the RC, as a function of the sensor activation probability 4.1. Fig. 4.3 shows the sensitivity curve of the sensor measured at the two different frequencies, 900 MHz and 1800 MHz, for $N = 50$ and Vs=9 V. The vertical bars give an indication of the uncertainty in the estimation of the field value. This means that the actual field strength that activates the sensor with a given probability $P_N(E)$ is a value comprised in the interval indicated by the vertical bars. The length of the bars is estimated by using the measured values of the σ of the loaded chamber at the considered frequencies.

Fig. 4.4 shows the electric field measured in the working volume of the RC and averaged over a complete tuner revolution as a function of frequency for different values of the probabilities of activation. Fig. **??** shows $P_N(E)$ as a function of frequency for given electric field levels.

The obtained results demonstrate that the sensor response is weakly frequency selective, since it is sensitive to modulated signals also at frequencies different from the GSM ones. This suggests the need of implementing an efficient post-processing procedure of the data coming from the sensor in order to effectively recognize the emitting GSM source [36]. In any case, it is confirmed that the activation occurs at average field levels consistent with the ones generated by GSM

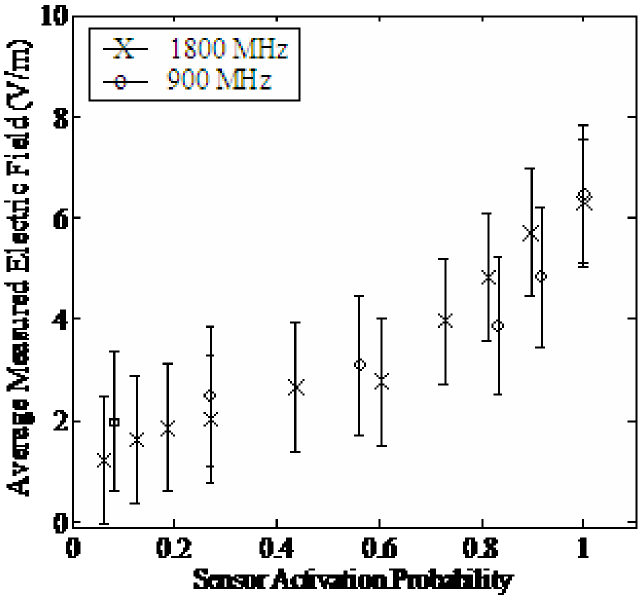

Figure 4.3: Statistical sensitivity curve and vertical bars for $f = 900$ and 1800 MHz, Vs=9 V, and $N = 50$.

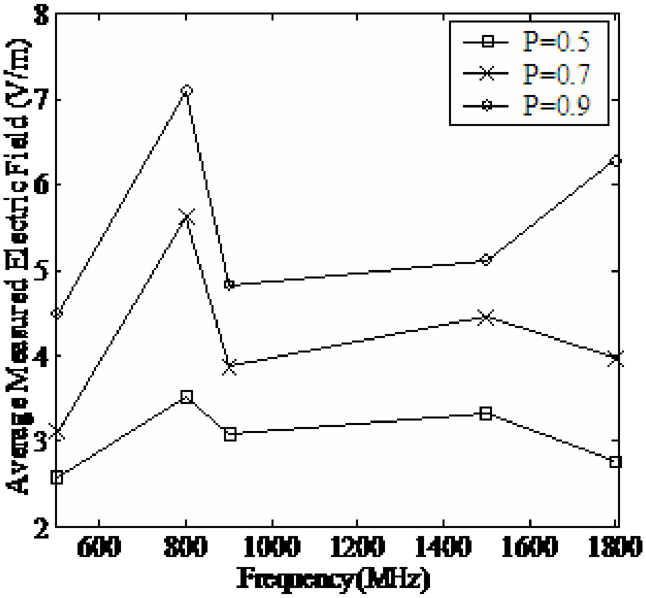

Figure 4.4: Average measured electric field necessary to obtain a given $P_N(E)$ as a function of frequency when Vs=9 V.

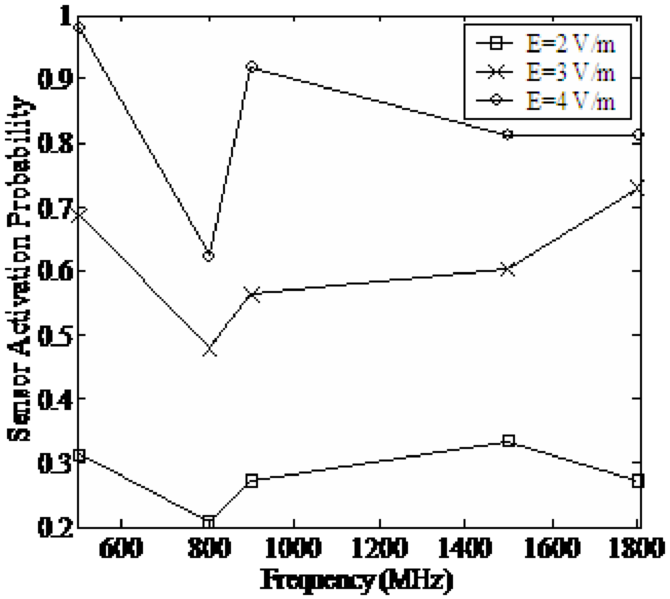

Figure 4.5: $P_N(E)$ relative to a predefined electric field as a function of frequency when Vs=9 V.

phones operating indoor. One of the most important capabilities of the sensor under test is the possibility to change the sensitivity to the exciting signal by varying the DC voltage supply. To this purpose, the analysis of the behavior of the sensor was carried out by using voltage supplies ranging from 5 V to 12 V. For example, Fig. 4.5 shows the value of the average electric field corresponding to increasing sensor activation probabilities for two different values of Vs. It can be noted that for a higher Vs the same activation probability of the sensor is obtained for a lower field level. Therefore, the sensitivity of the sensor can be enhanced by increasing Vs.

4.5 Conclusion

An innovative test procedure was developed in order to perform EM tests in an aircraft-like reverberating environment. The procedure was applied to the EM characterization of a field sensor to be used as an element of a network for the

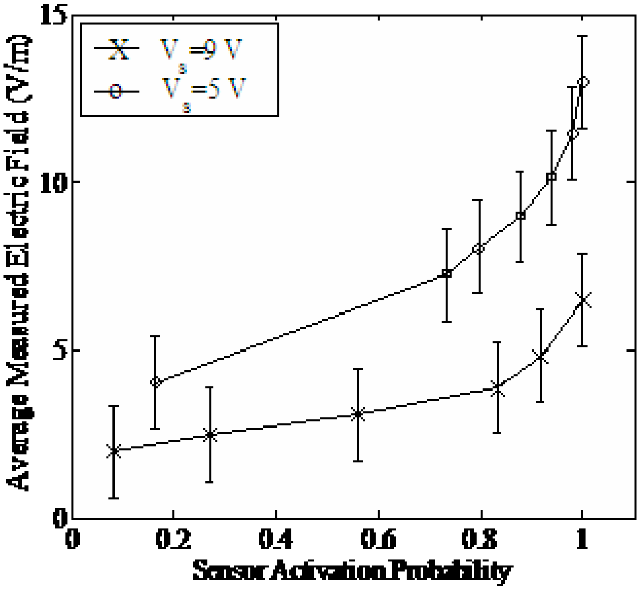

Figure 4.6: Effect of the voltage supply on the sensor sensitivity for $f = 900$, $N = 50$, and two different Vs.

localization of disturbing cellular phones aboard aircraft. Due to the nature of the considered environment, the sensitivity of the sensing unit was statistically defined to be consistent with a reverberation chamber approach, as the probability of activation in a complete rotation of the tuner of the loaded chamber. In particular, the behavior of the sensing unit was experimentally characterized in terms of frequency, average field level, and different voltage supplies. The experimental results show that the sensor is able to identify GSM-like modulated signals but it is not selective with respect to the frequency, thus requiring an efficient post-processing of the data in order to effectively recognize the emitting source. Anyway, the field levels producing the activation of the system are consistent with those generated by GSM phones operating in indoor environments and, in particular, in aircraft. Moreover, the sensitivity of the sensor can be controlled through the voltage applied to the sensing unit. The described procedure, adopted to test the specific sensor, can be successfully extended to characterize emitting devices operating in different reverberating environments. In fact, due to safety, security, privacy, or simply etiquette considerations, the use of PEDs is restricted in many other situations, generally corresponding to indoor environments.

Chapter 5

Electromagnetic Shielding of Enclosures

The Chapter presents a new method for the measurement of the shielding effectiveness of geometrically “small”, but electrically “large” enclosures. The proposed technique implements a hybrid mode-stirring technique on nested reverberation chambers. Correction factors are considered to account for the effect of the inner chamber on the radiating antenna. Numerical simulation of a 0.3 m^3 box are carried out in order to investigate the feasibility of frequency-stirring the modes inside the enclosure and to excite a correct number of modes. At least, the the use of the nested RC hybrid approach is applied to evaluate the EM shielding performance of a small satellite, simulated by means of a nested chamber loaded with an increasing number of lossy units.

5.1 Introduction

The shielding performances of an object generally depend on the testing conditions and method, leading to an uncertainty in the definition itself of the adopted parameters. In particular, the results changes with the characteristics of the incident EM field and on the geometry of the test configuration. The available standards describe alternative techniques to characterize the conducting or shielding performances of planar samples of material [2]-[4] or of enclosures [43]. One critical issue consists in correlating the results of the different characterization techniques, and in assessing the effect of the test configuration and of the intrinsic properties of the material on the shielding performance.

There is increased interest in the development, realization, and characterization of new high-performance multifunctional materials for shielding applications over a wide frequency range [44], [**?**]. However, the shielding performance of innovative materials such as nanostructured thin films, plastics with conductive fillers, or advanced composite materials is generally difficult to predict. For example, the electrical resistivity of very thin metal films depends on the technique adopted for the deposition and on the film thickness. As a result, experimental tests play an important role in estimating the shielding effectiveness (SE) and indirectly the intrinsic electrical properties of a material sample.

The IEEE Standard 299 [**?**] describes the standard method to measure the shielding performances of shelter or shielded rooms. The standard [43] provides a uniform measurement procedure and technique for determining the effectiveness of electromagnetic shielding enclosures at frequencies from 9 kHz to 18 GHz (extendable down to 50 Hz and up to 100 GHz) for enclosures having no dimensions less than 2 m. The types of inclosures covered include, but are not limited to, single-shielded or double-shield structures of various construction, such as bolted demountable, welded, or integral with a building, and made of materials such as steel plate, copper or aluminum sheet, screening, hardware cloth, metal foil, or shielding fabrics. Moreover, it includes enclosures used for testing groups of equipment, vehicles, computing systems, and smaller units whose electromagnetic emission and susceptibility require determination without disturbance from other sources. MIL-STD 285 was the common reference for many years, but the applicability of that document lessened with the advent of technological changes. Further, restructuring within U.S. Government policies and procedures has resulted in an emphasis on the use of commercial standards and the discontinuance of documents such as MIL-STD 285. The basic premise of MIL-STD 285 is still in position. The shield effect is to provide an insertion loss to outside influence. This standard offers testing based upon the performance specifications of the shield, rather than a fixed set of parameters that may not be applicable to the shield in question. Specific test procedures and frequency ranges are then selected as needed.

During the last revision of this standard, the problem related to the measurement of the SE of “small” enclosures, having linear dimensions less than 2 m, has been widely discussed. However, due to the complexity of both practical and theoretical aspects related to the measurement, the standard [43] does not deal with the case of “small” enclosures. Since 2006, the new working group 299.1 of the IEEE EMC Society has been investigating the issue, with the final scope of defining a new standard for the SE measurement of enclosures having linear dimensions smaller than 2 m, but greater than 0.1 m. Some of the critical topics that have been pointed out by the working group 299.1 concern the following aspects: Firstly, different test methods should be defined for medium enclosures with linear dimensions between 1 m and 2 m, and for very small ones with linear dimensions between 1 m and 0.1 m. For the former class of enclosures, it is considered that the test method described in [43] could be extended. For the latter one, new techniques should be proposed. Secondly, the test method should distinguish between electrically small and electrically large enclosures. The existing standard IEC 61000-4-21 on reverberation chamber (RC) test methods [13], suggests the use of RCs for SE measurements. Recent papers have discussed the technique based on nested RCs for the characterization of the SE of material sheets mounted on a conducting box [3], [4]. This approach can be applied only in case the enclosure under test behaves as an RC, that is in the frequency range where the multi-mode propagation regime can be excited. Thirdly, several papers discuss the definition of the SE referred to an enclosure [5], [6]. In fact, it is known that inside a shielding box the EM field distribution is not uniform, especially in the resonant frequency range and above. Such problem is considered in [43]: actually it is recommended to define the SE looking for the most critical positions inside the enclosure. In practice, especially in the case of “small” enclosure, the precise mapping and deterministic average of the electric and magnetic field components inside the enclosure is not feasible. At last, the new test method of the SE of “small” enclosures should fulfill the following requirements: to be easy to be implemented by technical personnel, to be not too expensive in terms of testing time and equipment, to be reliable and meaningful of the shielding performance of the enclosure in case of real EM field configurations. This paper focuses on the SE measurement of “small” enclosures in the frequency range where the multi-mode propagation regime can be excited. In particular, it discusses the use of RCs, starting from the nested RC approach described in [13], [3], [7]. The standard [13] codifies a method for the evaluation of the SE by means of nested RCs mechanically stirred. The mechanical stirring of the EM modes consists in changing the boundary conditions to the EM field by means of conductive mechanical paddles. For each position of the paddles, the spatial maxima and minima of the EM field move around the volume of the chamber resulting in the stirring of the EM modes. The main limitation of this method concerns the dimensions of the enclosure under test. In fact, since stirrers subtract plenty of room, small enclosures may not be large enough to accommodate all the necessary equipment and at the same time to respect the adequate clearance from walls and conducting surfaces to allow a correct response of the chamber.

Several studies analyze the possibility to use a frequency mode-stirring (FS) technique to produce reverberating environments [8], [9], [10]. An innovative approach was firstly proposed in [7] to measure the SE of physically small, but electrically large enclosures. The FS is an alternative mode stirring method quite fast and easy to implement. The idea is to excite a certain number of frequencies at the same time in order to stimulate a multi-mode propagation inside the structure. This method is preferable in case of small enclosures because it does not require mechanical stirrers. Moreover, a monopole antenna can be used instead of horn and log-periodical antennas as investigated in [10]. The position of the antenna does not sensibly affect the statistical characteristics of the field distribution inside the chamber. In this paper an alternative hybrid mode-stirring approach is proposed. The method consists in using two nested chambers. The FS technique is adopted to stir the EM modes inside the enclosure under test and for this reason a mechanical stirrer is not necessary in the inner chamber. The outer chamber is excited by the energy coupled from the inner chamber. An additional mechanical stirring is performed in the outer chamber in order to prevent the case that the number of modes excited by the leaking energy are not sufficient to satisfy the statistical requirements for a reverberating environment. The proposed procedure contains some considerations concerning the effect of the inner chamber on the radiating antenna. Numerical simulations are performed in order to asses the reverberating environment generated by the FS technique inside the test enclosure. Experimental tests on a 0.7 m × 0.7 m × 0.7 m aluminum box with one open side loaded with various shielding panels are the subject of ongoing work. In particular, the tests are performed by applying the proposed hybrid measurement procedure in the reverberating chamber available in the EMC Lab of the Department of Electrical Engineering at the University of Rome Sapienza.

The existing IEEE standard for measuring the effectiveness of electromagnetic shielding enclosures [43] is suitable for room-size enclosures, and as such, the method presented in [43] is not applicable for small size enclosures or cavities. As a result, the IEEE 299 standard [43] on shielding of large enclosures to currently being modified for these small enclosures.

The coaxial fixture is a commonly used measurement technique for determining far-field equivalent SE [8]-[11]. However, these approaches determine SE for only a very limited set of incident wave conditions. In most applications, are exposed to complex electromagnetic environments where fields are incident on the material with various polarizations and angles of incidence.

The standard IEC 61000-4-21 on reverberation chamber (RC) test methods [4] describes the use of mechanically stirred RCs for SE measurements. Recent papers have discussed the technique based on nested RCs for the characterization of the SE of material sheets mounted on a conducting box [8]. This approach can be applied if the enclosure under test behaves as an RC, that is in the frequency range where the multi-mode propagation regime can be excited.

Shielding effectiveness (SE) is typically used to assess the shielding property of a material, and is defined as the ratio of the transmitted power through the material to the incident power , i.e., where is the power received inside the inner chamber with a sample, and is the power received in the outer chamber with a sample in the aperture and source in the outer chamber.

This method is difficult to apply to measure the SE of electrically large but physically small enclosures due to the room necessary to the installation of antennas and stirrers inside the test box. An alternative method to reproduce a reverberating environment in a conducting enclosure is to use the FS technique [45]. It is assumed that the FS is generated by an amplitude modulated signal, for example a white Gaussian noise centered at the center frequency f_0 and having a limited agility bandwidth $\Delta f \ll f_0$. The center frequency is increased starting from the lowest usable frequency (LUF), defined in 2.

If the FS is applied to perform the SE measurement on enclosures using a nested RC approach, the main difficulty is to assure a correct reverberating environment in both chambers. Let's assume, for instance, that the FS is realized in the outer chamber. Due to the low-pass filtering behavior of enclosures, the frequency spectrum of the EM field penetrated inside the inner box can be strongly different from the one of the exciting signal. This situation results in a poor multi-mode propagation and in the failure of the required field statistical uniformity inside the inner box. A similar problem occurs if the FS is applied in the inner enclosure, therefore, a hybrid stirring technique that combines both the FS and the mechanical stirring should be implemented as described in the following.

For large enclosures, a global measure can be obtained by sampling the field at various locations in the enclosure and then take some type of average value [**?**]. However, this is not practical for physically small enclosures due to the difficulty in moving a probe with its cables. The problem can be overcome by stirring the inner chamber. To accomplish it, various technique were proposed in liter typically by an internal mechanical paddle [**?**] or using other techniques proposed in literature for RCs. In this case, the analysis (**??**) coincide with the local analysis.

Even in the case of an impinging plane wave, the shielding performance of a conducting enclosure is strongly dependent on the material, geometry, presence of apertures, and frequency of the impinging wave.

Figure 5.1: Set-up for the SE measurement of the ITO-coated: a) metallic box with the open aperture; b) metallic box with the aperture closed by the panel under test.

Figure 5.2: Sketch of the bonded (a) and unbonded (b) test configurations.

5.2 Nested reverberation chamber

The SE of an electrically large enclosure can be also approached from an operative point of view, by exploiting the properties of nested RC set-up [46], shown in Fig. **??**. In this procedure, an enclosure under test is placed inside a larger chamber. The excitation is placed in the outer chamber. Both chambers are equipped with antennas and some stirring is performed in both chambers to achieve the statistical field uniformity and to reproduce a correct reverberating environment. Tx is the transmitting antenna located in the outer chamber; Rx and Rx' are the receiving antennas inside the outer and the inner chambers, respectively. It is important to stress that the reciprocity of the system allows to exchange the role of the two antennas.

The measurement of the RC quantities is based on ensemble averages that can be determined over paddle positions in case of MS, the frequency bandwidth for the FS, or both the preceding for the HS and are indicated by the symbols $\langle\cdot\rangle$. When it is necessary to provide more information about the stirring nature either to specify its origin or the environment in which it operates, the symbols $\langle\cdot\rangle_{\text{oc}}$, $\langle\cdot\rangle_{\text{ic}}$, $\langle\cdot\rangle_{\text{FS}}$, $\langle\cdot\rangle_{\text{MS}}$, and $\langle\cdot\rangle_{\text{HS}}$ will be used. Due to the linearity of the operations,

$$\langle\langle\cdot\rangle_{\text{ic}}\rangle_{\text{oc}} = \langle\langle\cdot\rangle_{\text{oc}}\rangle_{\text{ic}}\,, \qquad \langle\langle\cdot\rangle_{\text{MS}}\rangle_{\text{FS}} = \langle\langle\cdot\rangle_{\text{FS}}\rangle_{\text{MS}} = \langle\cdot\rangle_{\text{HS}} \tag{5.1}$$

In general, the role of the chamber can be exchanged, with the only difference that is more difficult to insert a mechanical stirrer and a large antenna in the IC.

In an ideal RC the properties of the fields evaluated through an ensemble average are independent of the position. Then, the condition

$$\langle\mathbf{E}(\mathbf{r})\rangle = \langle E_x(\mathbf{r})\rangle = \langle E_y(\mathbf{r})\rangle = \langle E_z(\mathbf{r})\rangle = 0 \tag{5.2}$$

is valid for each rectangular component x, y, and z and for every position $\mathbf{r}$ included in the test volume, namely at sufficient distances from the walls, stirrers, and sources. The isotropy establishes also that the mean square value of the electric field is independent of position and

$$E_0^2 \triangleq \langle|\mathbf{E}(\mathbf{r})|^2\rangle = 3\langle|E_x(\mathbf{r})|^2\rangle = 3\langle|E_y(\mathbf{r})|^2\rangle = 3\langle|E_z(\mathbf{r})|^2\rangle. \tag{5.3}$$

Summarizing, for the purposes of this paper a chamber can be considered effectively reverberating if it satisfies the following conditions:

$$\begin{cases} \langle\mathbf{E}(\mathbf{r})\rangle = 0, & \text{RCa} \quad (5.4a)\\ \langle|E_x(\mathbf{r})|^2\rangle = \langle|E_y(\mathbf{r})|^2\rangle = \langle|E_z(\mathbf{r})|^2\rangle, & \text{RCb} \quad (5.4b)\\ \langle|\mathbf{E}(\mathbf{r})|^2\rangle = E_0^2, \qquad \forall\mathbf{r}, & \text{RCc} \quad (5.4c)\\ \chi\text{-family pdfs}, & \text{RCd.} \quad (5.4d) \end{cases}$$

The conditions (5.4) are the basis for the different criteria and tests proposed to verify the existence of a reverberating environment and to asses its performances. The interdependence among the (5.4) and the further properties that can be derived from them will be not considered in this paper.

For steady-state conditions, conservation of power requires that the dissipated power P_d equals the transmitted power P_T to derive

$$E_0^2 = \frac{Q}{\omega\varepsilon V}\langle P_\mathrm{T}\rangle = \frac{\eta_0\lambda Q}{2\pi V}\langle P_\mathrm{T}\rangle \tag{5.5}$$

where the quality factor Q is an intrinsic property of the chamber. In general, the cavity will have apertures and will contain lossy objects and at least one receiving antenna. A high Q indicates that an RC has low losses and is therefore very efficient in storing energy. For a RC Q is an important quantity because it allows prediction of the mean field strength resulting for a given input power. In addition, it provides an estimate of the chamber time constant.

One of the main consequences of (5.2) and (5.3) is that the power received by an antenna operating in an RC is independent from the type and parameters of the antenna. In fact, the received power $\langle P_\mathrm{R}\rangle$ has χ^2 distribution with two degrees of freedom (exponential) with

$$\langle P_\mathrm{R}\rangle = \langle S_r\rangle\langle A_{\mathrm{eq}_\mathrm{RC}}\rangle = \frac{E_0^2}{\eta_0}\langle A_{\mathrm{eq}_\mathrm{RC}}\rangle \tag{5.6}$$

where $\langle A_{\text{eq}_{\text{RC}}} \rangle$ is the equivalent area in a RC that is half that of an isotropic antenna in free space

$$\langle A_{\text{eq}_{\text{RC}}} \rangle = \frac{1}{2} A_{\text{eq}_0} = \frac{\lambda^2}{8\pi}. \tag{5.7}$$

By substituting (5.5) into (5.6), the average power received by a matched, lossless antenna is found to be

$$\langle P_{\text{R}} \rangle = \frac{\lambda^3 Q}{16\pi^2 V} \langle P_{\text{T}} \rangle. \tag{5.8}$$

5.3 Frequency stirring

5.3.1 Theoretical aspects

The SE of a screening structure against the electric field is defined as the ratio between the electric field magnitude in a point without the shield, E^i, and the electric field magnitude in the same shielded position with the shield present, E^t. In dB, the SE is given by:

$$SE_E = 20 \log_{10} \frac{E^i}{E^t}. \tag{5.9}$$

In general, the SE against the magnetic field (SE_H), or defined in terms of EM power (SE_P) [43] assumes different values from SE_E. In case of a planar infinite shield, illuminated by a plane wave, it results $SE_E = SE_H = SE_P$. In case of a shielding enclosure SE_E and SE_H are different, and also the value of SE defined locally, i.e. considering one specific field observing position inside the enclosure, is not meaningful of the box shielding behavior as discussed above. Actually, even in the case of an impinging plane wave, the shielding performance of a conducting enclosure is strongly dependent on the material, geometry, presence of apertures, and frequency of the impinging wave. The field distribution inside the enclosure can be very inhomogeneous due to the inside structure especially in case the dimensions of the enclosure become comparable to the wavelength of the exciting wave. In general, reflection mainly contributes to the SE against electric fields of conducting enclosures without apertures. For the shielding of the magnetic field the predominant effect is due to the mechanism of diffusion: the magnetic field induces currents in the wall of the enclosures that generate a field that is opposite to the incident one. This effect is more and more evident as the frequency associated to the incident field increases, so that an enclosure without apertures acts as a low-pass filter to the magnetic field. The low cut frequency is related to the penetration depth δ of the screen defined as:

$$\delta = \frac{1}{\sqrt{\mu_0 \pi f \gamma}}. \tag{5.10}$$

where μ_0 is the magnetic permeability of free space and γ is the conductivity of the screen. In case of an electrically large box, the nested RC approach can be applied to the SE measurement [13]. In this procedure, an enclosure under test is placed inside a larger chamber. The excitation is placed in the outer chamber. Both chambers are equipped with antennas and a mechanical stirring is performed in both chambers to achieve the statistical field uniformity and to reproduce a correct reverberating environment. The experimental set-up of this method is shown in Fig. 5.3. Tx is the transmitting antenna located in the outer chamber; Rx and Rx' are the receiving antennas inside the outer and the inner chambers, respectively.

The SE expressed in dB is [13]:

$$SE_E = 10 \log_{10} \frac{P_{ref}}{P_{EUT}}. \tag{5.11}$$

in which P_{ref} is the power coupled to the receiving antenna Rx in the outer chamber and P_{EUT} is the power coupled to the receiving antenna Rx' located inside the enclosure under test. This method is difficult to apply to measure the SE of electrically large but physically small enclosures due to the room necessary to the installation of antennas and stirrers inside the test box. An alternative method to reproduce a reverberating environment in a conducting enclosure is to use the FS technique [45]. It is assumed that the FS is generated by an amplitude modulated signal, for example a white Gaussian noise centered at the center frequency f and having a limited agility bandwidth $\Delta f \ll f$. The center frequency is increased starting from the lowest usable frequency (LUF), defined as the lowest frequency at which the specified field uniformity can be achieved, of the inner chamber up to the desired test frequency. The agility bandwidth of the signal is selected in order

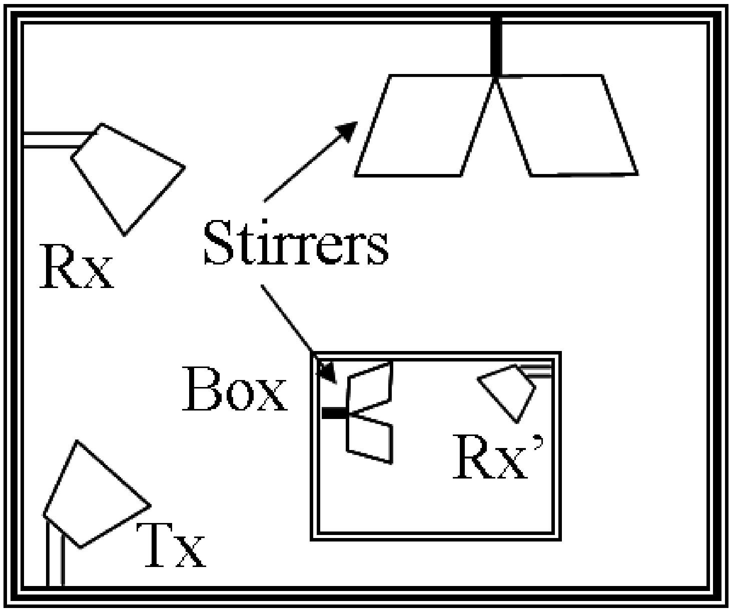

Figure 5.3: Experimental set-up of the nested chambers technique using two mechanically stirred RC.

to guarantee the generation inside the chamber of an EM reverberating environment, which requires the excitation of at least 60 modes according to [13]- [6]. The number of modes NM that are excited by an FS with agility bandwidth Δf and center frequency f, inside a rectangular enclosure of dimensions $a \times b \times d$ is given by [45]:

$$NM = \frac{8\pi abd}{c^3} f^2 \delta f. \tag{5.12}$$

where c is the velocity of light. Notice that NM depends on the center frequency f, the agility bandwidth Δf and the geometry of the enclosure. To increase NM the internal surface of the enclosure can be corrugated but this will result in the decrease of the quality factor (Q) and in a limitation of the maximum field level obtainable with the same input power [45]. Therefore, for a given enclosure and a fixed f, the best way to control NM is to play on Δf.

5.4 Proposed hybrid stirring technique

5.4.1 Experimental setup

If the FS is applied to perform the SE measurement on enclosures using a nested RC approach, the main difficulty is to assure a correct reverberating environment in both chambers. Let's assume, for instance, that the FS is realized in the outer chamber. Due to the low-pass filtering behavior of enclosures, the frequency spectrum of the EM field penetrated inside the inner box can be strongly different from the one of the exciting signal. This situation results in a poor multi-mode propagation and in the failure of the required field statistical uniformity inside the inner box. A similar problem occurs if the FS is applied in the inner enclosure, therefore, a hybrid stirring technique that combines both the FS and the mechanical stirring should be implemented as described in the following. In order to overcome this difficulties, an hybrid mode-stirring technique for the measurement of the SE is proposed. Let's consider the test configuration shown in Figures 5.4 and 5.5, in which the transmitting and the receiving antennas are labeled with Tx and Rx respectively. The inner box is the enclosure under test. The radiating source is placed in the inner chamber in which the reverberating environment is realized by exploiting a FS technique. Therefore, a mechanical stirring is not required in the inner chamber. It should be noted that if the FS is properly implemented, the statistical characteristics of the generated reverberating environment are not affected by the position of the radiating antenna. The outer room is excited by the energy coupling from the inner chamber. The outer chamber is equipped with a mechanical stirrer operating in tuned-mode by means of a stepping-motor in order to operate an additional mode-stirring. In this way both chambers are properly stirred and are characterized by a uniform statistical field distribution.

The described hybrid mode-stirring technique requires that all the quantities in the following, are to be intended as values averaged over both the frequency interval Δf defined above and over a number of steps of a complete revolution of the stirrer. According to 5.9, the SE of the test box can be rearranged in terms of the received powers from the Rx antenna without $\langle P_{RA} \rangle$ and with $\langle P_{RB} \rangle$ the

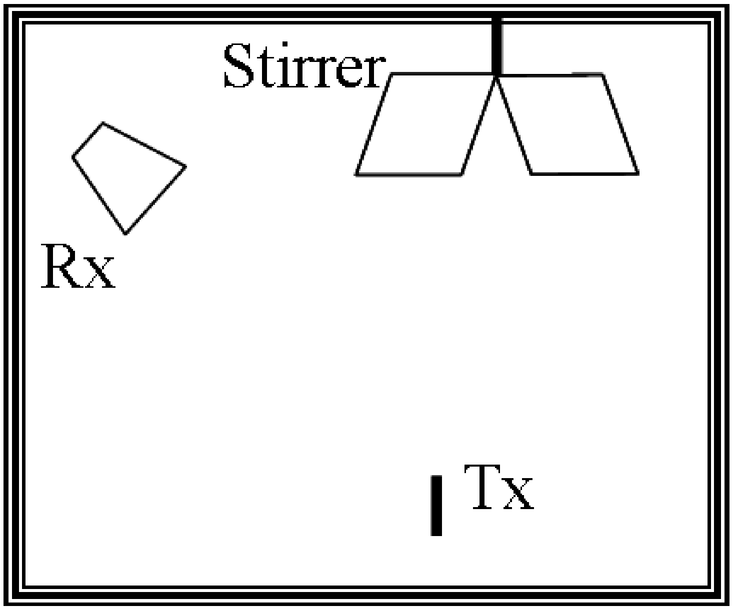

Figure 5.4: Experimental set-up: Antenna radiating in free space and box removed.

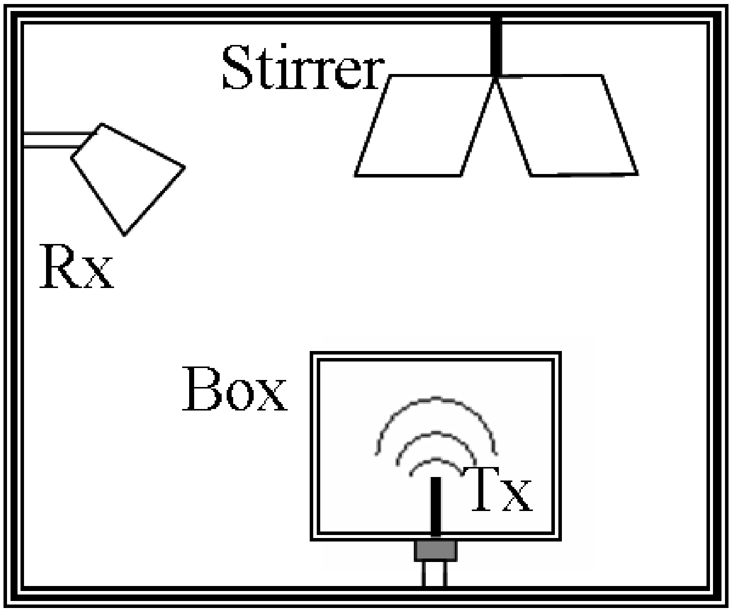

Figure 5.5: Experimental set-up: Antenna radiating in the box.

shield in place:

$$SE = 10\log_{10}\frac{\langle P_{RA}\rangle}{\langle P_{RB}\rangle}. \tag{5.13}$$

The main concern in using the definition of SE given by 5.13 is that the radiating performances of the antenna inside the test enclosure are affected by the presence of the surrounding conducting surfaces. For this reason, the expression of the SE of the inner enclosure has to be modified in order to account for the effect of the box under test on the antenna. The resulting expression for the SE in dB, yields:

$$SE = 10\log_{10}\frac{\langle P_{RA}\rangle}{\langle P^*_{RB}\rangle}. \tag{5.14}$$

where $\langle P^*_{RB}\rangle$ is the power coupled to the receiving antenna with the enclosure in place, when the input power is adjusted to compensate for the antenna mismatching generated by the presence of the enclosure itself.

Let's now consider the Tx antenna as port 1 and the Rx antenna as port 2. The quantities referring to configuration A or B of Fig. 5.4 or 5.5 are labeled with the subscript A or B respectively. In order to account for the mismatching of the Tx and Rx antennas operating inside the RCs, the reflection scattering parameters are measured in both configurations A and B. In general, due to the presence of the test box in Fig. 5.5, $\langle S_{11A}\rangle \neq S_{11B}\rangle$ and $\langle S_{22A}\rangle \neq \langle S_{22B}\rangle$. The powers delivered to the Tx antenna in configuration A and B, P_{inA} and P_{inB} respectively, and the corresponding radiated powers P_{TA} and P_{TB}, are related to the antenna efficiencies η_{1A} and η_{1B}:

$$\langle P_{TA}\rangle = \eta_{1A}P_{inA}(1-|S_{11}|^2_A) \tag{5.15}$$

$$\langle P_{TB}\rangle = \eta_{1B}P_{inB}(1-|S_{11}|^2_B). \tag{5.16}$$

In order to obtain the SE as defined in 5.14, the radiated power in the two different configurations must be the same:

$$\langle P_{TA}\rangle = \langle P_{TB}\rangle\,. \tag{5.17}$$

Combining 5.15,5.16 and 5.17, it results:

$$P^*_{inB} = \frac{\eta_{1A}(1-|S_{11}|^2_A}{\eta_{1B}(1-|S_{11}|^2_B)}P_{inA}. \tag{5.18}$$

The power delivered to the Tx antenna can be controlled from the operator. Therefore P^*_{inB} can be adjusted depending on P_{inA} in order to satisfy 5.18. The only unknowns are η_{1A} and η_{1B}, which would be coincident either in case of ideal lossless antennas, or in case the test box does not affect the radiating performances of the inner antenna. In general, it can be assumed $\eta_{1A}/\eta_{1B} \approx 1$ if the Tx antenna is small enough so that it couples weakly with the conductive walls. Moreover, in configuration A and B, at the receiving side it results:

$$\left\langle P_{measA(B)} \right\rangle = \eta_{1A(B)} \left\langle P_{RA(B)} \right\rangle (1 - |S_{22}|^2_A (B)) \tag{5.19}$$

$$\left\langle P_{measA(B)} \right\rangle = |S_{21}|^2_A (B) P_{inA(B)} \tag{5.20}$$

where $P_{RA(B)}$ is the power coupled to the Rx antenna and $P_{measA(B)}$ is the power measured by a matched sensor attached to Rx. For the antenna efficiencies η_{2A} and η_{2B} hold considerations similar to the ones discussed as regards η_{1A} and η_{1B}. Therefore, the received powers P_{RA} and P^*_{RB} yields:

$$P_{RA} = \frac{|S_{21}|^2_A P_{inA}}{\eta_{2A}(1 - |S_{22}|^2_A)} \tag{5.21}$$

$$P^*_{RB} = \frac{|S_{21}|^2_B P^*_{inB}}{\eta_{2B}(1 - |S_{22}|^2_B)}. \tag{5.22}$$

From 5.21 and 5.22, the SE in 5.14 can be written as:

$$\mathrm{SE} = 10 \log_{10} \left(\frac{\eta_{2B}}{\eta_{2A}} \frac{1 - |S_{22}|^2_B}{1 - |S_{22}|^2_A} \frac{|S_{21}|^2_A}{|S_{21}|^2_B} \frac{\eta_{1B}}{\eta_{1A}} \frac{1 - |S_{11}|^2_B}{1 - |S_{11}|^2_A} \right). \tag{5.23}$$

Assuming $\eta_{1A} \approx \eta_{1B}$, $\eta_{2A} \approx \eta_{2B}$, expression 5.23 gives:

$$\mathrm{SE} = 10 \log_{10} \left(\frac{1 - |S_{22}|^2_B}{1 - |S_{22}|^2_A} \frac{|S_{21}|^2_A}{|S_{21}|^2_B} \frac{1 - |S_{11}|^2_B}{1 - |S_{11}|^2_A} \right). \tag{5.24}$$

5.4.2 Numerical analysis and simulation results

In order to investigate the behavior of a conductive box when the FS is operated, some numerical simulations with the commercial software CST Microwave Studio [**?**] are carried out. The feasibility of the method is discussed. In particular, a perfectly conducting (PEC) box of dimensions 0.7 m $\times 0.7$ m $\times 0.7$ m with one wall made of aluminum is modeled. The EM field is recorded in nine probe positions randomly located around the volume of the box. A Gaussian pulse excitation is applied to calculate the frequency transfer function of the box up to 5 GHz. The results are then post-processed to calculate the output of the system when a Gaussian noise limited in the agility bandwidth, is applied. The parameter Ψ is chosen as an indicator of the field uniformity, according to [45]. Ψ is given by the ratio between the maximum average power density over the minimum power density recorded in the cavity and averaged over the agility bandwidth Δf. In dB, Ψ reads:

$$SE = 10log\frac{\langle P_{max}\rangle_{\Delta f}}{\langle P_{min}\rangle_{\Delta f}}. \tag{5.25}$$

A rule of thumb states that $\Psi \approx 2.5\sigma$, where σ is the standard deviation of the field ratios. For example to have $\sigma = 3$ dB, Ψ should not be grater than 7.5 dB [45]. Figures 5.6 and 5.7 show the minimum agility bandwidth necessary at each center frequency to excite at least 60 modes inside the box, and the frequency spectrum of function Ψ obtained on the simulated data respectively. Figures 5.8 and 5.9 show the frequency spectra of Ψ for the same set of data processed considering $\Delta f = 20$ MHz and $\Delta f = 100$ MHz respectively, over the considered frequency range. In can be noted that an enhancement of the field uniformity is obtained for a larger Δf, as expected.

5.4.3 Conclusion

In this Chapter an innovative hybrid mode-stirring approach for the evaluation of the SE of small enclosures, using the nested RC method is proposed. The nested reverberation chambers method is modified in order to apply the frequency mode-stirring technique to the inner chamber, being the enclosure under test. The FS is adopted to excite the inner chamber, while a mechanical stirrer in the outer chamber, helps in stirring the coupled energy and in achieving the required field statistical uniformity. Correction factors are considered to account for the effect of the inner chamber on the radiating antenna. We stress out that the FS in the outer

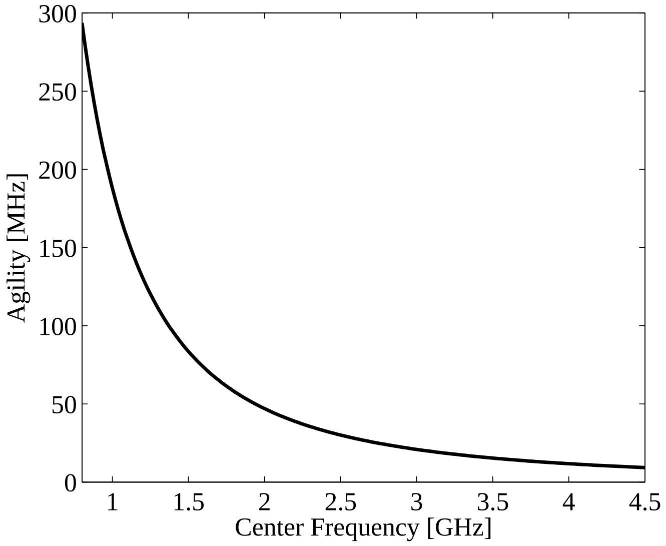

Figure 5.6: Minimum agility bandwidth required to obtain $NM = 60$.

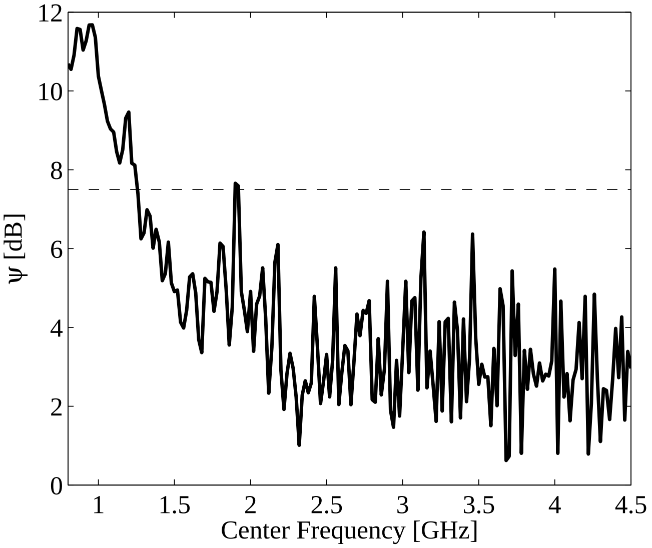

Figure 5.7: Function Ψ corresponding to the minimum agility bandwidth required to obtain $NM = 60$.

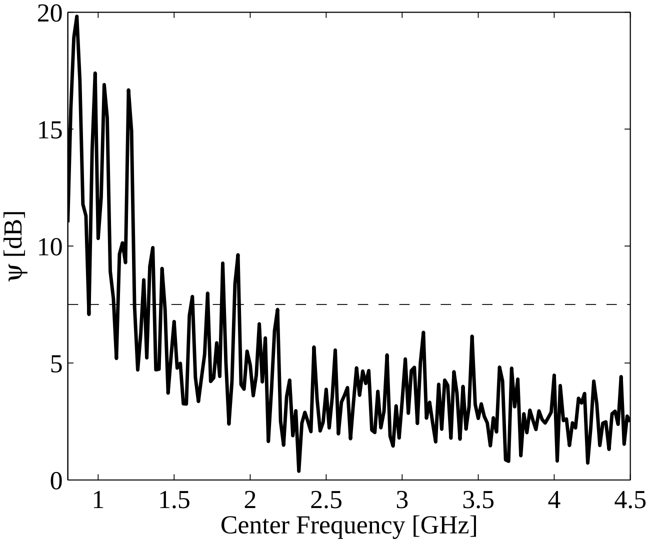

Figure 5.8: Frequency spectrum of Ψ obtained for $\Delta f = 20$ MHz.

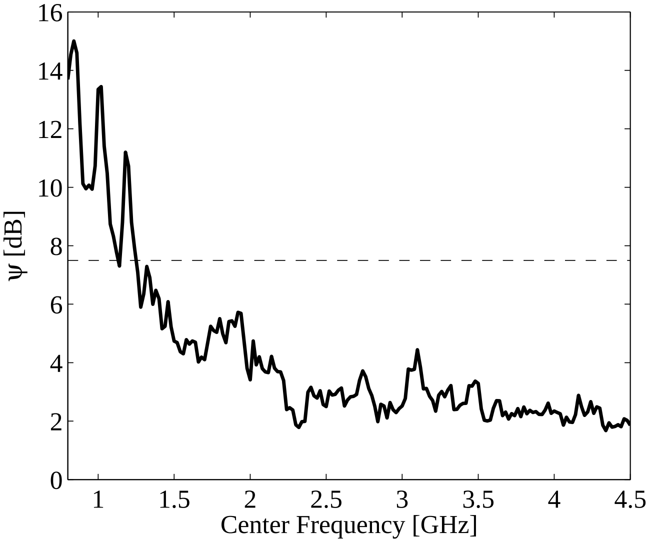

Figure 5.9: Frequency spectrum of Ψ obtained for $\Delta f = 100$ MHz.

chamber may be not sufficient to assure the necessary multi-mode propagation in the inner chamber, due to the frequency selective behavior that generally characterize enclosures of different materials and shape and including apertures, seams and slots. The main advantage of the proposed method is that the installation of mechanical stirrers inside the enclosure under test is not required. The results of the numerical simulation of a 0.3 m^3 box indicate the feasibility of the FS to perform measurements of the SE of enclosures having the largest dimension less than 2 meters, in the multi-mode resonant frequency range. The post-processing of the results indicated the possibility to frequency-stir the modes inside the enclosure and to excite a correct number of modes. The objectives of future investigations will be the applications of the described innovative method to characterize the shielding performances of a test enclosure, and the comparison with the data obtained by using the fully FS approach proposed in [47].

5.5 Test of artificial satellites in loaded chambers

5.5.1 Introduction

“Miniaturized” or “small” satellites are artificial satellites of limited size and weight that are usually categorized as: minisatellites (with a “wet mass” including fuel between 100 and 500 kg), microsatellites (10-100 kg), nanosatellites, (1-10 kg), picosatellites (less than 1 kg). The size of such satellites strongly depends on the installed equipment and on the mission purpose, but in general their linear dimensions are smaller than 2 m. EMC-related issues are becoming more and more critical due to the widespread use of composite materials as replacement for metals in aerospace applications and to the increasing complexity of electrical and electronics apparatus and systems. A crucial aspect at design and system development levels concerns the estimation of the electromagnetic (EM) energy coupling with a satellite structure, considering also the effect of the internal loading produced by onboard systems and devices. The IEEE standard 299 describes a technique to measure the shielding effectiveness (SE) of an enclosure having any linear dimension greater than 2 m [43]. The working group IEEE 299.1 is developing new approaches for the SE measurement of enclosures having all linear dimensions smaller than 2 m and greater than 0.1 m. The proposed solutions are based on the use of nested reverberation chambers (RCs) [47], [13]. The scope of this paper is to propose the use of the nested RC measurement method to assess the EM shielding performance of a small satellite (linear dimension less than 2 m). Such measurement will provide information on the worst-case average attenuation that the satellite structure can provide against a statistically uniform and isotropic EM field at radio-frequency. The SE data could be then used at the design level in order to optimize the EM interference protection and the system layout taking into account the potential screening effect of the satellite structure. The test set-up considered in this paper is based on the use of two nested RCs, as shown in Figure 5.10: the outer chamber (OC) produces a stirred field incident on the inner chamber (IC) corresponding to a physical model of the satellite EM properties. For this type of test, some authors have suggested to adopt the frequency stirring technique [47]. A variant of such technique consists in the hybrid approach introduced in [48] that combines the advantages of the frequency stirring and of the mechanical stirring. A further improvement proposed in this paper consists in loading the IC to reproduce the effects on the field intensity and distribution due to the presence of objects and devices onboard [24].

5.5.2 Experimental set-up and obtained results

In order to demonstrate the validity of the proposed approach, preliminary experimental tests were performed in the RC of the EMC Laboratory of the Department of Electrical Engineering of Sapienza University of Rome, assuming that the physical model of a satellite is represented by an aluminum box of dimensions $70 \times 70 \times 70$ cm with a 24×15.5 cm aperture centered in one wall. The box is placed in a $3.5 \times 3 \times 2.5$ m RC equipped with a controlled mechanical stirrer running 12 steps over a complete rotation. The transmitting antenna (Tx), placed in the OC, is fed by a frequency swept signal generated by a vector network analyzer, while the receiving one (Rx) is mounted inside the test box, which is not equipped with mechanical stirrers. A 25 W microwave amplifier is inserted inside the measurement chain in order to increase the dynamic range of the tests. The preliminary results shown in the following refer to the 1-4 GHz frequency range. The received signals are averaged over the stirrer positions and over a 100 MHz agility bandwidth [48], also compensating for the antenna mismatches that need to be estimated in each configuration. The quality factor of the IC Q_{IC} is modified by introducing in the IC a variable number n_{RL} of pyramids of absorbing material assumed as a representative load (RL) for a satellite or for an enclosure [49]. The repetition of the measurements after moving the RLs in different random positions confirmed that, as expected from the theory, the effect of the RLs depends exclusively on their characteristics (volume and density) and, for a given unity, on n_{RL}. Figure 5.11 shows the variations of the Q_{IC} spectrum with n_{RL}. The same concept is summarized by the average Q_{IC} in Figure 5.12, in which the experimental data are compared with the theoretical curve obtained by identifying the best fit to the RL contribution and assuming that it acts in parallel to the intrinsic QIC0 (empty unloaded satellite). Following this approach, any desired value of Q_{IC} can be reached. The final paper will analyze the Q values that can be presumably found in practical situations. Just to provide some preliminary examples, Figures 5.11-5.13 report also the Q_{IC} resulting when a computer mother board or a commercial power supply with many output cables is inserted inside the IC. Such effects are approximately equivalent to those produced by one piece of RL. Figure 5.13 shows that, as expected, the actual SE of an enclosure depends on its Q. Notice that the study has been carried out on a low shielding enclosure (mainly due to the presence of the aperture) in order to emphasize this phenomenon, but the results will be extended to other configurations. In particular, in the final paper a composite material enclosure will be considered.

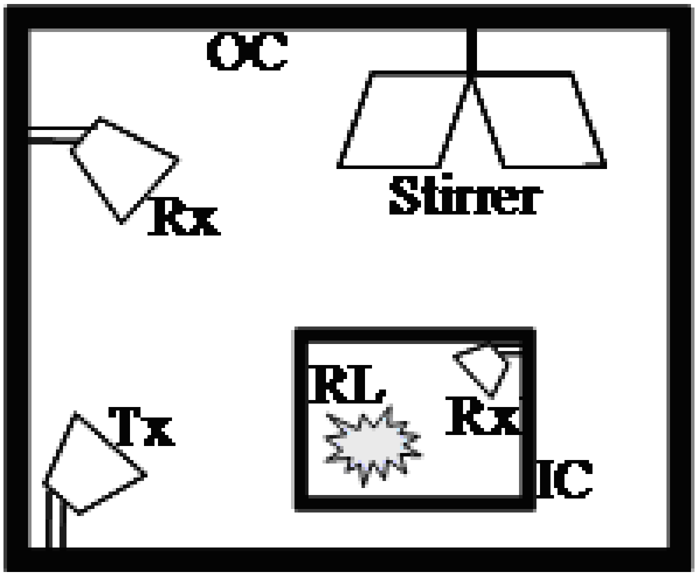

Figure 5.10: Configuration of the experimental set-up. The IC is nested in the OC and contains the RL. The field is stirred in both the chambers by the hybrid technique combining the mechanical stirrer with a frequency stirring.

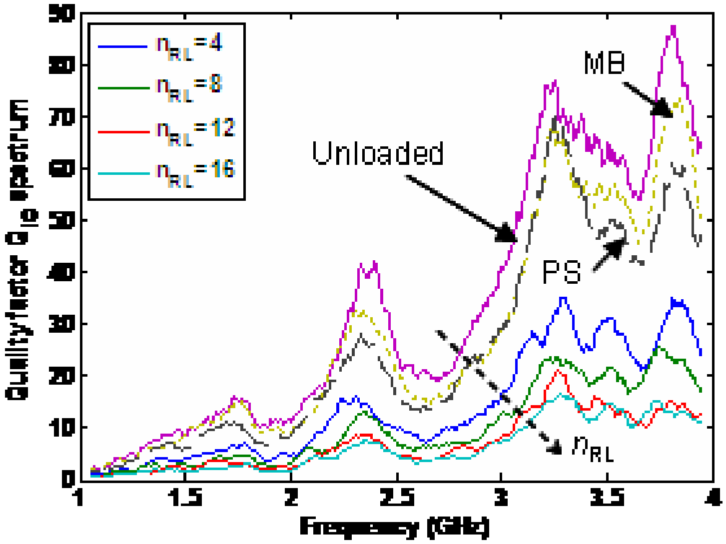

Figure 5.11: Q_{IC} spectrum for different n_{RL} values. The curves are lower for increasing n_{RL}. The dotted and the dashed lines refer to the Q_{IC} measured for a computer mother board (MB) and for a power supply (PS), respectively.

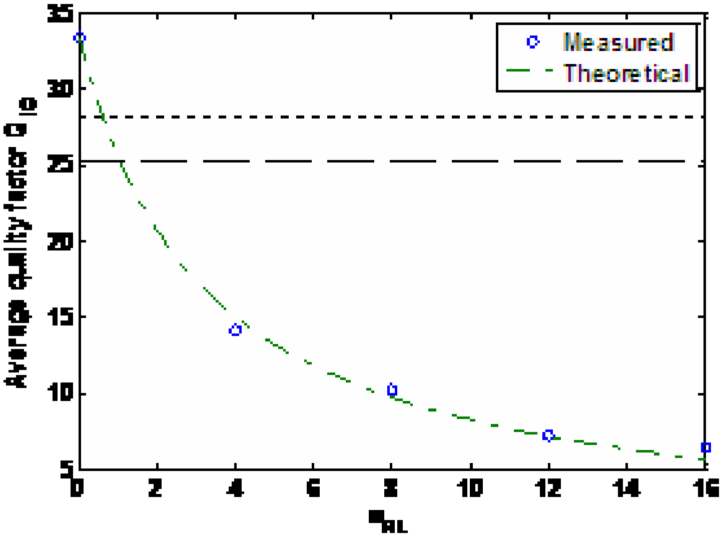

Figure 5.12: Relationship between n_{RL} and the average Q_{IC}. The experimental data are well fitted by the theoretical model. The dotted and the dashed lines refer to the mother board and power supply Q_{IC}.

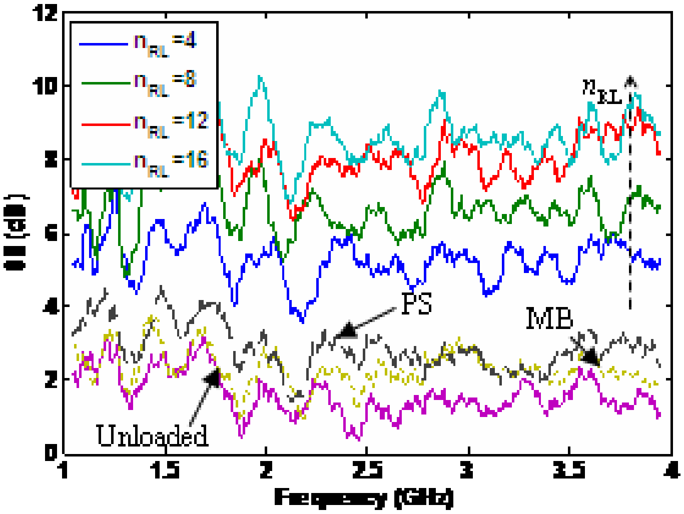

Figure 5.13: SE for different n_{RL} values. The curves are higher for increasing n_{RL}. The dotted and the dashed lines refer to the SE measured for a computer mother board (MB) and for a power supply (PS), respectively.

Chapter 6

Materials for the Electromagnetic Shielding

6.1 Introduction

Transparent electromagnetic (EM) screens can be used for the radio-frequency (RF) shielding of displays of electrical and electronic apparatus, of electromedical devices, of portable electronic equipment like cellular phones, of aircraft or building windows. A specific application was supported by the Italian Environment Protection and Technical Services Agency (APAT) in the framework of a research project aimed to adopt such facilities to reduce the propagation of the EM fields through building windows to protect from undesired effect both people and electronic apparatus. Several technological solutions have been proposed in the past, but it is necessary to consider that for the presented application the key aspects are the costs and the possibility to apply the new solutions to variable situations without excessively modifying the existing structures. Therefore, such solutions should comply with the building standards and common practice. In particular, some investigated technologies are extensions of special products used for energy saving purposes.

One of the most critical aspects in the practical realization of transparent metals samples for electromagnetic shielding at radio frequency is due to the fact that finite dimension screens provide maximum attenuation of the incident field only if they are perfectly bonded to ground. This would suggest that the metal layers in the screening structure should be connected to the reference ground by direct contact. Most of the commercial windows are based on metallic meshes that are expensive, bulky, and heavy.

Another critical aspects concerns the definition and the characterization of the shielding performances of the transparent materials. Commercial products are generally provided of data sheet describing the expected shielding performances in some frequency ranges. However, it is well known that the shielding properties of a screen generally depend on the testing method, and in particular on the characteristics of the incident EM field and on the geometry of the test configuration. The available standards describe alternative techniques to characterize the conducting or shielding performances of planar samples of material [2]-[4] or of enclosures [5]. One critical issue consists in correlating the results of the different characterization techniques, and in assessing the effect of the test configuration and of the intrinsic properties of the material on the shielding performance. The existing IEEE standard for measuring the effectiveness of electromagnetic shielding enclosures [1] is suitable for room-size enclosures, and as such, the method presented in [1] is not applicable for small size enclosures or cavities. As a result, the IEEE 299 standard [1] on shielding of large enclosures to currently being modified for these small enclosures.

A technique commercially used to realize transparent windows consists in the deposition of micrometer-thin films of transparent semiconductor oxide, like the Indium Titanium Oxide (ITO), on a plastic or glass surface [1] [**?**].

The scope of this paper is to characterize both experimentally and by means of numerical simulations the performances of two families of commercial solutions. The first is based on ITO-coated

The results of three different test techniques are analyzed and compared. Moreover, the effect of the perfect bonding of the shield is investigated. Numerical simulations are performed by using a three-dimensional (3D) finite-difference time-domain (FDTD) procedure. The ITO film is simulated applying the thin-layer model described in [6], using the data of electrical conductivity obtained by the experimental characterizations.

The coaxial fixture is a commonly used measurement technique for determining far-field equivalent SE [8]-[11]. However, these approaches determine SE for only a very limited set of incident wave conditions. In most applications, are exposed to complex electromagnetic environments where fields are incident on the material with various polarizations and angles of incidence

The standard IEC 61000-4-21 on reverberation chamber (RC) test methods [4] describes the use of mechanically stirred RCs for SE measurements. Recent papers have discussed the technique based on nested RCs for the characterization of the SE of material sheets mounted on a conducting box [8]. This approach can be applied if the enclosure under test behaves as an RC, that is in the frequency range where the multi-mode propagation regime can be excited.

6.2 Alternative characterization techniques

6.2.1 Four-point probe method

The sheet resistance of a sample with conductivity σ, resistivity ϱ, and thickness d is

$$R_{\square} \triangleq \frac{1}{\sigma d} = \frac{\varrho}{d}. \tag{6.1}$$

The sheet resistance (in DC) of the thin conductive film is measured applying the four-point method, as described in [2]. The measuring system is constituted by a Signatone S301 four-point probe stand and a Keitley 2400 source meter. The probe head, secured to the stand arm, has four collinear equally spaced tungsten carbide tips, which are placed in contact with the conducting sample. As the injected direct current flows through the specimen between the two outer tips of the probe, the voltage between the inner ones is recorded. Then, the sheet resistance is calculated from the measured current and voltage applying proper correction factors, which depend on the specimen and probe geometry.

The values of d and σ_0 are used to predict the SE of the conducting film. Since

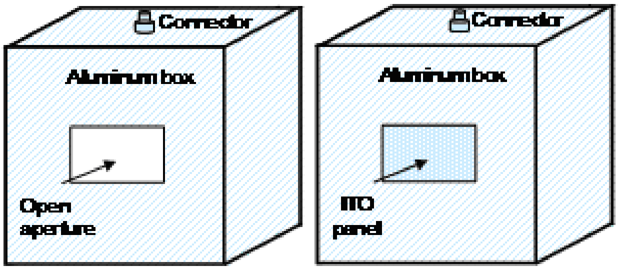

Figure 6.1: Set-up for the SE measurement of the ITO-coated: a) metallic box with the open aperture; b) metallic box with the aperture closed by the panel under test.

the shielding coating is electrically thin up to about 10 GHz, it results that in the considered frequency range, the SE is nearly constant and can be expressed in dB by the following approximated formula [7]:

$$\mathrm{SE}_{\mathrm{dB}} = 45.51 + 20\log_{10}\sigma_0 d = 45.51 - 20\log_{10} R_{\square}. \tag{6.2}$$

6.2.2 Coaxial TEM cell

In order to verify the previous results, the SE of the ITO film is directly measured in the frequency range from 40 MHz to 8 GHz with a coaxial transmission line method, based on the ASTM D4935 standard [3]. The ASTM D4935 standard describes one of the most exploited techniques for the SE measurement of planar materials. It uses a flanged coaxial sample holder (FCSH), which is an enlarged coaxial line with an interrupted inner conductor. The material to be tested is sandwiched between the two halves of the cell that are fastened by non conducting screws or by a pressure system. The main drawback of the standard fixture is the narrow frequency band of operation. According to [3], the maximum working frequency of the test set-up is 1.5 GHz. In order to overcome such limitation, a new coaxial cell for measurements up to 8 GHz was presented in [7]. The performances and the critical aspects of the new fixture were discussed testing different shielding materials.

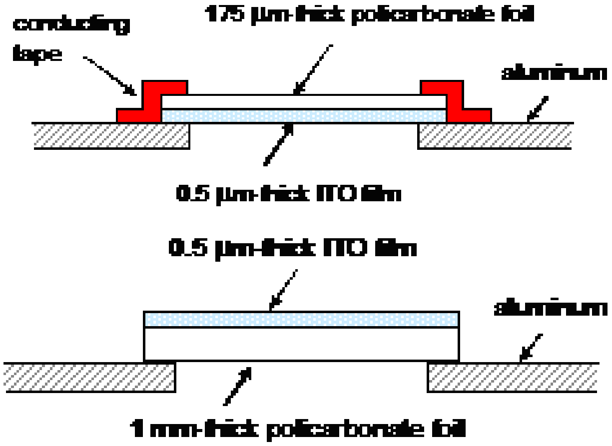

Figure 6.2: Sketch of the bonded (a) and unbonded (b) test configurations.

6.3 Antenna Effects

Even though all the shielding parameters can be estimated from the knowledge of P_{T} and the measurement of P_{R}, these quantities are not totaly accessible for the equipment used in practice. The difference between the incident power available to the transmitting antenna P_{in} and the power reflected by the antenna is equal to the net input power accepted by the antenna. This can be determined by a VNA controlling the transmitting and receiving antennas. Moreover, some of the power is dissipated by resistive losses in the antenna and the remainder is radiated. The ratio of the total radiated power to the net power is defined as the radiation efficiency η of the antenna. The extension of the model also to the received and measured powers leads to

$$P_{\mathrm{T}} = \eta_{\mathrm{T}} P_{\mathrm{in}}(1 - |S_{11_0}|^2), \qquad P_{\mathrm{M}} = \eta_{\mathrm{R}} P_{\mathrm{R}}(1 - |S_{22_0}|^2) \tag{6.3}$$

where S_{11_0} and S_{22_0} are the free space reflection coefficients of the transmitting and receiving antennas, respectively. The antenna efficiency η_{T} and η_{R} are extremely difficult to measure and have often assumed to be unitary. The standard consider ...

The property (5.6) is very useful in the choice of the detection system, as it establishes that the received power far from the walls does not depend on the antenna characteristics. A large antenna can mitigate the effect of the non uniformities in the stirred field, but such dimensions must not influence the reverberation properties. In fact, Fig. shows. A small antenna is better also because it can inserted also in a small enclosure. Moreover, [**?**] has shown that the normal component of $\mathbf{E}(\mathbf{r})$ at the surface of a wall not close to another wall has the same statistics of a probe placed anywhere in the cavity with double mean-square value?. This allows the use of a wall-mounted small monopole antenna [47] to monitor the field inside a RC and in particular in the IC. However, in this case the reflections at the antenna terminals can be excessive due to the poor impedance match. The same problem can be encountered for any kind of antenna, as the reflections are different with respect to free space and depends on the chamber configuration. In fact, the reflections measured at the input of an antenna consists of two components: the intrinsic antenna reflection and the reflections due to the transmitted signal interacting with the chamber and returning to the antenna. The average electromagnetic environment inside a mode-stirred chamber behaves like free space [6] with the average wave impedance similar to that of free space, then, on average, the antenna behaves as if it were in free space. Thus, the magnitude of the average reflection coefficients $|\langle S_{11}\rangle|$ and $|\langle S_{22}\rangle|$ measured in a mode-stirred chamber and averaged should be similar to the magnitude of the free-space reflection coefficients:

$$|\langle S_{11}\rangle| \simeq |S_{11_0}|, \qquad |\langle S_{22}\rangle| \simeq |S_{22_0}| \tag{6.4}$$

If the coupling is $\langle |S_{21}|^2\rangle$, then the corrected coupling $\widetilde{S}_{21}$ is given by [47], [**?**]

$$\widetilde{S}_{21} = \frac{\langle |S_{21}|^2\rangle}{m_1 m_2} \tag{6.5}$$

where

$$m \triangleq 1 - |S_{22_0}|^2 \simeq 1 - |\langle S_{22}\rangle|^2 \tag{6.6}$$

is the mismatch coefficient estimated from $\langle S_{22}\rangle$.

The procedure has to be repeated for each antenna, even when they are identical because the other objects and particularly the small enclosure can influence the input impedances. The quantities referring to configuration A or B of Fig. 2(a) or 2(b) are labeled with the subscript A or B, respectively. The Tx antenna is connected to port 1 and the Rx antenna to port 2. In order to account for the mismatching of the Tx and Rx antennas operating inside the RCs, the reflection scattering parameters are measured in both configurations A and B. In general, due to the presence of the test box in Fig. 2(b), $\langle S_{11_\mathrm{A}}\rangle \neq \langle S_{11_\mathrm{B}}\rangle$ and $\langle S_{22_\mathrm{A}}\rangle \neq \langle S_{22_\mathrm{B}}\rangle$.

The powers delivered to the Tx antenna in configuration A and B, $P_{\mathrm{in}_\mathrm{A}}$ and $P_{\mathrm{in}_\mathrm{B}}$ respectively, and the corresponding radiated powers $P_{\mathrm{T}_\mathrm{A}}$ and $P_{\mathrm{T}_\mathrm{B}}$, are related to the antenna efficiencies $\eta_{\mathrm{T}_\mathrm{A}}$ and $\eta_{\mathrm{T}_\mathrm{B}}$:

$$\langle P_{\mathrm{T}_\mathrm{A}}\rangle = \eta_{\mathrm{T}_\mathrm{A}} P_{\mathrm{in}_\mathrm{A}} (1 - |\langle S_{11_\mathrm{A}}\rangle|^2) \tag{6.7}$$

$$\langle P_{\mathrm{T}_\mathrm{B}}\rangle = \eta_{\mathrm{T}_\mathrm{B}} P_{\mathrm{in}_\mathrm{B}} (1 - |\langle S_{11_\mathrm{B}}\rangle|^2) \tag{6.8}$$

In order to obtain the SE as defined in (6), the radiated power in the two different configurations must be the same:

step-rotation stirrer (SRS) and continuous-rotation stirrer (CRS). The simplification given from the properties (6.4) and () are always used in literature [6], [**?**] when an antenna effect is considered. However, they introduce a useles approximation when the actual data of S_{11} and S_{22} are available, as it may happen when a VNA is used and the measurement of S21 and S11 and S22 are performend in the same conditions. Therefore, the correction was applied

$$\widetilde{S}_{21} = \frac{S_{21}}{1 - |S_{22}|^2} \tag{6.9}$$

and

$$\frac{\langle P_\mathrm{R}\rangle}{\langle P_T\rangle} \simeq \langle \widetilde{S}_{21}\rangle \simeq \left\langle \frac{S_{21}}{(1 - |S_{11}|^2)(1 - |S_{22}|^2)} \right\rangle \tag{6.10}$$

For measurement set-up without sufficient information to apply (6.10) as the CRS the use of the simplification is still necessary. The SE is defined in terms of active power as

$$\mathrm{SE_{dB}} = 10 \log_{10} \frac{P_{source}}{P_{shield}} \tag{6.11}$$

where Psource is the power received when the screen is not present (Fig. 7(a)), and Pshield when it is in place (Fig. 7(b)).

The voltage-scattering parameters S11, S22, S21 are measured in the two configurations shown in Fig. 2(a) and (b): the subscripts 1 and 2 correspond to the ports connected to the Tx and Rx antennas, respectively. The SE in dB is expressed in terms of the voltage-scattering parameters by [13]:

$$\mathrm{SE} = 10\log_{10}\left[\left(\frac{1-|S_{22}|_B^2}{1-|S_{22}|_A^2}\right)\left(\frac{|S_{21}|_A^2}{|S_{21}|_B^2}\right)\left(\frac{1-|S_{11}|_B^2}{1-|S_{11}|_A^2}\right)\right]. \tag{6.12}$$

in which the averages are performed in frequency over an opportune agility bandwidth $\Delta\varphi$, and over a complete rotation of the mechanical stirrer. The sub-scripts A and B in eq.(3) refer to the measurement set-ups of Figs. 2(a) and (b), respectively.

6.4 Frequency Stirring

The possibility to use a frequency mode-stirring (FS) technique to produce reverberating environments was initially proposed in [9]-[11], and more recently implemented in the new approach presented in [12] for the measurement of the SE of small enclosures. The FS is an alternative mode-stirring method quite fast and easy to implement. The idea is to excite a certain number of frequencies at the same time in order to stimulate a multi-mode propagation inside the structure without the use of mechanical stirrers.

The one main concern with frequency stirring is what bandwidth (BW) should be used in the frequency averaging process. If the BW is too large and the Q of the outer reverberation chamber changes significantly over that BW, then the frequency averaging approach is not valid

place a small mechanical paddle inside the enclosures placing a small probe in the center of the small enclosure as is done in [?] poses difficulties.

Firstly, the SE is estimated considering an agility bandwidth $\Delta\varphi$ =200 MHz and without mechanical stirring in the outer chamber. The frequency averages in (3) are computed using nf samples in each $\Delta\varphi$-wide interval, in the range from 1 GHz to 4.5 GHz. Figs. 4(a) and (b) show the results obtained in the bonded and unbonded configurations, for nf=200 and nf=1000, respectively. Notice that as nf increases, the number of modes excited increases, thus improving the reverberating performances of the chamber. The results correlate within 2 dB - 4 dB with the ones shown in Fig.1, obtained using the coaxial-waveguide set-up. Both curves in Fig.1 and 4(b) are slowly decreasing because the shielding film is thin and characterized by sheet resistance of 13.35 $\Omega/\Box$, with thickness of only 0.5 μm. The resonant characteristics of the curves shown in Fig. 6.5(b) confirm that the EM environment is not optimally stirred. Moreover, the SE measured in the RC is in average 3 dB - 5 dB lower than the one measured with the coaxial waveguide, due to the effect of the finite size of the panel under test, and of the multidirectional illumination.

There must be a significant number of modes in the enclosure such that we have independent frequency samples for the chosen averaging bandwidth. The mode density D(f) in the enclosure is approximately [**?**], [3]

$$Df \simeq \frac{8\pi V f^2}{c^3} \tag{6.13}$$

so the number of modes in a bandwidth N is the product of the mode density times the bandwidth. In order for the frequency stirring approach to be valid, the enclosure must is able to support at least 60 modes for a given enclosure size and frequency. Thus, the minimum frequency that this procedure can be used for is a given enclosure size is [?]:

$$f_{min} = c\sqrt[3]{\frac{90}{4\pi V}} \tag{6.14}$$

where V is the volume of the small enclosure. there is no upper frequency. However, the upper frequency may be governed by the test equipment used (VNA, cables, and antennas).

achieve this, BW must satisfy the following (see [2] for details):

$$BW \gg \frac{c^3}{8\pi V f^2} \tag{6.15}$$

This assumes that BW is somewhat greater than the single-mode bandwidth f /Q , but this is the typical case since f /Q is generally small for large Q [7]. If the bandwidth is too large then resonances in the actual shielding response of the small enclosure would be smoothed out. The second issue is associated with the outer reverberation chamber. If the BW is too large and the Q of the outer reverberation chamber changes significantly over that BW, then the frequency averaging approach is not valid.

6.5 Mechanical Stirring

Successively, the SE of the ITO screen is measured activating the mechanical stirrer in the outer RC, but without applying the frequency stirring. Both the bonded and unbonded configurations are considered. Expression (**??**) is applied considering at each frequency an average over 25 different positions of the mechanical stirrer. The obtained results are reported in Fig. 6.6. The high number of resonances affecting the SE spectrum is due to a poorly overmoded propagation inside the inner box that results in a not sufficiently stirred EM field. This confirms that the use of only the external mechanical stirring is not suitable to perform SE measurements.

6.6 Hybrid Mechanical and Frequency Stirring

Finally, the SE is measured in the nested RCs, applying both the frequency and the mechanical stirring, according to the procedure described in [13]. The measured data are averaged over an agility bandwidth ??=200 MHz, using nf=1000 samples in each ??-wide interval, and over 25 positions of the tuner. The obtained results shown in Fig. 6.7 demonstrate that the hybrid stirring does contribute to improve the measurement. In fact, the curves of Fig. 6.7 are much smoother than the ones in Fig. 6.5(b). Moreover, it results that the SE in the bonded configuration well correlates with the one shown in Fig. 6.4, within 5 dB.

6.6.1 Characteristics of transparent materials

6.6.2 Optical characteristics

The solar energy approximately consists of radiations in the wavelength interval $0.3 \div 3$ μm. This interval includes the UV ($0.3 \div 3$ μm), visible ($0.4 \div 0.8$ μm), and thermal radiations (above 0.8 μm). Any material, including transparent materials, partially reflects and absorbs this radiation. For example, a standard float” glass reflects approximately transmits the the 83% of the incident power in the internal

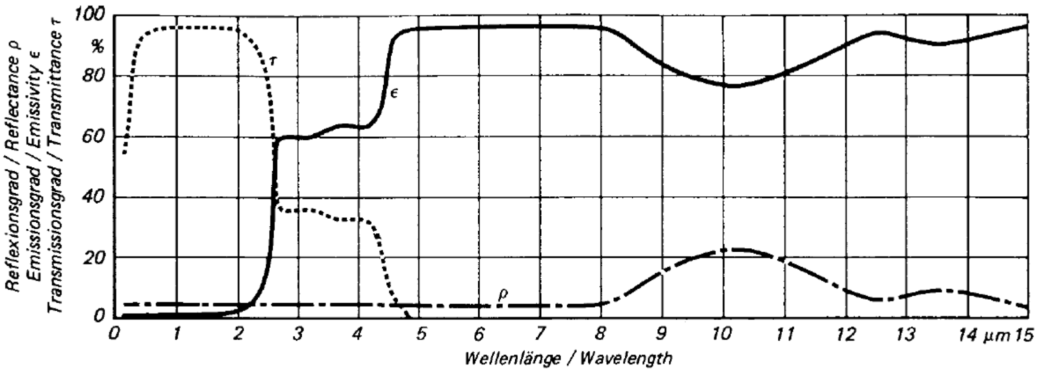

Figure 6.3: Typical spectral transmittance of common glass.

environment. Spectral transmittance of glass Fig. 6.3.

The standard EN 410:2000 [**?**] determines the luminous and solar characteristics of glazing for a radiation whose incident angle is approximately normal and using the relative spectral distribution of the of the solar radiation and in particular of the standard illuminant D_{65} defined by the International Commission on Illumination [**?**].

The optical spectral transmittance and reflectance of a material for a given incidence angle are respectively given by

$$T(\lambda) \triangleq \frac{E_\mathrm{i}^2(\lambda)}{E_\mathrm{t}^2(\lambda)}, \qquad R(\lambda) \triangleq \frac{E_\mathrm{i}^2(\lambda)}{E_\mathrm{r}^2(\lambda)} \tag{6.16}$$

where E_i is the amplitude of the incident electrical field, E_t is the amplitude of the transmitted field, and E_r is the amplitude of the reflected field. Then, the absorbance corresponds to

$$A(\lambda) = 1 - T(\lambda) - R(\lambda). \tag{6.17}$$

All the relevant optical parameters, as T_v and g, of a system can be derived from these quantities. The knowledge of the value of a characteristic allows to automatically derive the values for different glass thicknesses or substrates from the analytical method described in [?].

The solar direct energy transmittance (DET) of the solar energy is given by the formula

$$T_{\mathrm{e}} \triangleq \frac{\sum_{\lambda=300}^{2500} S_\lambda T(\lambda)\Delta\lambda}{\sum_{\lambda=300}^{2500} S_\lambda \Delta\lambda} \simeq \sum_{\lambda=300}^{2500} S_\lambda T(\lambda)\Delta\lambda \tag{6.18}$$

while the the direct reflectance is

$$R_{\mathrm{e}} \triangleq \frac{\sum_{\lambda=300}^{2500} S_\lambda R(\lambda)\Delta\lambda}{\sum_{\lambda=300}^{2500} S_\lambda \Delta\lambda} \simeq \sum_{\lambda=300}^{2500} S_\lambda R(\lambda)\Delta\lambda \tag{6.19}$$

where S_λ is the relative spectral distribution of the solar radiation provided in specific tables in [?] that were derived from [**?**] together with the corresponding values of $S_\lambda\Delta\lambda$ for specific wavelength intervals $\Delta\lambda$. Such values are organized to ensure that $\sum_{\lambda=300}^{2500} S_\lambda\Delta\lambda = 1$ and, consequently, to allow the approximations in (6.18) and (6.19).

The main function of a window is to admit visible light, but only a portion of solar radiation contain visible components. This is measured by the light transmittance given by the formula

$$T_{\mathrm{v}} \triangleq \frac{\sum_{\lambda=380}^{780} D_\lambda T(\lambda)V(\lambda)\Delta\lambda}{\sum_{\lambda=380}^{780} D_\lambda V(\lambda)\Delta\lambda} \simeq \sum_{\lambda=380}^{780} D_\lambda T(\lambda)V(\lambda)\Delta\lambda \tag{6.20}$$

where D_λ is the relative distribution of the standard illuminant D_{65} and V is the spectral luminous efficiency that defines the fotometry reference observer [**?**]. The values $D_\lambda V(\lambda)\Delta\lambda$ are given for $\Delta\lambda = 10$ nm to produce an unitary denominator. Analogously, the light reflectance is

$$R_{\mathrm{v}} \triangleq \frac{\sum_{\lambda=380}^{780} D_\lambda R(\lambda)V(\lambda)\Delta\lambda}{\sum_{\lambda=380}^{780} D_\lambda V(\lambda)\Delta\lambda} \simeq \sum_{\lambda=380}^{780} D_\lambda R(\lambda)V(\lambda)\Delta\lambda. \tag{6.21}$$

The UV region contain the subintervals UV-B ($280\div315$ nm) and UV-A ($315\div380$ nm) that are represented in [?] by the relative spectral distribution of UV solar radiation U_λ and by the term $U_\lambda\Delta\lambda$ for $\Delta\lambda = 5$ nm to give the ultraviolet transmittance

$$T_{\mathrm{UV}} \triangleq \frac{\sum_{\lambda=280}^{380} U_\lambda T(\lambda)\Delta\lambda}{\sum_{\lambda=280}^{380} U_\lambda \Delta\lambda} \simeq \sum_{\lambda=280}^{380} U_\lambda T(\lambda)\Delta\lambda. \tag{6.22}$$

The secondary internal q_{i} and external q_{e} heat transfer factors correspond to the heat exchange of the fraction of the incident solar radiation absorbed by the material. Such fraction given by (6.17) is transmitted for convection and for far IR radiation towards both the internal and the external environments. This leads to a complex analysis for multiple material window systems, but a single pane can be modeled by

$$q_{\text{i}} = A_{\text{e}}e - q_{\text{e}} = 1 - T_{\text{e}} - R_{\text{e}} - q_{\text{e}} = A_{\text{e}}\frac{h_i}{h_{\text{e}} + h_i}. \tag{6.23}$$

The internal and external heat transfer coefficients h_{i} and h_{e} depend on the boundary conditions as the position, wind velocity, environment and superficial temperatures. To provide a practical approach, [?] identifies the following conventional conditions: vertical orientation, air cavities without ventilation, natural convection in the internal environment, external wind velocity 4 m/s, corrected emissivity $\varepsilon_{\text{e}} = 0.837$. As far as the internal surface corrected emissivity ε_{i} is concerned, it has to be measured according to the standards EN 673 or prEN 12898. For the sodico calcico non rivestito glass and the vetro borosilicato glass it is possible to assume $\varepsilon_{\text{i}} = 0,837$, whereas lower values should be considered only for superficial coatings with a higher $R(\lambda)$ in the far IR whitout a formazione di condensa. These hypotheses give the normalized values

$$h_{\text{e}} \simeq 23 \text{ W/(m}^2\text{K)}, \qquad h_{\text{i}} \simeq 3.6 + \frac{4.4\varepsilon_{\text{i}}}{0.837} \simeq 8 \text{ W/(m}^2\text{K)} \tag{6.24}$$

and then the approximation

$$q_{\text{i}} \simeq 0.26A_{\text{e}}. \tag{6.25}$$

The total solar energy transmittance (solar factor), defined in the EN 410 as

$$g \triangleq T_{\text{e}} + q_{\text{i}} \tag{6.26}$$

is the most used luminous and solar parameter, especially in the commercial data sheets. Practically, it is the fraction of incident solar radiation admitted through a window (both directly transmitted and absorbed) and subsequently released inward (absorbed and reradiated). All the following alternative expressions can be derived from (6.24) and (6.25):

$$g = T_e + A_e\frac{h_i}{h_e + h_i} \simeq T_e + 0.26A_e \tag{6.27}$$

$$g = T_e(1 - \frac{h_i}{h_e + h_i}) + \frac{(1 - R_e)h_i}{h_e + h_i} \simeq 0.74T_e - 0.26R_e + 0.26. \tag{6.28}$$

Unfortunately, also due to the adoption of other non-European standards, several different terms, symbols, and estimation methods can be encountered (solar heat gain, passive solar gain, G-value, SF, SHGC, TT, γ). In particular, the expression solar heat gain coefficient (SHGC) is more used in the United States [**?**]

The following definitions are not included in the standard in EN 410 and are normally derivable from the above presented parameters. The shading coefficient (SC)

$$\text{SC} \triangleq \frac{\text{SHGC}}{\text{SHGC}_0} \simeq \frac{\text{SHGC}}{0.87} = 1.15 \cdot \text{SHGC} \leq 1. \tag{6.29}$$

is an older concept that is still used, particularly in the United States, to compare the solar factor, indicated as SHGC, of a glass assembly to that of single pane glass that has

$$\text{SHGC}_0 \simeq 0.87. \tag{6.30}$$

Considering that the remission operates and higher wavelengths, the SC information can be split for short and long wavelengths:

$$\text{SC}_{\text{sw}} \simeq \frac{T_{\text{e}}}{0.87}, \qquad \text{SC}_{\text{lw}} = \text{SC} - \text{swSC}. \tag{6.31}$$

When a material is used for thermal insulation a relevant parameter is the light efficiency

$$\text{LE} \triangleq \frac{T_{\text{v}}}{\text{SC}} \tag{6.32}$$

while when only the visible light performance is interesting, the glare reduction

$$\text{GR} \triangleq 1 - \frac{T_{\text{v}}}{T_{\text{v}_0}} \simeq 1 - \frac{T_{\text{v}}}{0.87} \tag{6.33}$$

allows a comparison with the visible light transmission of a reference situation (approximately 0.87 for a standard glass).

6.6.3 Thermal characteristics

The European standards on glass and window assembly and the window industry specifications of are based on the concept of thermal transmittance or U-factor U

in the central area of a material. The U-factor includes heat transfer by conduction, convection, and radiation through the window assembly but does not include the energy transfer due to the solar radiation and does not consider the edge effects due to the thermal bridge through the air space cavity of a insulating glazing or through the window frames. In stationary conditions the power flowing through a unitary surface with a temperature difference ΔT between the two glazing sides is

$$Q = U\Delta T. \tag{6.34}$$

The U-factor is measured in W/m^{2}K but it is common to find definitions based on Btus per square foot per hour per degree Fahrenheit. Moreover, some countries and old standards use the symbol K or the reciprocal

$$R = \frac{1}{U}. \tag{6.35}$$

The global U of a window system is

$$U = h_\mathrm{e} \parallel h_\mathrm{w} \parallel h_\mathrm{i} \tag{6.36}$$

where the term h_w depends on the system structure. For a single wall, pane, or material with thickness d_m and thermal conductance Λ_m the heat transfer coefficient is

$$h_\mathrm{m} = \frac{\Lambda_\mathrm{m}}{d_\mathrm{m}} \tag{6.37}$$

and for several material layers of different materials with thickness d_{m_i} it results from

$$h_\mathrm{w} = \parallel_i h_{\mathrm{m}_i} = \frac{1}{\sum_i \frac{d_{\mathrm{m}_i}}{\Lambda_{\mathrm{m}_i}}}. \tag{6.38}$$

For instance, for a vetro sodo-calcico $\Lambda_\mathrm{m} \simeq 1$ W/mK. The presence of air space cavities between the transparent materials produces a specific heat transfer coefficient

$$h_\mathrm{s} = h_\mathrm{r} + h_\mathrm{g} \tag{6.39}$$

depending on the filling gas conductivity h_g and on the T_m è la temperatura media assoluta dell'intercapedine; e1 e e2 sono il fattore di emissione corretto a Tm through the radiation transfer coefficient

$$h_{\mathrm{r}} = \frac{4\sigma_{\mathrm{SB}} T_{\mathrm{m}}^{3}}{\frac{1}{\varepsilon_1} + \frac{1}{\varepsilon_2} - 1} \tag{6.40}$$

where σ_{SB} is the Stefan-Boltzmann constant. Hence, the total heat transfer coefficient becomes

$$h_{\mathrm{w}} = \|_i \, h_{\mathrm{m}_i} \, \|_i \, h_{\mathrm{s}_i} = \left(\sum_i \frac{d_{\mathrm{m}_i}}{\Lambda_{\mathrm{m}_i}} + \sum_i \frac{1}{h_{\mathrm{s}_i}} \right)^{-1} . \tag{6.41}$$

The cavity radiative contribution to the thermal exchange can be very high, up to the 60% of the total power. The use of low-E coatings can reduce the IR ($\lambda >?$) exchange between transparent materials, leading the $\varepsilon_{\mathrm{n}} = 0.8 \div 0.9$ of an uncoated glass to $\varepsilon_{\mathrm{n}} < 0.2$. For more than one cavities, U needs to be derived by means of an iterative procedure [**?**].

6.7 Characterization of ITO films

The transparent shielding panel characterized in this paper is a commercial 175 μm-thick policarbonate foil, coated on one surface with an Indium-Titanium-Oxide (ITO) film having thickness of 0.5 μm. The analysis is performed in the frequency range from 1 GHz to 4.5 GHz. In the following, the results of three different experimental techniques are compared and discussed.

6.7.1 Four-point probe method

The measurement is repeated by positioning the test-probe in five different points of the sample in order to check the uniformity of the ITO film and the repeatability of the measurements. The results are reported in Table 6.1. The calculated average sheet resistance $< R_{\mathrm{s}} >$ is 13.35 ohms/square with a standard deviation of 2.5%. It results that the ITO film is characterized by a direct-current (dc) conductivity σ_0 of about 150 kS/m, considering that the average thickness of the coating over the whole sample surface is $d = 0.5$ μm. The values of d and σ_0 are used to predict the SE of the conducting film. Since the shielding coating is electrically thin up to

Table 6.1: Sheet resistance measured in different points of the ITO-coated samples.

Measurement points	Voltage/Current [V/A]	Rs [ohms/square]
1	2.92	13.23
2	2.92	13.23
3	2.98	13.5
4	3.05	13.8
5	2.86	12.96

about 10 GHz, it results that in the considered frequency range, the SE is nearly constant and can be expressed by the following approximated formula. From (6.2) it results SEdB = 23 dB.

6.7.2 Coaxial TEM cell

Fig. 6.4 shows the measured SE frequency spectra from 1 GHz to 4.5 GHz. Note that the SE is almost constant over the whole frequency range and its average value is around 21 dB. This confirms that the absorption phenomena are negligible and the shielding is mainly due to reflection. Besides, the obtained result agrees satisfactorily with the one predicted by (6.2).

6.7.3 RC

In this paper, measurements of the SE of a transparent window coated with an ITO thin film are carried out in a RC applying the procedure described in [13]. The set-up for the SE measurement of the screening panels consists in a 3 mm-thick aluminum box of dimensions 70 cm × 70 cm × 70 cm, with a 24 cm × 15.5 cm aperture centered in one wall (Fig.2(a)). The panel under test is mounted over the aperture (Fig.2(b)). The box is placed in a 3.5 m × 3 m × 2.5 m RC equipped with a mechanical stirrer. The transmitting antenna (Tx) is positioned inside the

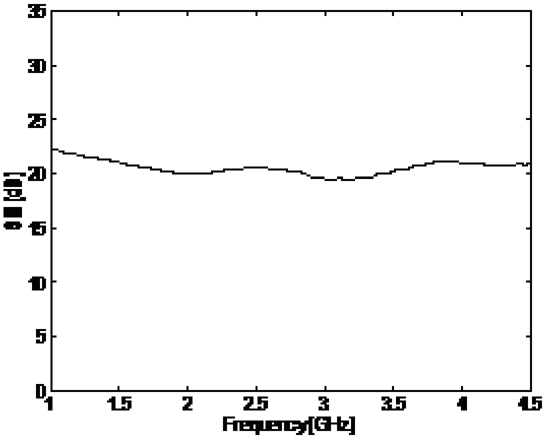

Figure 6.4: SE frequency spectrum of the ITO sheet measured by using the coaxial waveguide test set-up, in the 1 GHz - 4.5 GHz frequency range.

outer RC and the receiving one (Rx) is mounted inside the test box, which is not equipped with mechanical stirrers. Tx is fed by a frequency stirred signal, which is generated by using a vector network analyzer, whose receiving port is connected to the Rx antenna. A 25-W-power amplifier is inserted inside the measurement chain in order to increase the dynamic range of the test configuration.

In the configuration of Fig. 2(b), the measurements are performed with the screening panel bonded and unbonded, as shown in Figs. 3(a) and (b), respectively. In the first configuration, the ITO surface of the panel is directly contacted to the aluminum border of the aperture. In the latter one, a 1-mm-thick seam is created between the conducting face of the panel and the box border. In the following, a comparative analysis of the effect of the mechanical, frequency and hybrid stirrings on the measurement of the SE of the panel is presented.

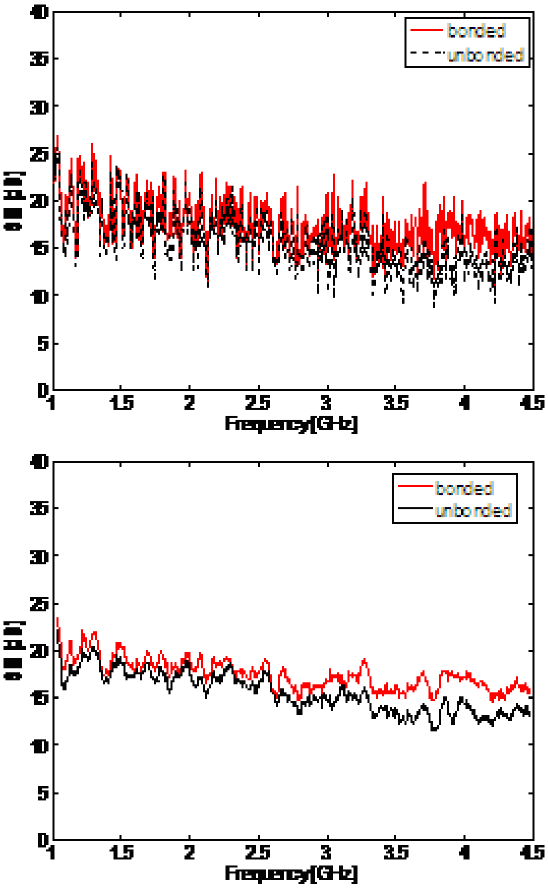

Figure 6.5: Frequency spectra of the measured SE of a commercial ITO sheet by using nested RCs with frequency stirring of modes, in bonded and unbonded configurations. The agility bandwith is ??=200 MHz, and the number of equally spaced samples used for the frequency stirring is nf=200 (a) and nf=1000 (b).

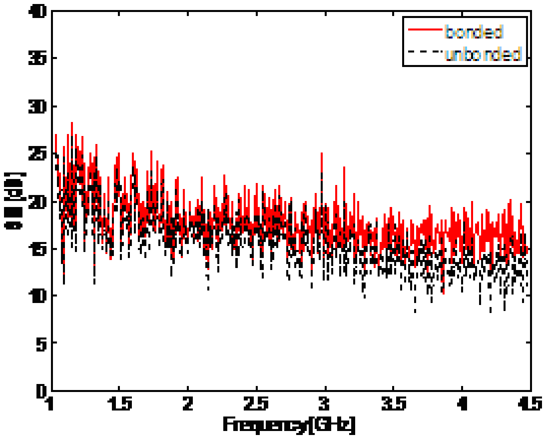

Figure 6.6: Frequency spectra of the measured SE of a commercial ITO sheet by using nested RCs with mechanical stirring in the outer chamber, in bonded and unbonded configurations.

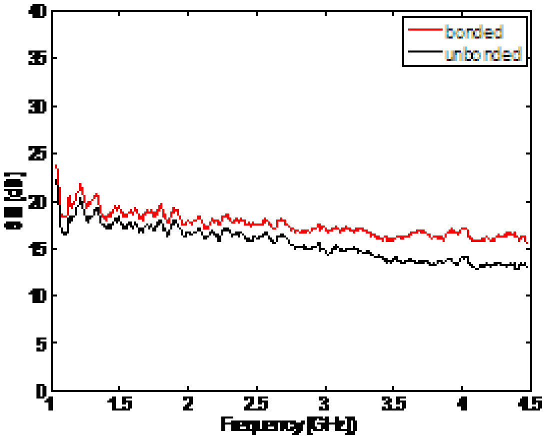

Figure 6.7: Frequency spectra of the measured SE of a commercial ITO sheet by using nested RCs with frequency and mechanical stirring of modes, in bonded and unbonded configurations. The agility bandwith is ??=200 MHz, the number of frequency samples is nf=1000, the number of tuner steps in one complete rotation is 25.

6.8 Numerical models and simulations

6.8.1 3D-FDTD Modeling

Numerical simulations are performed by applying the three-dimensional (3D) finite-difference time-domain (FDTD) procedure described in [6] and [14]. The 70-cm-side box is discretized by using the space step of 1.67 cm. The 3 mm-thick aluminum walls are considered as perfect-electric conducting (PEC), whereas the shielding panel is simulated by applying the thin-layer model described in [6], using the value of the dc electrical conductivity measured in Section II.A using the four-point probe method (σ_0=150 kS/m). UPML-boundary conditions [15] are positioned at six cells from the discrete model of the box, which is assumed to lay over an infinite PEC plane. The two different box configurations sketched in Figs. 6.8(a) and 6.8(b) are simulated. The box is illuminated by a plane wave impinging orthogonally to the face with the aperture. The calculation is performed using the time-step of 27.9 ps and running $6{\cdot}10^5$ iterations. The SE of the ITO panel against the y-component of the electric field in a point $\mathbf{r}$ is given by:

$$\text{SE}_{\text{panel}}(\mathbf{r},f)=\left|\frac{E_{y_{ob}}(\mathbf{r},f)}{E_{y_{cb}}(\mathbf{r},f)}\right| \tag{6.42}$$

where E denotes the Fourier transform of the signal $\mathcal{E}_y(\mathbf{r},t)$ in open-box and in closed box conigurations. The corresponding SE of the box closed with the ITO panel is computed by:

$$\text{SE}_{\text{box}}(\mathbf{r},f)=\left|\frac{E^i_y(\mathbf{r},f)}{E_{y_{cb}}(\mathbf{r},f)}\right| \tag{6.43}$$

in which is the incident electric field in P without the box. In order to obtain an average estimate of the shielding performance of the enclosure, the SEs in eqs. (6.42) and (6.43) are evaluated in the nine points reported in Table 6.2. The obtained data are then averaged to calculate the mean value.

6.8.2 Simulation Results

First, the set-up of Fig. 6.8(a) is considered. The frequency spectra of the average SE of the box and of the 70 cm × 70 cm ITO panel are shown in Figs. 6.9(a)

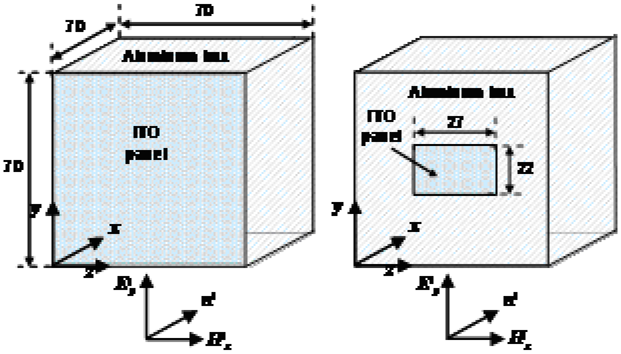

Figure 6.8: Schematic configuration of the modelled boxes illuminated by a plane wave (all dimensions are in cm): a) 70 cm × 70 cm ITO panel; b) 27 cm × 22 cm ITO panel.

Table 6.2: Positions of the 9 observation points for the calculation of the SE.

Position	x [cm]	y [cm]	z [cm]
P1	35	26	35
P2	35	26	35
P3	35	26	35
P4	45	40	35
P5	45	40	35
P6	45	40	35
P7	58	47	35
P8	58	47	35
P9	58	47	35

and (b), respectively. The multiresonant characteristic of the obtained curves is due to the fact that in the considered 1 GHz - 4.5 GHz frequency range the box is electrically large. It is noted that in average the SE of the ITO panel is nearly 5 dB higher than the SE of the PEC box having one wall made with the ITO-coated polycarbonate. This is due to the fact that in the considered frequency range both the enclosure and the ITO panel are electrically large.

Next, the calculation is repeated considering the configuration shown in Fig. 6.8(b), in which the aperture loaded with the ITO panel has dimensions 27 cm × 22 cm. It results that in average the SE of the box (Fig. 6.10(a)) is higher than the SE of the finite size-panel (Fig. 6.10(b)). Moreover, the SE of the box is characterized by a decreasing trend because at frequencies up to 1 GHz - 2 GHz, the aperture is not electrically large. At higher frequencies the SE spectra of Figs. 6.10(a) and 6.10(b) are very similar. From the comparison of the spectra of Figs. 6.9(b) and 6.10(b), it is observed that in average the SE of the smaller panel (27 cm × 22 cm) is higher than that provided by the larger panel (70 cm × 70 cm) of nearly 1 dB - 2 dB.

6.8.3 Consideration on ITO shielding performances

The EM shielding performances of commercially available transparent ITO film coated on a polycarbonate foil have been characterized both experimentally and by numerical simulations. The obtained results demonstrate that the dc sheet resistance measurements can be used to predict with accuracy within 3 dB the theoretical low-frequency value of the shielding effectiveness of a planar sample of material having infinite dimensions and illuminated by a plane wave with normal incidence. The new test method proposed to extend the limit of applicability of the ASTM standard D4935-89 is very accurate and provides an estimate of the theoretical SE, which is a function of only the material intrinsic properties and of the shield total thickness. The results of the two previous methods well correlate with the data obtained by applying the FS technique to the nested RCs test method described in the IEC standard 61000-4-21. In particular, it is demonstrated that the test results obtained in the RC agree within 5 dB with the one obtained using

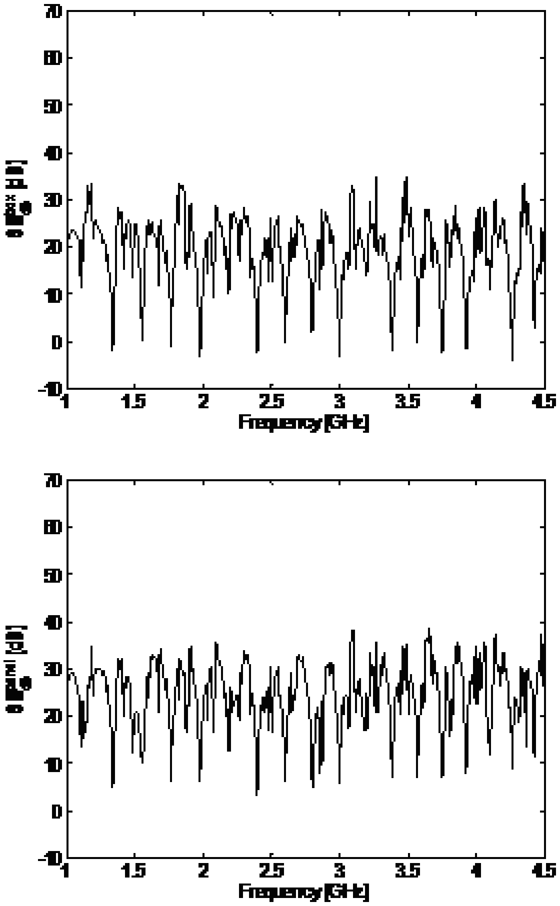

Figure 6.9: Frequency spectra of the SE of the box of Fig.7(a) (a) and of the 70-cm-side squared ITO panel (b).

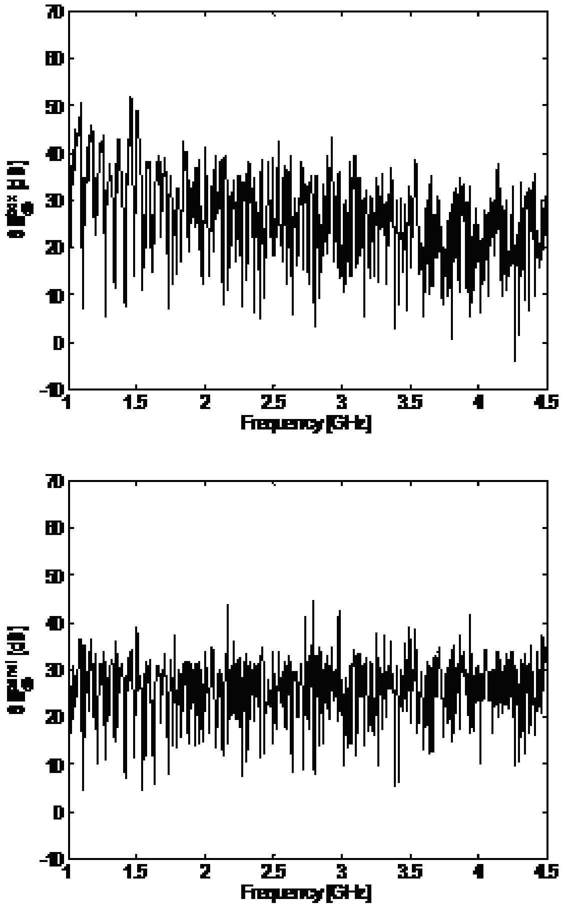

Figure 6.10: Figure 9. Frequency spectra of the SE of the box of Fig.7(b) (a) and of the 27 cm × 22 cm ITO panel (b).

the coaxial waveguide configuration, if the EM environment is optimally stirred. It is shown that the best RC's performance is achieved combining the frequency and mechanical stirrings of modes. Finally, the results of numerical simulations performed applying the 3D-FDTD method are well in line with the experimental data. It is confirmed that as the size of the tested panel decreases, the average SE estimated using a resonant enclosure increases.

The EM shielding performances of commercially available transparent ITO film coated on a polycarbonate foil have been characterized both experimentally

6.9 Shielding performances of solar control films

Some films currently used for thermal control in windows can be successfully adopted to reduce the EMI and in particular the human exposure to the electromagnetic pollution. The three different adopted techniques allow the experimental assessment of the shielding performances of the analyzed films in different conditions. The experimental characterization of each film permits to identify some correlations between electromagnetic shielding and optical transparency. The knowledge of the film structures (material, thickness and number of the layers) could permit to analytically predict and optimize the achievable electromagnetic, optical and thermal performances by using the developed simulation codes.

The first presented measurement was obtained by using the flanged coaxial waveguide in the EMC Laboratory of according to the standard ASTM-D-4935 “Standard Test Method for Measuring the Electromagnetic Shielding Effectiveness of Planar Materials”. The developed test set-up permits to overcome the frequency limits of the standard up to 8 GHz. Table 6.3 summarizes the average SE of different available films in the frequency bandwidth 0.5÷8 GHz. The same table shows the values of the visible light transmittance T_{v} as defined by the international standards and reported in the film data sheets.

The optical and electromagnetic performances depend on the material, the thickness and the number of layers of the realized films: for the same film typology the highest SE is normally characterized by a low transmittance. The data of

Table 6.3: Shielding effectiveness and transparency of some commercial films.

Film	SE (dB)	T_{v} (%)
Century Solar Bronze 20	29.56	17.50
Century Nova 35	28.59	32.10
Century Nova 50	25.62	50.10
Century Solar Bronze 35	24.47	37.00
Century Solar Bronze 50	21.85	48.20
Argent 65	21.85	65
Century Nova 70	19.97	68.10
Optima Exterior 22	17.24	22.00
Stainless Steel Exterior 20	6.77	24.30
Century Signature 20	6.37	17.90
Century Signature 35	3.58	33.30
Endurance 38	2.8	38
Stainless Steel Exterior 35	2.60	33.90
Endurance 50	1.92	50

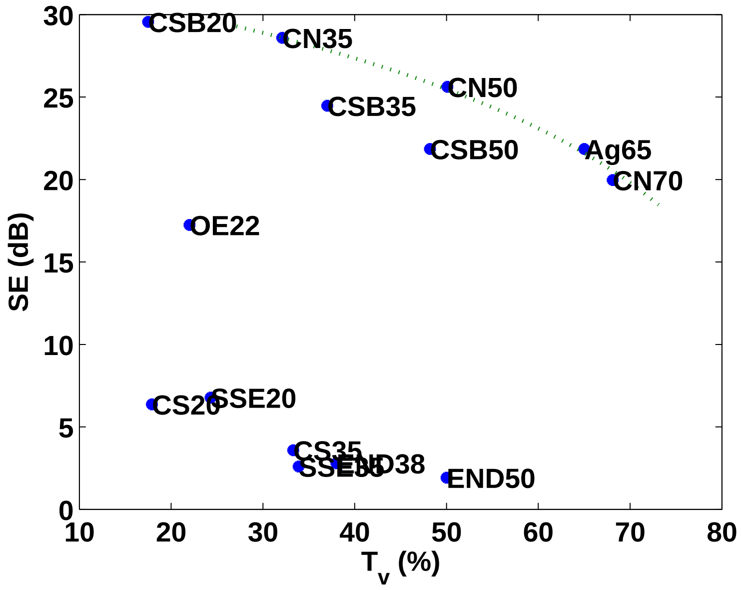

Figure 6.11: Diagram of the SE values and optical transparency of SUN-GARD films. The dotted curve depicts the SE expected from the experimental data for the Century Nova family.

Table 6.3 are also represented by the SE-T_v diagram in Fig. 6.13. This diagram permits to identify a correlation between the SE and the transparency by fitting the experimental data of the films belonging to the same family: an example is shown in Fig. 6.13 for the Century Nova family.

The SE was measured also using the nested RC technique with a hybrid mechanical-frequency stirring, as this technique will be included in the new Standard IEEE 299.1. The RC facility reproduces a realistic environment for shielding test of material. Moreover, the sample dimensions can be larger with respect the ones needed for waveguide structure. Fig. 6.12 shows the measured frequency spectrum between 1 GHz and 6 GHz of the film Argent 65. The obtained spectrum is compared with the measured one using the waveguide. The results are not identical as the two setups use different excitation incident fields, thus providing complementary information. In fact, the RC provides a sort of worst-case evaluation of the SE.

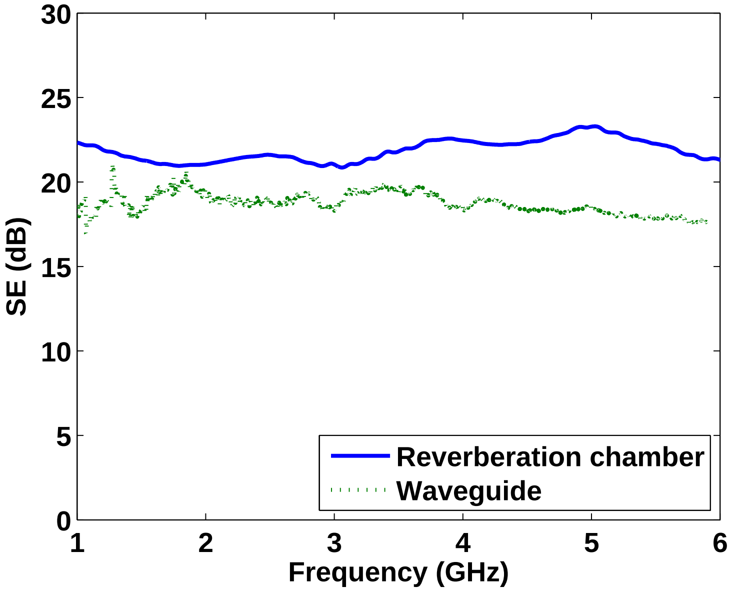

Figure 6.12: Frequency spectra of the film Argent 65 SE measured in the reverberation chamber and in the waveguide.

Finally, some preliminary results about the shielding performances provided in real conditions by a 120 × 80 cm window system consisting of a 4 cm size aluminium frame and a 6 mm thick glass covered by the film Century Nova 50 were obtained. The electric field attenuation was defined as the ratio between the field measured in an open-area tests site (OATS) by a probe placed behind the glass when the window is not present and the field measured inserting the window. Several system attenuations were observed by varying the characteristics and the distance of the transmitting antennas. The three frequency spectra represented in Fig. **??** were measured by using a horn antenna placed at 1.5 and 2.5 m from the window to ensure to operate in far-field conditions. For the first case both the horizontal and vertical antenna polarizations are showed. The strong frequency variability of the electric field attenuation is mainly due to the multi-path propagation produced by the non-ideal directivity of the used antennas and the reflecting ground plane.

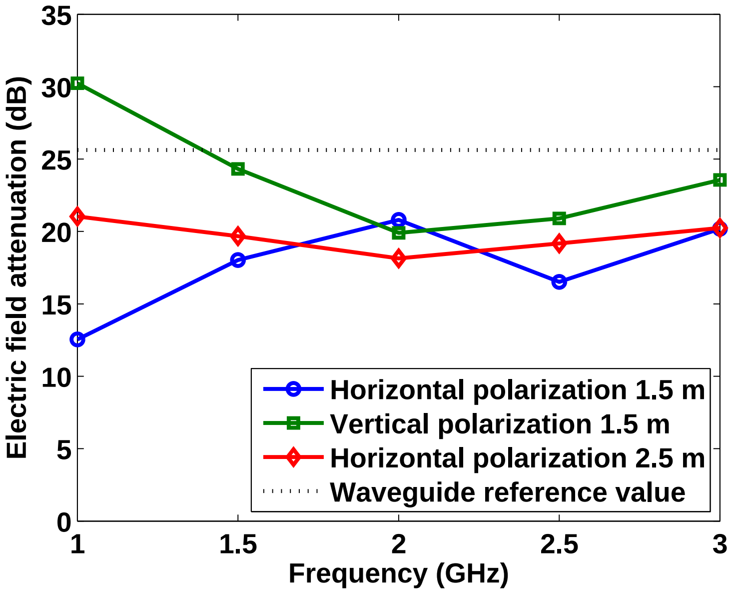

Figure 6.13: Frequency spectra of the measured electric field attenuation of a window system consisting of an aluminium frame and a 6 mm thickness glass covered by the film Century Nova 50.

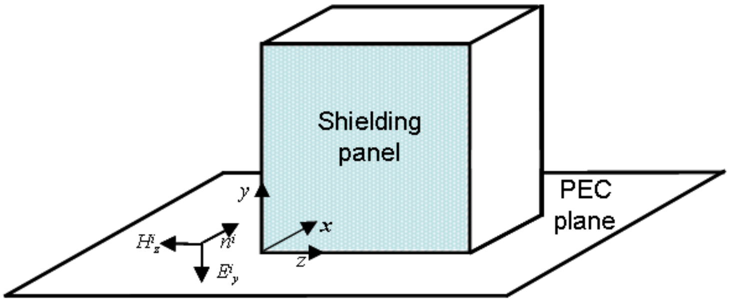

Figure 6.14: The excited box.

6.10 Shielding against EMP penetration

The EMP-interaction with an aluminum enclosure having a wall of carbon-fiber reinforced composite (CFRC) material was characterized by means of theoretical and experimental approaches: the simulated results were compared with measured data obtained by using a full-scale EMP generator [**?**]. The CFRC panel is replaced with two different types of transparent shields. The first shield consists of a commercial 175 μm-thick polycarbonate sheet, coated on one surface with an indium-titanium-oxide (ITO) film having thickness of 0.5 μm, and sheet resistance 13.35 S/□. The second screen is realized with a nanostructured transparent metallo-dielectric thin film applied on the panel surface. Titanium dioxide (TiO2) is used as target material for the dielectric layers in transparent metals; the conductive films are made of silver (Ag).

The thickness of the TiO2 films is 32 nm, of the Ag layers is 17 nm, of the Ti interlayers 1 nm. The total metal content is 68 nm. The overall thickness of the coating is 332 nm. The simulated configuration, shown in Fig. 6.14, considers a 3 mm-thick aluminum box of dimensions 70 cm $\times 70$ cm $\times 70$ cm. The incident electric field is simulated by a double exponential function with time constants $\tau_1 = 5$ ns, $\tau_2 = 200$ ns and $E_0 = 50$ kV/m. The numerical simulation is implemented by a three-dimensional finite-difference time domain (FDTD) procedure and the thin layer model described in [?] and [**?**], respectively. The electric and magnetic transient fields are recorded at positions (x=9.5 cm, y=34 cm, z=17.5 cm) and (x=2.5 cm, y=53.5 cm, z=27.8 cm), respectively. Figure 6.15 and 6.16

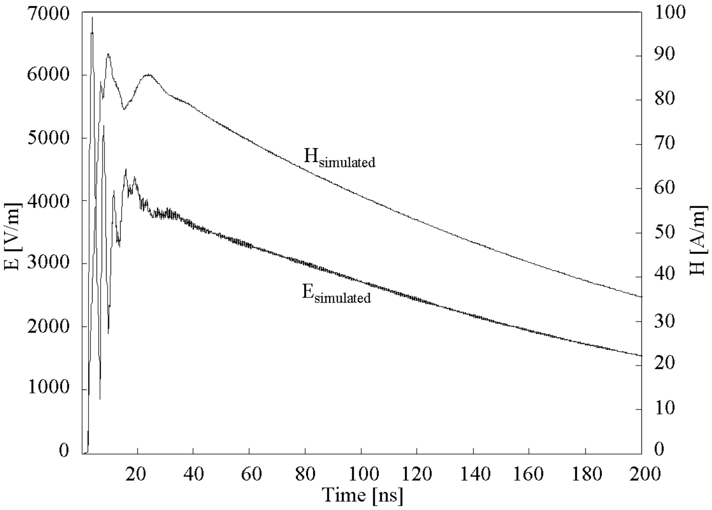

Figure 6.15: Transient electric field in the enclosure without the ITO- or Ag-shield.

represent the obtained transient waveforms inside the enclosure without and with the Ag- and the ITO- panel, respectively.

6.11 Nanostructured transparent shield against EMP interaction

The transient shielding performances of a nanostructured transparent shield installed on the aperture of a metal enclosure excited by an EMP-plane wave are analyzed. The screen consists of 17 alternating thin layers of metal (Ag) and dielectric (TiO2) materials. The 3D-FDTD simulation tool implementing the sub-cell model of the thin multilayered shield allows predicting the spatial distribution of the transient electric and magnetic fields inside the enclosure. The electromagnetic energy coupled with the unshielded and shielded box is obtained from the time integration of the transient power, which is computed as the flux of the Poynting vector through the aperture.

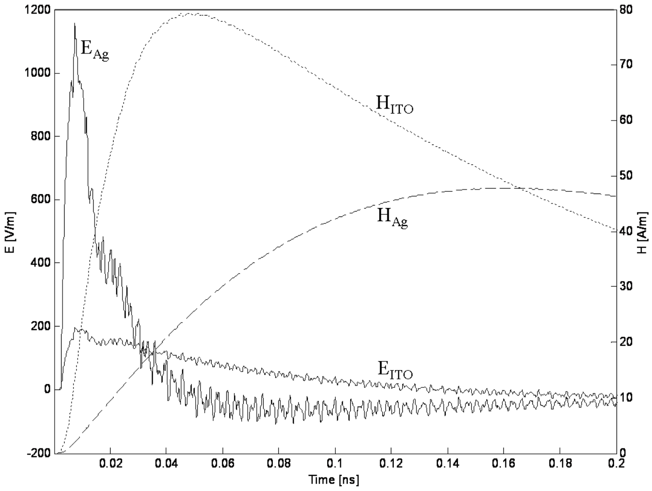

Figure 6.16: Transient magnetic field in the enclosure with the ITO- or Ag-shield.

6.11.1 Introduction

Nanostructured transparent metals providing high electromagnetic shielding at radio frequency and high transmittance in the visible range have been developed [**?**]-[**?**]. Experimental tests have demonstrated that planar samples of the new material, containing 68 nm in thickness of silver, are characterized by shielding effectiveness of 40 dB from 30 MHz to 6 GHz and optical transmittance in the visible range of 70 %. The feasibility of frequency selective surfaces made of transparent metal patches, with pass-band at 0.9 GHz and at 1.8 GHz was investigated in [?]. Moreover, the design of new nanolayered transparent thin films for active shielding of low frequency magnetic field was proposed in [**?**]. The transient electromagnetic shielding of an enclosure with apertures is a critical subject that has been widely investigated in analytical and/or experimental studies [**?**]- [**?**]: the obtained results are strongly dependent on the characteristics of the enclosure and cannot be considered of general validity. Moreover, the transient shielding effectiveness is not yet strictly defined inside the scientific community. The scope of this paper is to predict the transient shielding performances of a nanostructured transparent shield installed on the aperture of a metallic box excited by an EMP-

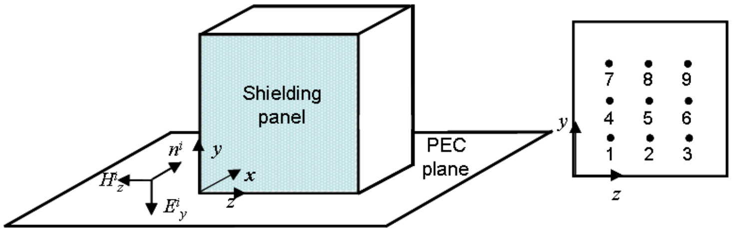

Figure 6.17: Excited box (a) and yz-plane at distance x inside (b).

plane wave. The analysis is carried out by means numerical simulations, which are performed by applying the three-dimensional finite-difference time domain (3D-FDTD) procedure described in [?] and the sub-cell model of thin multi-layer coatings developed in [**?**]. The transient waveforms of the electric and magnetic fields inside the enclosure with the unshielded and the shielded aperture are computed: the corresponding transmitted energies inside the enclosure are obtained from the discrete time integration of the transient power, which is computed as the flux of the Poynting vector through the aperture.

6.11.2 Configuration of the excited shielded aperture

The test configuration is constituted by a metallic enclosure having a shielded aperture. The 3 mm-thick aluminum box of dimensions 70 cm $\times 70$ cm $\times 70$ cm is illuminated by an EMP plane wave propagating along the x-axis with y-polarization, according to Fig. 6.17(a,b). The screen is realized by a 125-μm-thick polycarbonate panel coated with a nanostructured transparent metallo-dielectric thin film.

Transparent metals are one-dimensional (1D) photonic band gap (PBG) structures made by alternating layers of conducting (e.g. metal) and non-conducting (e.g. dielectric or semiconductor) materials [**?**]. The Titanium dioxide (TiO2) is used as target material for the dielectric layers in the transparent metals, due to its high refractive index and low absorption in the visible range. The conducting films are made of silver (Ag) due to the location of its plasma resonance, and have thickness greater than the limit value of 10 nm, below which the conductive properties of Ag are strongly reduced, due to the formation of islands. A critical issue in Ag/TiO2 multi-layer coatings realized by conventional radio frequency sputtering technique is the silver oxidation and agglomeration, due to the oxygen diffusion favoured by the heat and ions bombardment from the plasma [?]. The use of blocking layers, made of Titanium (Ti), is necessary in that case. The structure of the resulting coating, which is constituted by 17 layers, is (TiO2/Ti/Ag/Ti/TiO2)4 [?]. The thickness of the TiO2 films is 32 nm, of the Ag layers is 17 nm, and of the Ti interlayers 1 nm. The total metal thickness is $\delta_{Ag} = 68$ nm. The overall thickness of the coating is 332 nm. The electrical conductivity of the silver film, measured by using the four probes method on a sample of 17 nm in thickness, is equal to 7.75.106 S/m. The measured optical transmittance reaches the value of 70 % for normal incidence; a dielectric optical filter can be applied on the plain transparent substrate of the screened window in order to produce the same chromatic resolution and luminosity of the transparent metal [?].

6.11.3 Simulation model

The simulation tool of the excited enclosure with shielded aperture is based on the 3D-FDTD method [?] and on the efficient sub-cell model of the thin multi-layered shield [?]. The aluminum walls and the ground plane are considered as perfect-electric conducting. The FDTD analysis is carried out using space and time steps equal to 2 cm and 33 ps, respectively. UPML-boundary conditions are positioned at six cells from the discrete model of the box. The incident field of the EMP plane wave assumes the following expression:

$$E_y^i(t) = E_0 \left(e^{-t/\tau_2} - e^{-t/\tau_1} \right) \tag{6.44}$$

with time constants $\tau_1 = 5$ ns and $\tau_2 = 200$ ns, and $E_0 = 50$ kV/m. The inner transient electric and magnetic fields are computed in the yz-planes at different distances from the aperture along the x-axis. Note that the coupling effects inside the enclosure are principally due to the peak of the electric field and to the rise time of the magnetic field. The transient power $P(t)$ transmitted inside the unshielded and the shielded enclosure is computed as the flux of the Poynting vector $N(t)$

through the inner yz-plane located at the distance $x = 2$ cm from the aperture, i.e. at one cell from it. It results that $P(t)$ depends only on the following x-component $N_x(t)$ of the Poynting vector:

$$N_x(t) = E_y(t)H_z(t) - E_z(t)H_y(t) \tag{6.45}$$

in which $E_y(t)$, $H_z(t)$ are the dominant components associated to the incident EM field and $E_z(t)$, $H_y(t)$ are the ones generated by the interaction of the EM impinging field with the shielding enclosure. The transient energy W transmitted into the box is obtained by discrete time integration of the transient power $P(t)$.

6.11.4 Numerical prediction of the shielding performances

The electric and magnetic fields are computed in the nine positions shown in Fig. 6.17(b), which lay in the yz-plane at the distances of 2 cm (plane 1), 35 cm (plane 2) and 52.5 cm (plane 3) along the x-axis from the front panel. Figures **??**(a), **??**(b), **??**(c) and **??**(d) show the obtained field waveforms: notice that the highest Ey-peak value and the longest Hz-rise time are observed in point no. 2 of Fig. 6.17(b) in all considered planes, for both the shielded $\delta_{Ag} = 68$ nm) and the unshielded aperture. Next, the total silver thickness δ_{Ag} of the nanostructured shield is supposed equal to 34 nm and 136 nm. The computed transient fields at point no. 2 of plane 1 are reported in Figures **??**(a),(b).

Table 6.4 shows the values of the E_y-peak E_{yp}^{sh} and of the H_z-rise time t_{rH}^{sh} (from 0.1 to 0.9 of the peak value) for the shielded box configuration, and their ratio with respect to the corresponding values $E_{yp}^{un} = 10.6$ kV/m and $t_{rH}^{un} = 4$ ns computed for the unshielded box.

The procedure for the computation of the energy transmitted into the box is then applied. The flux of the Poynting vector is computed over the 70 cm $\times 70$ cm planar surface located on the yz-plane 1 at 2 cm from the aperture. The computed E_y and H_z components in each cell are utilized to obtain the total power transmitted inside the enclosure. Figures **??**(a) and (b) show the transient waveforms of the power for the shielded (δ_{Ag} equal to 34 nm, 68 nm and 136 nm) and unshielded aperture configuration.

Table 6.4: E-peak values and H-rise times.

δ_{Ag} (nm)	E_{yp}^{sh} (V/m)	E_{yp}^{un}/E_{yp}^{sh}	t_{rH}^{sh} (ns)	t_{rH}^{un}/t_{rH}^{sh}
34	547	19.4	60	0.07
68	282	37.6	93	0.04
136	143	74.1	106	0.03

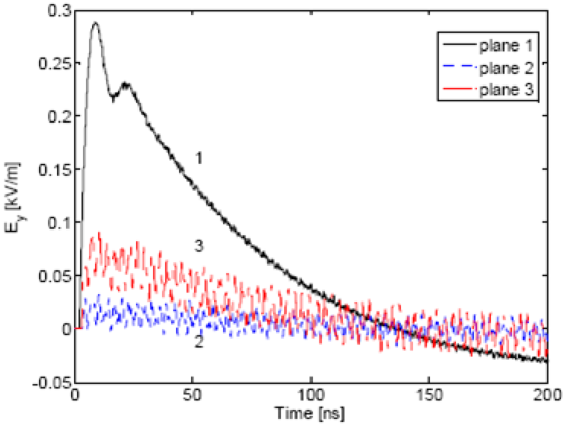

Figure 6.18: Transient waveforms of the electric field at point no. 2 of planes 1, 2, 3 for shielded ($\delta_{Ag=68}$ nm) aperture.

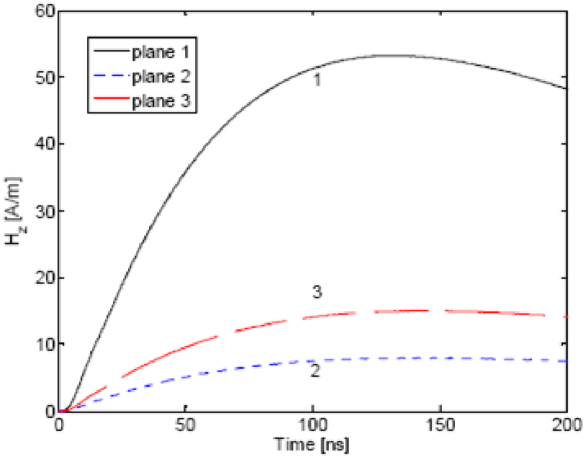

Figure 6.19: Transient waveforms of the magnetic field at point no. 2 of planes 1, 2, 3 for shielded ($\delta_{Ag=68}$ nm) aperture.

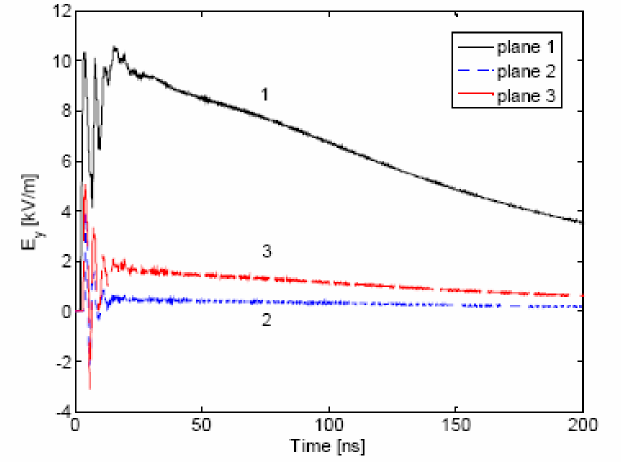

Figure 6.20: Transient waveforms of the electric field at point no. 2 of planes 1, 2, 3 for unshielded aperture.

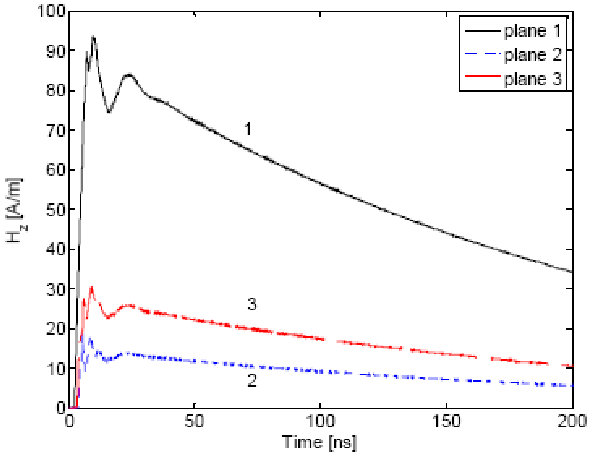

Figure 6.21: Transient waveforms of the magnetic field at point no. 2 of planes 1, 2, 3 unshielded aperture.

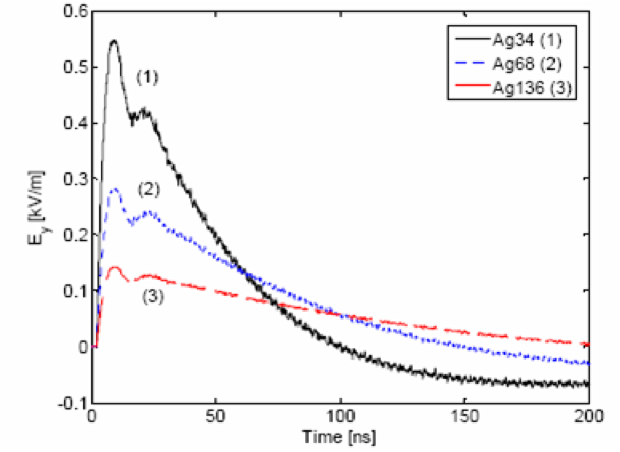

Figure 6.22: Transient waveforms of the electric field at point no.2 of plane 1 for different silver thicknesses.

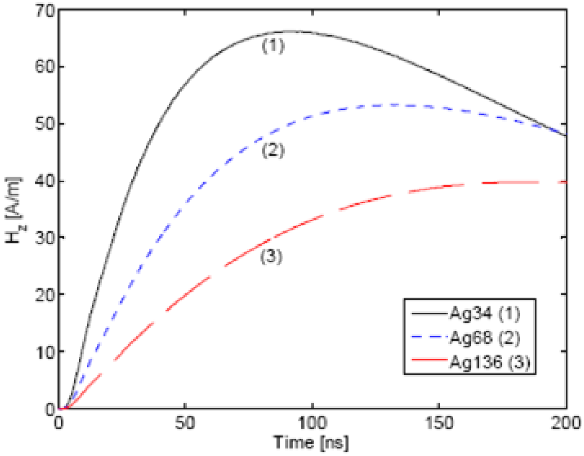

Figure 6.23: Transient waveforms of the magnetic field at point no.2 of plane 1 for different silver thicknesses.

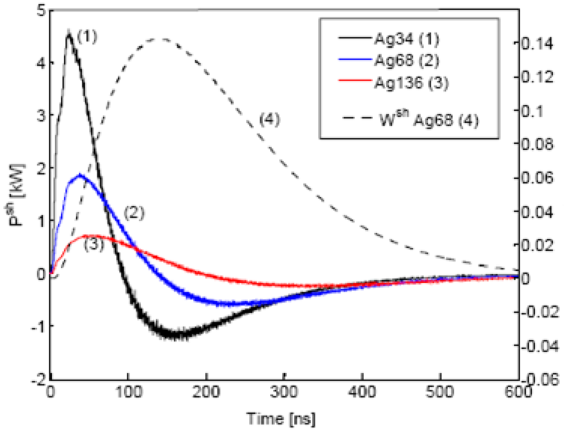

Figure 6.24: Transient waveforms of the transmitted power and energy through the yz-plane 1 at 2 cm inside the shielded box.

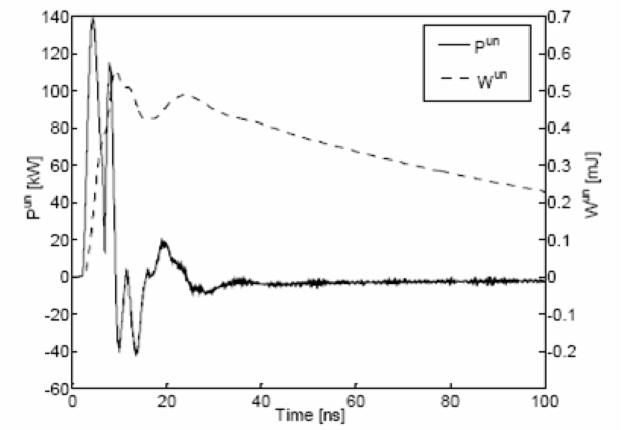

Figure 6.25: Transient waveforms of the transmitted power and energy through the yz-plane 1 at 2 cm inside the unshielded box.

Table 6.5: W-peak values and W-fall times for the shielded aperture.

δ_{Ag} (nm)	W_p^{sh} (mJ)	W_p^{un}/W_p^{sh}	t_{fW}^{sh} (ns)	t_{fW}^{un}/t_{fW}^{sh}
34	0.22	2.5	257	0.93
68	0.14	3.9	302	0.79
136	0.08	6.9	394	0.61

The energy is computed by means of the central difference time integration of the transient power, which is sampled up to 660 ns with a time step of 33 ps. The obtained waveforms for the shielded ($\delta_{Ag=68}$ nm) and unshielded enclosure are represented in Figures 6.24, 6.25 respectively. The peak value of the energy for the unshielded box is $W_p^{un} = 0.55$ mJ, and the fall time t_{fW}^{un} (intended as 0.9 to 0.1 of the peak value) is 240 ns. The values of W_p^{sh} and t_{fW}^{sh} for the shielded box are reported in Table 6.5.

6.11.5 Considerations on shields against EMP interaction

A procedure for the prediction of the transient shielding performances of enclosures with aperture against an EMP-plane wave is presented. The described 3D-FDTD numerical procedure allows the simulation of a nanostructured transparent metallo-dielectric thin film. The obtained results outline that the Ey-peak value decreases, the Hz-rise time increases and the W-peak value decreases as the overall silver thickness δ_{Ag} of the metallo-dielectric transparent metal increases. At the contrary, the optical performance of the shield improves as the total metal content decreases: it should be noted that for normal incidence the optical transmittance of the nanostructured shield in the visible range reaches the 70% for $\delta_{Ag} = 68$ nm and overcomes the 75%-80% in case of $\delta_{Ag} = 34$ nm, whereas for $\delta_{Ag} = 136$ nm the shield is no more transparent. The future development of this research will be focused on the EMP-shielding of active enclosures with aperture having electromagnetic sources inside.

6.12 EM characterization of shielding textiles

Shielding solutions available in the form of metal fibers and metal fibers fabrics are viable from a cost and production standpoint. Most metal fibers are really extremely fine wires produced by a bundle drawing process. A drawn wire of 50 microns diameter or less is defined as a fiber. Most metal fiber sales occur in the 4 to 25 micron diameter range. Metal fibers are generally available in fiber diameters of 2 to 50 microns, utilizing metals and alloys, for example: Stainless Steel, Nickel, Tin, Nickel Chromium, Titanium.

Where higher levels of attenuation are required, stainless steel non-woven fabric constructions are available in a variety of alloys, fabric weights and constructions. These non-wovens, shown in Fig. 6.26 are particularly effective for production of conductive composites since they are easily incorporated into composite structures with little additional labor or equipment investment. Other fiber forms may be utilized to produce necessary auxiliary products such as conductive adhesives, sealants, gaskets and coatings. Low galvanic action alloys may be used where this type of corrosion is a problem.

Non-woven Metallic Fabrics are highly versatile combinations of conductive and textile fiber, or all conductive fiber structures produced by a specialized manufacturing method. The metallization treatment on non-woven fabric supports offers the possibility to make polyester or polyamide filaments and micro-fiber textile structures electrically conductive. These fibers are covered with an electrochemical process, leaving the non-woven fabric with an electrical conductivity. They are produced on highly modified textile-type equipment which is capable of processing conductive fibers, or blends, of conductive fibers and synthetic or natural fibers into non-woven web fabric structures. Non-woven Conductive Fabrics are characterized by highly randomized, non-oriented fiber arrangements which are normally metallic in nature. The metallic fibers comprising the fabric can vary in diameter and alloy. The fiber content can even be blends of different alloys and diameters. Fabric weights can also be varied with the lightest weight product being one ounce per square yard. There are few limitations on producing heavier weight fabrics. Densities or porosities can be customized depending upon the

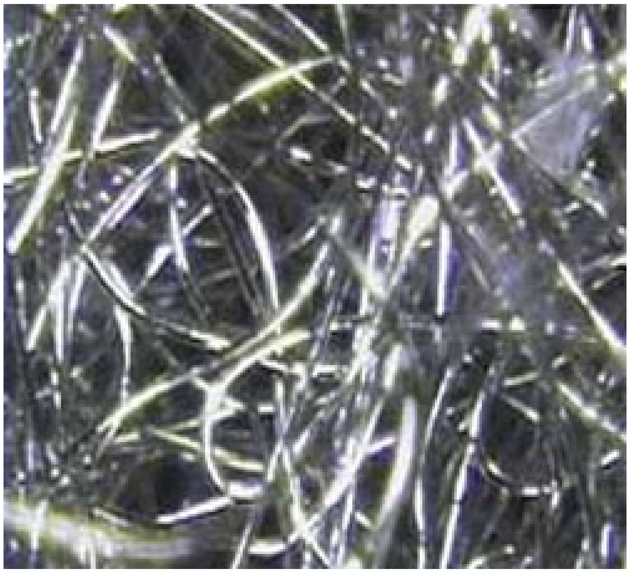

Figure 6.26: Non-woven fabric.

degree of consolidation and the fiber diameter utilized. Physical appearance can range from paper-like to that of a loose fiber batting-type structure. Non-woven Metal Fabrics may be stabilized through sintering, polymer bonding, or in the case of the finer fiber diameters, through consolidation with fiber to fiber friction.

Continuous multifilament metal fiber yarn, shown in Fig. 6.27 represent another approach to shielding problems. These products which are available in a selection of alloys can be woven or knitted with filament or spun reenforcing yarns into suitable configurations or they may be filament wound in combination with glass or other filament winding yarns to produce conductive filament wound parts. When woven in a matrix with carbon fiber tow, a fabric with good shielding as well as lightning strike properties can be produced. Performance of the fabric can be adjusted by varying the arrangement of the conductive yarns in the matrix.

Short aspect broken fibers are a relatively new development designed for use in applications where other fiber forms are not appropriate. The physical form of the product resembles a free flowing powder. Close examination, however, discloses that the particles are really individual fibers with aspect ratio specific

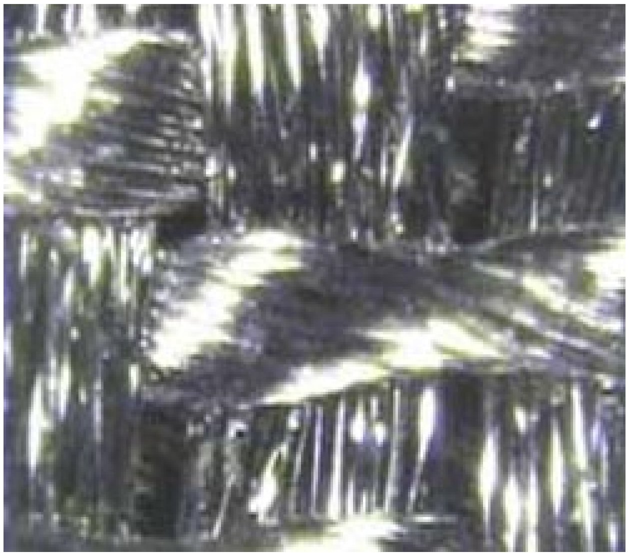

Figure 6.27: Multifilament metal fiber yarn.

to the respective fiber diameter. The absence of sizing agents and bent ends as well as the inherent free-flowing properties combine to make this product easily compounded into resins, elastomers, and powdered metals. Since the fiber is not in the form of a sized, chopped bundle, simple stirring procedures provide adequate dispersion. Broken fibers were specifically designed as the conductive element in the production of conductive gaskets, sealants, adhesives, and coatings. As such they represent a new and effective alternative to existing materials.

6.12.1 Measurements of SE with the nested RC hybrid technique

Comparative measurements of four different commercial shielding textiles, including non-woven and multifilament fiber yarns are carried out with the nested reverberation chamber hybrid approach proposed in Chapter 5. Table 6.6, summarizes some characteristics of the tested fabrics extracted from the commercial data sheets. Each textile is identified by a number from 1 to 4. The results of the measured shielding effectiveness of each fabric are shown in figures 6.28-6.31.

It can be observed that the measurement of the shielding effectiveness ob-

Table 6.6: Data of commercial textiles.

Textile #	Type	Weight [g/m^2]	Metallization [g/m^2]	Shielding [dB] at 200 MHz - 18 GHz
1	Polyester	96	35 Ni	50-40
2	Polyester	60	35 Ni	50-40
3	Non woven Polyester 1.5 mm	150	35-40 Ni	55-70
4	Non-woven Polyamide	31	30 Cu 2/3 Sn	80-70

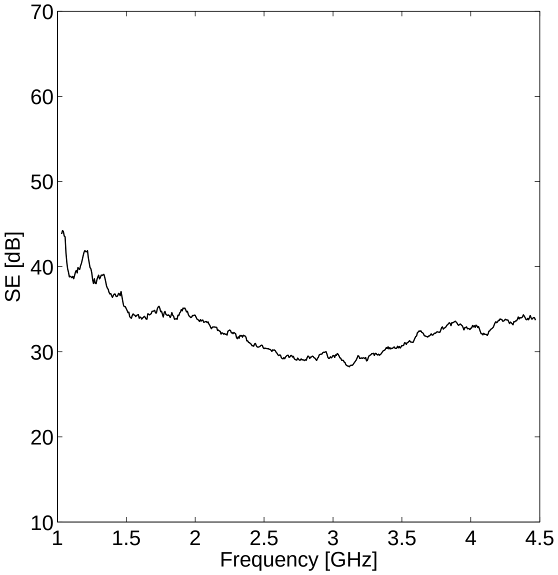

Figure 6.28: Textile $\#1$:SE frequency spectrum, in the 1 GHz - 4.5 GHz frequency range, measured with the hybrid approach for $\Delta f = 100$ MHz.

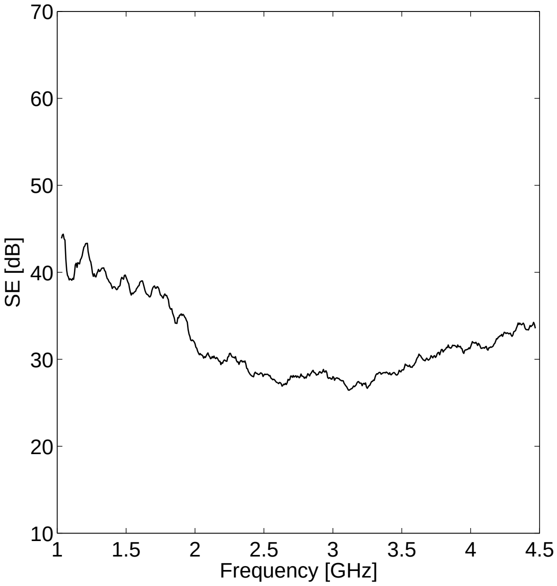

Figure 6.29: Textile $\#2$:SE frequency spectrum, in the 1 GHz - 4.5 GHz frequency range, measured with the hybrid approach for $\Delta f = 100$ MHz.

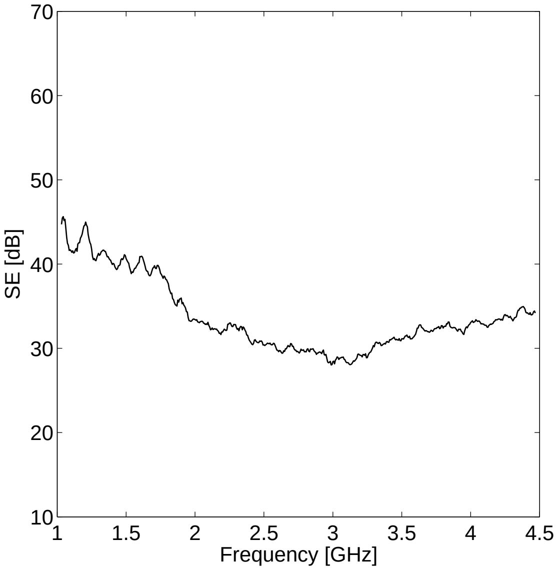

Figure 6.30: Textile $\#3$:SE frequency spectrum, in the 1 GHz - 4.5 GHz frequency range, measured with the hybrid approach for $\Delta f = 100$ MHz.

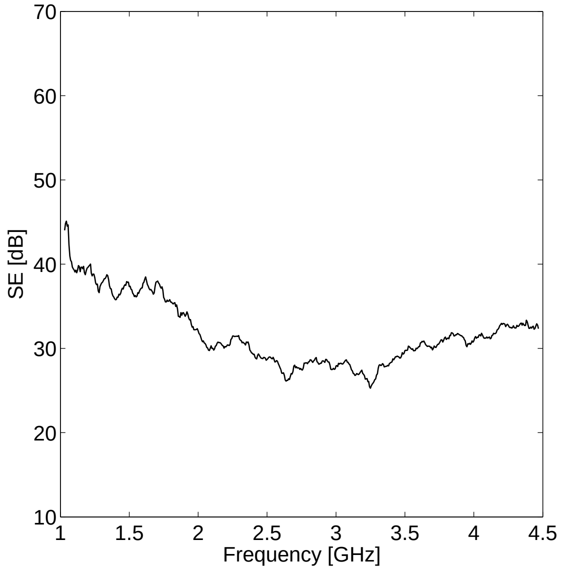

Figure 6.31: Textile $\#4$:SE frequency spectrum, in the 1 GHz - 4.5 GHz frequency range, measured with the hybrid approach for $\Delta f = 100$ MHz.

tained with the nested RC hybrid approach are not always consistent with the values presented in the commercial data sheets, obtained according to the standard SE MIL-STD-285, now included in the more recent [43]. The latter method is based on a plane wave approach, that can overestimate the actual shielding of the material, while the RC technique is more adequate to account for a more realistic electromagnetic environment. Moreover, all the curves present a minimum due to the resonant effect of the aperture of the box, that shifts in frequency depending on the size of the aperture itself. For our aperture, the minimum corresponds to a frequency of about 3 GHz, as expected.

Chapter 7

Radar Absorbing Materials

The Chapter describes an equivalent circuit approach for the analysis and the electromagnetic design of innovative thin absorbers. The use of thin bilayers of metamaterials as spacer in dielectric Salisbury screen is discussed. It is demonstrated that narrow-band thin absorbers can be obtained using both positive and negative materials, whereas broad-band thin absorbing screen can be realized only with bilayer of epsilon-negative and mu-negative materials. An optimization tool based on genetic algorithms is developed in order to design electrically thin absorbing screens including metamaterials for electromagnetic interference suppression. The optimization procedure is fully detailed and some design solutions of subwavelength screens are proposed.

7.1 Introduction

The increasing complexity of electronic devices and equipment and the widespreading use of wireless communication systems have pushed towards the development of multifunctional materials for electromagnetic interference (EMI) suppression, like shielding/absorbing materials. As regards aerospace systems, the key-requirements to be considered in the design of new materials for EMI protection are minimum weight and minimum volume. In general critical aspects in the design of absorbing laminated panel for radio frequency (RF) electromagnetic (EM) fields concern the minimization of the overall thickness of the screen and the maximization of the band-width of the absorber in the frequency range of interest. For instance the quarter-wavelength resonance that characterizes the dielectric Salisbury screen (SS) represents a limitation in the overall thickness of the shield [50], [51]. The use of metamaterials has been widely investigated in order to realize new devices for EM applications, like resonant cavities and sub-wavelength resonators [52]- [53]. It was shown that, by theory, the field enhancement taking place at the interface of a pair of metamaterial slabs, made for instance of left-handed materials, can be exploited to shrink the overall dimensions of field resonant devices [54]- [55]. However, one main limitation of existing studies on the use of metamaterials for the practical realization of EM devices is the lack of guidelines and indications for the practical design of both the device and the metamaterial layers. This paper focuses on the development of new thin absorbers. In general, the attribute “thin” can be intended as: “thin” in relation to the technology of application and creation of layers; “thin” in relation to the wavelength in each layer of the multilayer absorber. According to the second definition of “thin” above, sub-wavelength field-enhanced absorbing panels are analyzed in this work. The scope of this paper is to propose a methodological approach to define the design constraints of new thin laminated absorbers, constituted by pair(s) of metafilm. A metafilm is intended as a film made of metamaterial. This paper investigates metafilm characterized by isotropic EM properties on the plane of the film. A metafilm can be classified, according to the classification of metamaterial, depending on the values that the real parts of the dielectric permittivity and magnetic permeability in the plane of the film assume in the frequency range of interest. Double Positive Material (DPM) has the real parts of both the electrical permittivity and magnetic permeability positive. Double Negative Material (DNM) has the real parts of both the electrical permittivity and magnetic permeability negative. Epsilon-Negative Material (ENM) or Mu-Negative Material (MNM) has only negative real part of the electrical permittivity or of the magnetic permeability, respectively. Starting from the behavior of a traditional SS, this paper investigates the use of metafilm bilayers in order to realize screens having

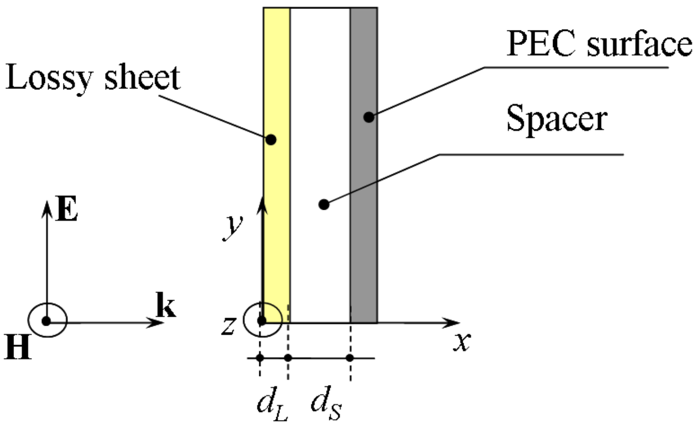

Figure 7.1: Schematic configuration of the dielectric Salisbury screen.

sub-wavelength thickness. An innovative methodological approach in modeling and designing the thin screen structure is proposed. The analysis starts from the EM propagation equations. The resonant frequency of the structure is derived from the input impedance of the equivalent circuit model of the multilayer structure. The EM performances and total thickness of thin absorbers realized by bi-layers of metafilms with different characteristics (e.g. DPM/DPM, DNM/DNM, ENM/MNM, MNM/ENM) are analyzed and compared in order to ascertain the practical advantages in the use of metamaterials instead of traditional materials.

7.2 Thin absorbing screen including metafilms

7.2.1 The Salisbury screen

Figure 7.1 shows the basic configuration of a SS. The first layer is the highly conductive surface to be screened. In general, it is assumed that such surface is perfect electric conducting (PEC).

The second layer is generally made of lossless dielectric. The third layer is the lossy sheet, which has the function of absorbing the EM energy associated to the incident field. Let's assume that the screen, having infinite dimensions along the y- and z- axes, is illuminated by an incident TM plane wave with normal

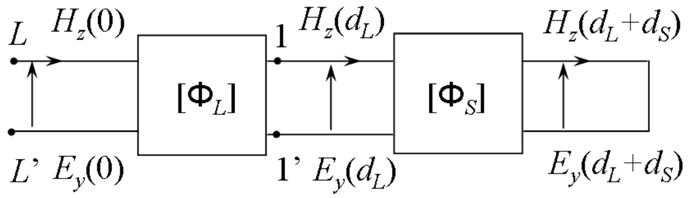

Figure 7.2: Equivalent TL model of the dielectric Salisbury screen of fig 7.2.

incidence. The EM wave propagation equations through the slab are described by the following expressions:

$$\begin{bmatrix} E_y(0) \\ H_z(0) \end{bmatrix} = \begin{bmatrix} \Phi_L(2,2) & -\Phi_L(1,2) \\ -\Phi_L(2,1) & \Phi_L(1,1) \end{bmatrix} \begin{bmatrix} E_y(d_l) \\ H_z(d_l) \end{bmatrix} \tag{7.1}$$

$$\begin{bmatrix} E_y(d_l) \\ H_z(d_l) \end{bmatrix} = \begin{bmatrix} \Phi_S(2,2) & -\Phi_S(1,2) \\ -\Phi_S(2,1) & \Phi_S(1,1) \end{bmatrix} \begin{bmatrix} E_y(d_L+d_S) \\ H_z(d_L+d_S) \end{bmatrix} \tag{7.2}$$

in which the coefficients of the transmission matrix are:

$$\Phi_{L(S)}(1,1) = \Phi_{L(S)}(2,2) = \cosh(\gamma_{L(S)} d_{L(S)}) \tag{7.3}$$

$$\Phi_{L(S)}(1,2) = -\eta_{L(S)} \sinh(\gamma_{L(S)} d_{L(S)}) \tag{7.4}$$

$$\Phi_{L(S)}(2,1) = -\eta_{L(S)}^{-1} \sinh(\gamma_{L(S)} d_{L(S)}) \tag{7.5}$$

The propagation constant $\gamma_{L(S)}$ and the intrinsic impedance $\eta_{L(S)}$ of the lossy sheet (spacer) are expressed as function of the electrical parameters of the material realizing the layer:

$$\gamma_{L(S)} = j\omega\sqrt{\mu_{L(S)}\varepsilon_{L(S)}} \tag{7.6}$$

$$\eta_{L(S)} = j\omega\sqrt{\frac{\mu_{L(S)}}{\varepsilon_{L(S)}}} \tag{7.7}$$

In general, for standard SS it is set $\mu_L = \mu_0, \varepsilon_L = \varepsilon_0\varepsilon_{rL} + \sigma_L/j\omega, \mu_S = 0, \varepsilon_S = \varepsilon_0\varepsilon_{rS}$. The boundary conditions describing the impinging EM wave at $x = 0$ and the PEC surface at $x = d_S + d_L$ read:

$$E_y(0) = 2E^i - \eta_0 H_z(0) \tag{7.8}$$

$$E_y(d_L + d_S) = 0 \tag{7.9}$$

The equivalent transmission line (TL) circuit of the SS is sketched in Fig. 7.2. The condition of maximum EM field absorption is satisfied when the equivalent input impedance at the section $(1 - 1')$ of the circuit of Fig. 7.2 is infinite, and the resulting input impedance of the slab at the section (LL')

$$Z_{(LL')} = \frac{\eta_L}{\tanh(\gamma_L d_L)} \tag{7.10}$$

matches the free space impedance η_0:

$$\Re\left\{Z_{(LL')}\right\} = \eta_0 \tag{7.11}$$

$$\Im\left\{Z_{(LL')}\right\} = 0 \tag{7.12}$$

The minimum reflection coefficient of the screen is then obtained at the first resonance frequency f_{res1}, i.e. when the thickness d_S of the spacer satisfies the condition:

$$d_S = \frac{\lambda}{4} = \frac{C_0}{4 f_{res1}\sqrt{\varepsilon_{rS}}} \tag{7.13}$$

Moreover, if the lossy sheet is thin and $\varepsilon_{rL} \ll \sigma_L/\omega\varepsilon_0$, eqs. 7.11, 7.12 are fulfilled when:

$$\sigma_L d_L = 1/\eta_0 \tag{7.14}$$

It results that the traditional SS behaves as a narrow-band absorber because the minimum EM field reflection takes place only at the frequency f_{res1} defined in 7.13. Moreover the traditional SS cannot be electrically thin because the spacer thickness d_L is constrained by the $\lambda_L/4$ condition.

7.2.2 Sub-wavelength thin Salisbury screen

The SS described in the previous section is basically a $\lambda/4$-resonant structure. The maximum absorption of the electromagnetic energy associated to the incident field takes place at the interface between the spacer and the lossy-sheet, where the electric field is maximum due to the $\lambda/4$-resonance. Therefore, the $\lambda/4$-resonance

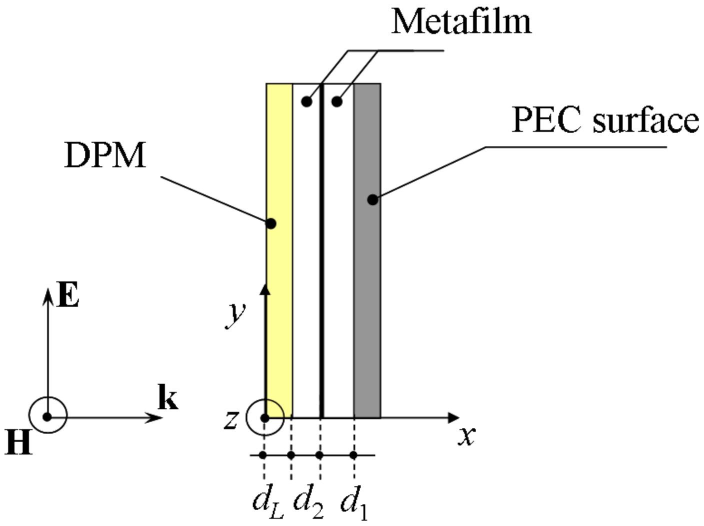

Figure 7.3: Schematic configuration of a TSS constituted by a metafilm bilayer and a lossy sheet, illuminated by a monochromatic plane wave with normal incidence.

phenomenon represents a limit on the overall thickness of the SS, which cannot be much smaller than the wavelength in the spacer and/or in the lossy sheet. A novel approach is described in the following, in order to realize an electrically thin Salisbury screen (TSS). The new SS has the four layers structure of Fig. 7.2. The back panel realizes the PEC surface of the screen. The lossy sheet is the same as the one of the SS of Fig. 7.1. The spacer of the SS is replaced by a bilayer made of a pair of metafilms. The typology of metafilm and the electrical parameters of each layer are defined so that the bilayer behaves as a thin sub-wavelength resonator. Several studies [54]- [53] have qualitatively shown that sub-wavelength resonances take place in bilayers made of DNM/DNM or ENM/MNM pairs. In the following, a rigorous analytical approach is developed in order to quantitatively investigate the existence of sub-wavelenght resonances in bilayer structures made of metafilm pairs.

7.2.3 Equivalent circuit model of a thin Salisbury screen

Let's consider the SS sketched in Fig. 7.2 The lossy sheet of thickness d_L has magnetic permeability μ_0, real relative permittivity $\varepsilon_{rL} > 0$ and real electrical conductivity $\sigma_L > 0$. The metafilms realizing the bilayer spacer are assumed to be lossless. The analysis of the structure is performed in the hypothesis that at the first resonance frequency of the TSS, f_{res1}, corresponding to the first minimum of the reflection coefficient, each metafilm layer is electrically thin. Therefore, the thicknesses d1 and d2 satisfy the condition:

$$d_i = \frac{k_S}{\omega_{res1}\sqrt{|\mu_i||\varepsilon_i|}} = 1,2 \tag{7.15}$$

in which $\omega_{res1} = 2\pi f_{res1}$ and $k_S \ll 1$ is a real positive constant. In the hypothesis 7.15 the thin metafilm can be modeled by an equivalent-lumped parameter circuit. Assume for instance that the $i-th$ metafilm layer is made of DNM. The EM field propagation equation through the layer having thickness d_i reads:

$$\begin{bmatrix} E_y(x) \\ H_z(x) \end{bmatrix} = \begin{bmatrix} \Phi_i(2,2) & -\Phi_i(1,2) \\ -\Phi_i(2,1) & \Phi_i(1,1) \end{bmatrix} \begin{bmatrix} E_y(x+d_i) \\ H_z(x+d_i) \end{bmatrix} \tag{7.16}$$

in which:

$$\Phi_i(1,1) = \Phi_i(2,2) = \cosh(\gamma_i d_i) \tag{7.17}$$

$$\Phi_i(1,2) = -\eta_i \sinh(\gamma_i d_i) \tag{7.18}$$

$$\Phi_i(2,1) = -\eta_i^{-1} \sinh(\gamma_i d_i) \tag{7.19}$$

and

$$\gamma_i = j\omega\sqrt{\mu_i \varepsilon_i} \tag{7.20}$$

$$\eta_i = j\omega\sqrt{\frac{\mu_i}{\varepsilon_i}} \tag{7.21}$$

In the thin-layer hypothesis 7.15, the $cosh-$ and $sinh-$ functions appearing in 7.17-7.19 can be approximated by the corresponding small-argument Taylor expansions truncated at the first term:

$$\widetilde{\Phi}_i(1,1) = \widetilde{\Phi}_i(2,2) = 1 \tag{7.22}$$

$$\widetilde{\Phi}_i(1,2) = -\eta_i\gamma_i d_i = j\omega|\mu_i|d_i \tag{7.23}$$

$$\widetilde{\Phi}_i(2,1) = -\frac{\gamma_i d_i}{eta_i} = j\omega|\varepsilon_i|d_i \tag{7.24}$$

The equation system 7.16 finally assumes the following approximated form:

$$E_y(x) = E_y(x+d_i) - j\omega|\mu_i|d_i H_z(x) \tag{7.25}$$

$$H_z(x) = -j\omega|\varepsilon_i|d_i E_y(x+d_i) + H_z(x+d_i) \tag{7.26}$$

which is obtained by setting $H_z(x+d_i) \cong H_z(x)$ in refportland14a. If the metafilm is made of metamaterial of different type, the propagation constant, the intrinsic impedance and the coefficients of the transmission matrix assume the expressions reported in Table 7.1.

The equivalent lumped-parameter circuits of bilayer-spacers loaded on PEC having different configurations are sketched in Table 7.2.

The condition for minimum reflection requires that the metafilm bilayer loaded on PEC is characterized by a high-impedance resonance at the frequency f_{res1}, and that the electrical conductivity and thickness of the lossy sheet satisfy condition 7.14. The equivalent circuits of the bilayer configurations reported in Table 7.2 are analyzed in order to define the resonance frequencies of the equivalent input impedance $Z_{(2-2')}$ at the section $(2-2')$.

It results that as regards configurations A and E, the first resonance corresponding to infinite input impedance (parallel resonance), occurs at the frequency

$$f_{res1} = \frac{1}{\sqrt{|\mu_1||\varepsilon_2|d_1 d_2}} \tag{7.27}$$

The structures B and D are characterized by a parallel resonance at the same frequency 7.27, but at lower frequency, i.e. for for $f < f_{res1}$, they are characterized by a series resonance corresponding to a zero of the equivalent input impedance. Finally, the bilayer C is characterized by a series resonance at the frequency 7.27. In conclusion, it results that the TSS can be made only by using as spacer one of the bilayer structures A, B, D, E in Table 7.2. In fact, at $f = f_{res1}$ for $Z_{(2-2')} = \infty$ equation 7.10 holds, and the minimum of the reflection coefficient of the screen is obtained if the matching condition 7.14 is satisfied. At the

Table 7.1: Propagation Constant, Intrinsic Impedance and Transmission Matrix Coefficients for Different Types of Metamaterials.

Material Type	γ	η	Coefficients of the Transmission Matrix
DPM $\mu = \lvert\mu\rvert$ $\varepsilon = \lvert\varepsilon\rvert$	$j\omega\sqrt{\mu\varepsilon}$	$\sqrt{\mu/\varepsilon}$	$\Phi(1,1) = \Phi(2,2) = \cosh(jd)$ $\Phi(1,2) = -\eta\sinh(jd)$ $\Phi(2,1) = -\eta^{-1}\sinh(jd)$
DNM $\mu = -\lvert\mu\rvert$ $\varepsilon = -\lvert\varepsilon\rvert$	$j\omega\sqrt{\lvert\mu\rvert\lvert\varepsilon\rvert}$	$\sqrt{\lvert\mu\rvert/\lvert\varepsilon\rvert}$	$\Phi(1,1) = \Phi(2,2) = \cosh(jd)$ $\Phi(1,2) = \eta\sinh(jd)$ $\Phi(2,1) = \eta^{-1}\sinh(jd)$
ENM $\mu = \lvert\mu\rvert$ $\varepsilon = -\lvert\varepsilon\rvert$	$j\omega\sqrt{\mu\lvert\varepsilon\rvert}$	$\sqrt{\mu/\lvert\varepsilon\rvert}$	$\Phi(1,1) = \Phi(2,2) = \cosh(jd)$ $\Phi(1,2) = -\eta\sinh(jd)$ $\Phi(2,1) = -\eta^{-1}\sinh(jd)$
MNM $\mu = -\lvert\mu\rvert$ $\varepsilon = \lvert\varepsilon\rvert$	$j\omega\sqrt{\lvert\mu\rvert\varepsilon}$	$\sqrt{\lvert\mu\rvert/\varepsilon}$	$\Phi(1,1) = \Phi(2,2) = \cosh(jd)$ $\Phi(1,2) = \eta\sinh(jd)$ $\Phi(2,1) = \eta^{-1}\sinh(jd)$

Table 7.2: Equivalent lumped-parameter circuit of bilayer spacers loaded on PEC.

Type	Bilayer-Spacer Configuration	Equivalent Circuit
A	DPM / DPM / PEC $\mu_2 > 0 \quad \mu_1 > 0$ $\varepsilon_2 > 0 \quad \varepsilon_1 > 0$	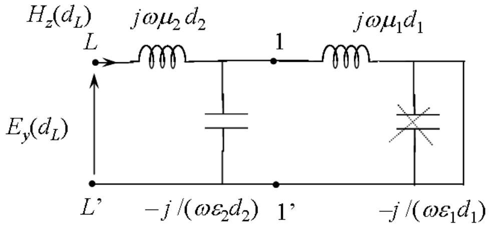
B	MNM / DPM / PEC $\mu_2 < 0 \quad \mu_1 > 0$ $\varepsilon_2 > 0 \quad \varepsilon_1 > 0$	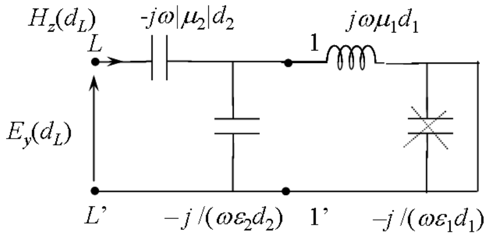
C	DPM / DNM / PEC $\mu_2 > 0 \quad \mu_1 < 0$ $\varepsilon_2 > 0 \quad \varepsilon_1 < 0$	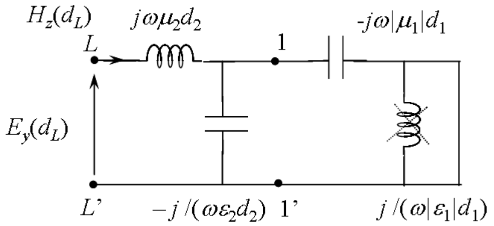
D	DNM / DNM / PEC $\mu_2 < 0 \quad \mu_1 < 0$ $\varepsilon_2 < 0 \quad \varepsilon_1 < 0$	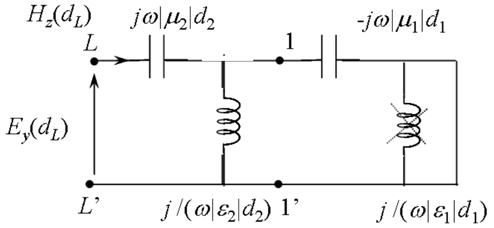
E	ENM / MNM / PEC $\mu_2 > 0 \quad \mu_1 < 0$ $\varepsilon_2 < 0 \quad \varepsilon_1 > 0$	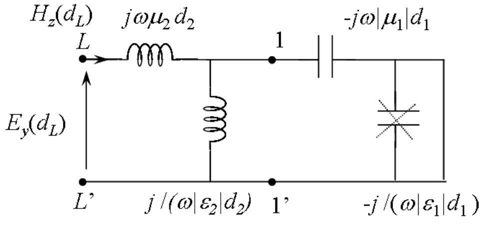

contrary, configuration C at the resonance frequency f_{res1} behaves as a PEC, thus producing maximum reflection. It is also observed that for frequencies higher than the first resonance frequency fres1, when the metafilms are no more electrically thin, the bilayer E in Table 7.2 is characterized by a second parallel resonance, because the EM field is evanescent and cannot propagate in the ENM and in the MNM. At the contrary, in the DPM/DPM/PEC structure at high frequency there appear both series and parallel resonances because of the EM field propagation. It results that a broad-band TSS can be realized only by using as spacer the metafilm bilayer of the type ENM/MNM.

7.2.4 Design Specification of Thin Salisbury Screen

The design specifications on the metafilms that constitute the TSS of Fig. 7.3 are defined with reference to one of the configurations A, B, D, E of Table 7.2, because they are all characterized by the parallel resonance at the frequency f_{res1}. Let's consider for instance the thin screen LS/DNM/DNM/PEC. In the thin-sheet hypothesis 7.15, at the resonance frequency f_{res1}, it results:

$$d_1 d_2 = \frac{k_S}{\omega_{res1}^2 \sqrt{|\mu_1||\varepsilon_1||\mu_2||\varepsilon_2|}} \tag{7.28}$$

Combining eqs. 7.28 and 7.27, it yields:

$$|\mu_1||\varepsilon_2| = \frac{\sqrt{|\mu_1||\varepsilon_1||\mu_2||\varepsilon_2|}}{k_S} \tag{7.29}$$

which is fulfilled if:

$$|\mu_1| = \frac{|\mu_2|}{k_S} \tag{7.30}$$

$$|\varepsilon_2| = \frac{|\varepsilon_1|}{k_S} \tag{7.31}$$

Expression 7.30 and 7.31 are the design specifications of the TSS having the bilayer-spacer constituted by a metafilm pair of type A, B, D, E of Table 7.2. If conditions 7.30, 7.31 are fulfilled the SS is electrically thin. The thicknesses d_1 and d_2 are defined uniquely and independently on the type of the metafilm bilayer. This means that it is possible to realize a narrow-band TSS of defined thickness

Table 7.3: Electrical and geometrical characteristics of a TSS including metafilm, having the configuration shown in fig. 7.3.

Metafilm 1	$d_1 = 290.4\mu$m	$\lvert\mu_{r1}\rvert = \lvert\mu_{r2}\rvert/k_S$	$\lvert\varepsilon_{r1}\rvert = 1$	$\sigma_1 = 0$
Metafilm 2	$d_2 = 290.4\mu$m	$\lvert\mu_{r2}\rvert = 10$	$\lvert\varepsilon_{r2}\rvert = \lvert\varepsilon_{r1}\rvert/k_S$	$\sigma_2 = 0$
Lossy sheet	$d_L = 442.0\mu$m	$\mu_{rL} = \mu_0$	$\varepsilon_{rL}\rvert = \varepsilon_0$	$\sigma_L = 6$ S/m

$d_{tot} = d_L + d_1 + d_2$ by using only DPMs. The use of metamaterials with negative parameters does not produce the reduction of the thickness of the spacer in case of narrow-band absorbers. At the contrary, a broad-band TSS with resonance frequency f_{res1} and $f_{res2} > f_{res1}$ can be made only by using the metafilm bilayer E in Table 7.2, having as a spacer the ENM/MNM pair.

7.2.5 Numerical calculations

Numerical calculations are performed in order to assess the proposed procedure for the design of narrow-band and broad-band TSSs. At first, the TSS having the characteristics reported in Table 7.3 and resonance frequency $f_{res1} = 2.6$ GHz is considered. The total thickness of the screen is $d_{tot} = 1.02$ mm, and it is set $k_S = 0.05$. Figure 7.4 shows the computed frequency spectra of the reflection coefficient in dB of the TSS assuming that the spacer is constituted by one of the different types of metafilm pairs A, B, D, E of Table 7.2.

The calculation is performed applying the exact model described by eq. 7.16, in which the coefficients of the transmission matrix are given by the expressions reported in Table 7.1. Notice that in the low-frequency range, where the metafilm layers are electrically thin, all curves are nearly overlapping. At frequencies higher than 5 GHz, the reflection coefficients of the TSS made with the bilayer DPM/DPM or DNM/DNM have a similar trend, and reach the maximum value of 0 dB. Next, the analysis is performed with reference to the TSS including the ENM/MNM pair, in order to verify for which values of the relative electrical permittivity of the lossy sheet it is possible to observe the broad-band response. Figure 7.5 shows the reflection coefficient of the screen computed by using the

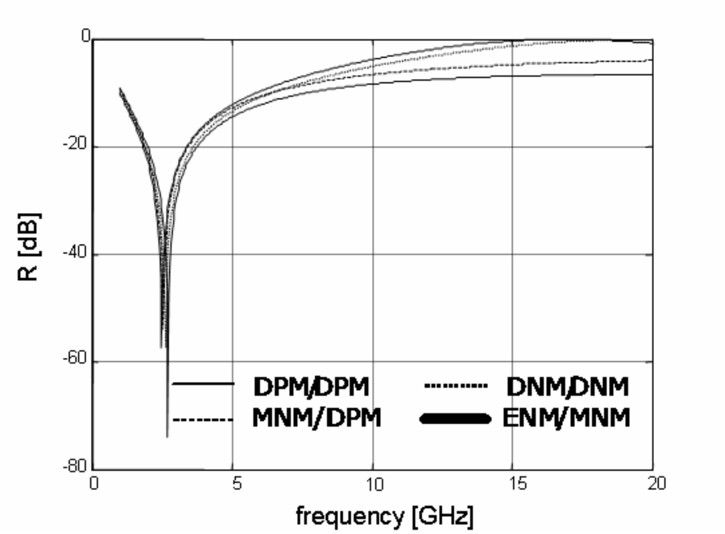

Figure 7.4: Frequency spectra of the reflection coefficient in dB of the TSS with spacer constituted by one of the different types of metafilm pairs A, B, D, E in Table 7.2.

data of Table 7.3, for increasing values of ε_{rL}. It is observed that as the relative permittivity of the lossy sheet increases, the second parallel resonance of the structure moves towards the low frequency range, producing the broad-band response of the absorber. The best wide-band performance is obtained for $\varepsilon_{rL} = 8$. The calculation is then repeated for $\varepsilon_{rL} = 8$ considering the TSS including one of the metafilm pairs A, B, D, E of Table 7.2. The obtained data are reported in Fig. 7.6. Notice that, as expected, the second relative minimum of the reflection coefficient is obtained only for the screen including the ENM/MNM bilayer. Finally, the sensitivity analysis against the value of the parameter k_S is performed, considering the broad-band TSS including the ENM/MNM bilayer and assuming $\varepsilon_{rL} = 8$. The curves reported in Fig. 7.7 show that the second resonance frequency moves towards the low frequency range as k_S increases because the metafilm layers become electrically thicker. In fact, for $k_S = 0.005$ it results $d_1 = d_2 = 29$ m and $d_{tot} = 500$ m; for $k_S = 0.05$ it results $d_1 = d_2 = 290$ m and $d_{tot} = 1023$ m; for $k_S = 0.1$ it results $d_1 = d_2 = 581$ m and $d_{tot} = 1600$ m.

Depending on the characteristics of the materials realizing the layers of the

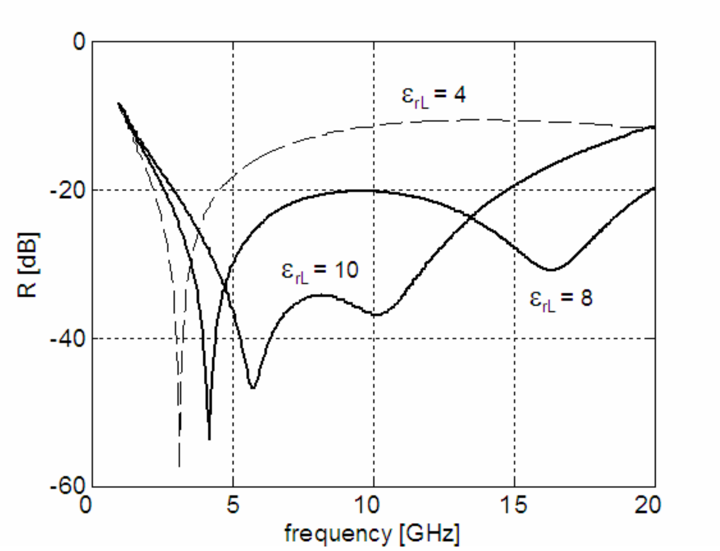

Figure 7.5: Reflection coefficient of the screen including the ENM/MNM bilayer for increasing values of ε_{rL}.

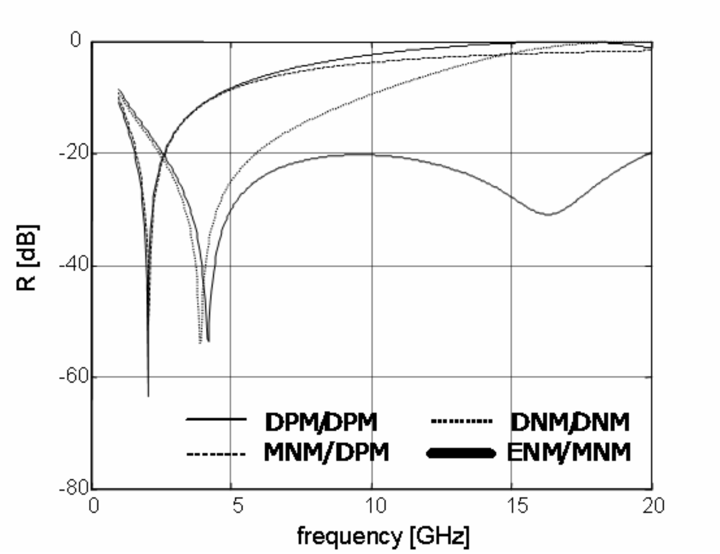

Figure 7.6: Reflection coefficient of the TSS including the different metafilm pairs A, B, D, E in Table 7.2 computed for $\varepsilon_{rL} = 8$.

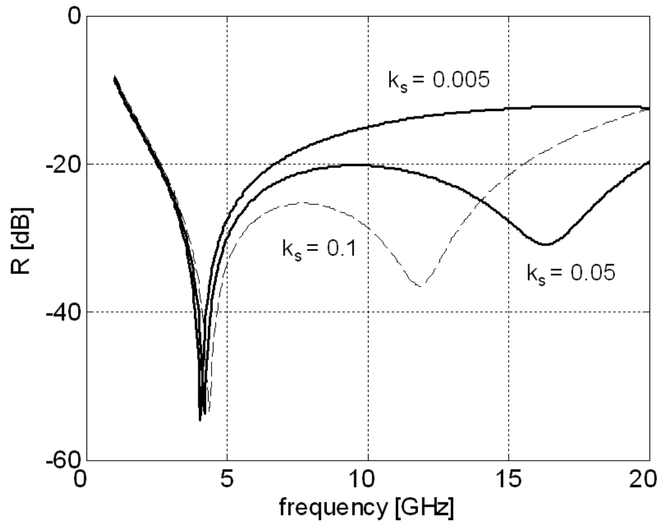

Figure 7.7: Reflection coefficient of the broad-band TSS including the ENM/MNM bilayer and with $\varepsilon_{rL} = 8$, for different values of the parameter k_S.

TSS and on the available technology for material fabrication, different electrical and geometrical configurations of the TSS can be designed. As an example, three different designs of bilayer spacers, producing the same EM response with the first resonance frequency at 2.6 GHz, are reported in Table 7.4.

7.3 Design optimization of metamaterial screens for EMI suppression

The design of multilayer EMAS requires the use of numerical tool [56], [57]. In fact, analytical procedures are not applicable, due to the large number of variables involved. The solution of optimization problems is not unique in general and cannot be obtained in close form, especially in case the physical parameters can assume both positive or negative values. An approach based on genetic algorithm (GA) optimization is investigated, and a complete design tool is developed. The procedure applies to a wide variety of materials, including carbon fiber composites, epsilon-negative materials (ENM), munegative materials (MNM), double-

Table 7.4: Electrical and geometrical parameters of TSSs including metafilm, having the configuration shown in fig. 7.3.

TSS 1	TSS 2	TSS 3
$k_S = 0.05$	$k_S = 0.05$	$k_S = 0.05$
$\|\varepsilon_{r1}\| = 0.1$	$\|\varepsilon_{r1}\| = 1$	$\|\varepsilon_{r1}\| = 0.5$
$\|\mu_{r2}\| = 1$	$\|\mu_{r2}\| = 10$	$\|\mu_{r2}\| = 5$
$d_1 = d_2 = 2.90$ mm	$d_1 = d_2 = 290$ mm	$d_1 = d_2 = 581$ mm
$d_{tot} = 6.24$ mm	$d_{tot} = 1.02$ mm	$d_{tot} = 1.60$ mm

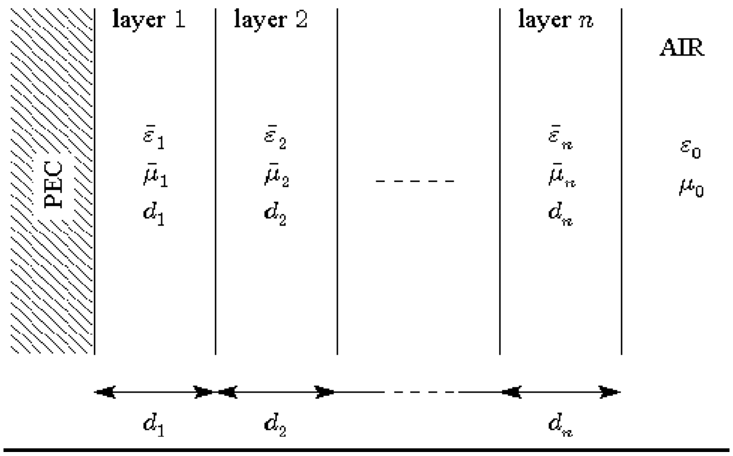

Figure 7.8: Representation of a generic multilayer EMAS.

negative materials (DNM). In particular, the tool provides the optimum combination of material parameters starting from constraints on the value of the reflection coefficient and the overall panel thickness. Numerical experiments demonstrate that very thin absorbers having sub-wavelength thickness can be obtained. In particular, for some combination of material parameters a two-layer slab of only 125 μm in thickness is designed, with an attenuation of at least 15 dB over the entire 6 GHz-18 GHz band. The design approach and the optimization procedure are fully detailed in the following.

7.3.1 Generality

Genetic algorithms (GAs) are methods for solving both constrained and unconstrained optimization problems, that are based on natural selection, the process that drives biological evolution [58]. Let's consider the EMAS having the structure of Fig. 7.8, in which n is the number of layers, d_i is the thicknesses of the i-th layer,

$$\overline{\varepsilon_i} = \varepsilon_i^{'} + j\varepsilon_i^{''} \quad , \quad \overline{\mu_i} = \mu_i^{'} + j\mu_i^{''} \tag{7.32}$$

are the effective complex permittivity and permeability of the i-th layer. The objective of the design process is to define the configuration of the panel, so that in a given frequency range is characterized by a reflection coefficient Γ_{dB} always below a given mask M_{dB}. The problem is solved by applying an iterative optimization procedure based on GA. At the k-th iteration, the generic h-th ($h = 1, ...m$) individual is defined by the $5n$-dimensional vector of real numbers given by:

$$I(h,k) = [\varepsilon_i^{'}(h,k), \varepsilon_i^{''}(h,k), \mu_i^{'}(h,k), \mu_i^{''}(h,k), d_i(h,k)_{\text{i=1,n}}] \tag{7.33}$$

At the same iteration, the population $P(k)$ used by the GA procedure is defined by a matrix of m individuals:

$$P(h,k) = [I(1,k), ..., I(m,k)] \tag{7.34}$$

.

The diversity between individuals is defined as their distance in the $5n$-dimensional space. It is very important that the individuals are well spread all over the space in order to improve the possibility to find a solution to the problem. The choice of the individuals at the first iteration can be completely random or it can be constrained by geometrical or electromagnetic bounds, or by data derived from preliminary analysis or from measurements, in order to define a selected pool of individuals that enable the algorithm to converge faster to the solution. The fitness function for this application is a function of frequency and it is defined by:

$$F = \Gamma_{dB} - M_{dB} \tag{7.35}$$

where Γ_{dB} is the reflection coefficient in dB and M_{dB} is a given mask.

The GA modifies the initial population of individuals, and creates a series of new populations, each of them is indicated as a different generation of the initial one, evolving toward an optimum solution. At each step, the GA selects individuals from the current population to be parents and uses them to generate the next generation individuals, called offspring. The selection of the parents can be made in different ways, based on the computation of a fitness value F_v that represents the maximum difference between Γ_{dB}, calculated in the whole frequency range of interest for each individual, and the desired value M_{dB}. The minimum F_v among the current population is called best fitness value BF_v, and it is used at each iteration for the choice of the parents and the generation of the offspring according to the following procedure. At first, individuals associated to the BF_v are named elite and are passed unmodified to the next generation. Next, all the other individuals become parents and produce offspring (new individuals necessary to complete the population matrix) either by considering random changes to a single parent (mutation) or by combining the vector entries of a pair of parents (crossover). A crossover fraction XoF can be defined to account for the percentage of individuals, excluding the elite, that is generated by mutation or crossover. When offspring is performed only by mutation or only by crossover, it is set $XoF = 0$ or $XoF = 1$, respectively. The process is iterated until one or more stopping criteria, generally based on the BF_v of the current population or on the time elapsed since the start of the GA run, is met. An outline of the core procedure is depicted in Fig. 7.9.

7.3.2 Critical aspects for the specific application

Realizing and using a GA requires both a high programming competence and a sufficiently deep knowledge of the basis of biological evolution. The application presented in the following, uses the Genetic Algorithm and Direct Search Toolbox (GADS) of the MATLAB environment, as it supplies a basic GA core extremely

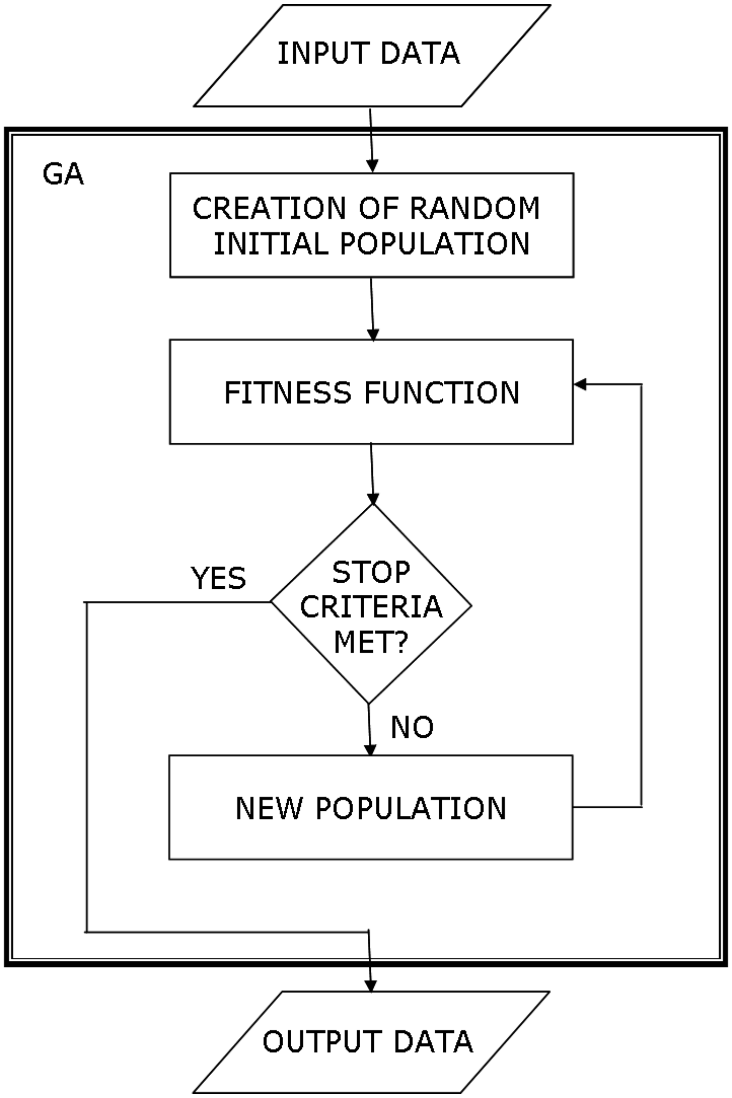

Figure 7.9: Flow diagram of the core GA procedure.

flexible and highly optimized for the processing of the great amount of data involved. The critical aspects about the development of the remaining code used in this paper are: the correct choice of the parameters on which the GA operation is based; to avoid that the algorithm is trapped into local minima, leading to the erroneous conclusion that there is no solution to the problem. Like all the stochastic global algorithms, GAs cannot guarantee the reaching of a global optima but, if they are properly tuned, they can assure a high probability to find the best solution in a reasonable amount of time. Such a tuning implied a trade-off between two opposite aspects of the GA behaviour, deeply connected to the way the current population breeds. Actually, the fact that offspring of the current population is generated by crossover implies that the population is projected towards the presently more promising region of the search space. At the same time, offspring by mutation forces the individuals to explore randomly regions of the solution space that are external to the ones already analysed, thus helping avoiding the stagnation in a local optima. In order to reasonably account for mutation and crossover, two different procedures were implemented: the preliminary search (PS) and the deep search (DS) respectively. The PS executes 20 runs of the GA for each XoF value between 0 and 1 with increments of 0.2 using the default (and computationally lighter) values for the GA parameters, returning the statistical distribution of the BF_v over the complete XoF range. If no solution is individuated by this procedure, a more intensive (thus computationally heavier) search may be performed with the DS on a restricted and promising XoF range chosen on the basis of the PS results. The setting of the GA's parameters for the DS is made essentially to avoid an excessive diversity loss and the resulting risk of stagnation in a local optima. To obtain such a behaviour while guaranteeing the convergence toward a solution, subpopulations and migrations are used and more "random" algorithms for the selection of the parents and the crossover and mutation mechanisms adopted.

7.3.3 Design of thin absorbing screens including metamaterials

The described GA optimization procedure is applied as an example to the design of EMAS including metamaterial layers. The EM modeling of the metamaterial as an effective medium is out of the purpose of this paper. Therefore, in the following it is assumed that individuals are represented by vectors having the structure introduced in 7.32. The dimension of the vector is $5n$, n being the number of layers of the EMAS. Notice that also n is an unknown of the problem, and its value will result from the optimization procedure. As a first example, the GA procedure is applied considering the constrains:

$$\begin{array}{ll} -20 \leq \varepsilon_i^{'} \leq 20 \quad 0 \leq \varepsilon_i^{''} \leq 20 & \\ & i = 1, n \\ -80 \leq \mu_i^{'} \leq 80 \quad 0 \leq \mu_i^{''} \leq 20 & \end{array} \tag{7.36}$$

Moreover, the overall thickness of the panel should be less than 1 mm, and the minimum thickness of each layer greater than 100 nm. Figs. 7.10,7.11 show the frequency spectrum of the reflection coefficient of the optimum panel obtained applying the mask:

$$M_1 = \begin{cases} -15, & \text{for } 6 \leq f < 12 \text{ GHz} \quad (7.37a) \\ -20, & \text{for } 12 \leq f \leq 18 \text{ GHz}. \quad (7.37b) \end{cases}$$

The obtained EMAS has two layers constituted by an epsilon negative material (ENM) and a double negative material (DNM). Fig. 7.12 shows the computed BF_v as function of the cross-over fraction. Such preliminary search is performed in order to verify the possibility that a solution for the specific problem of interest exists, and in order to define the optimum value of the crossover fraction for generation of parents in the GA. It results that the minimum BF_v is obtained for $XoF = 0.2$. The upper dotted line represents the maximum allowed BF_v, whereas the dotted lower line is the target BF_v below which we want to find the solution. Such value is set equal to -2 dB. Fig. 7.13 reports the values of the panel parameters resulting from the GA search.

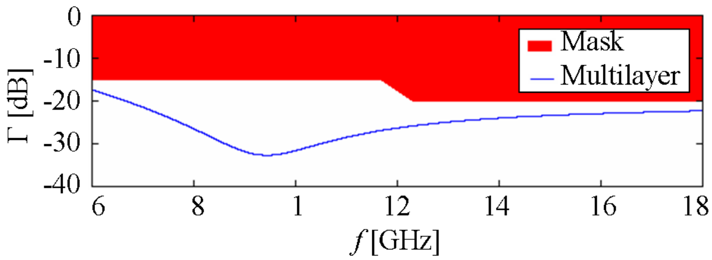

Figure 7.10: Frequency spectra of Γ_{dB} of a two-layer panel with overall thickness of 125 μm, and mask M_1 for 1 GHz $\leq f < 18$ GHz.

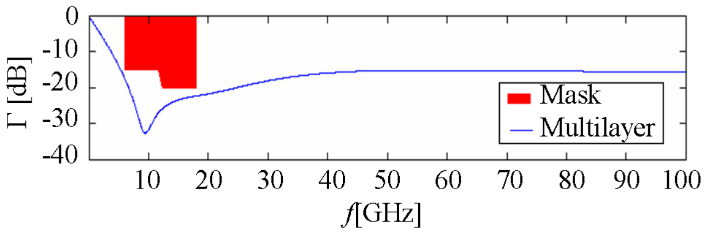

Figure 7.11: Frequency spectra of Γ_{dB} of a two-layer panel with overall thickness of 125 μm, and mask M_1 for 1 GHz $\leq f < 100$ GHz.

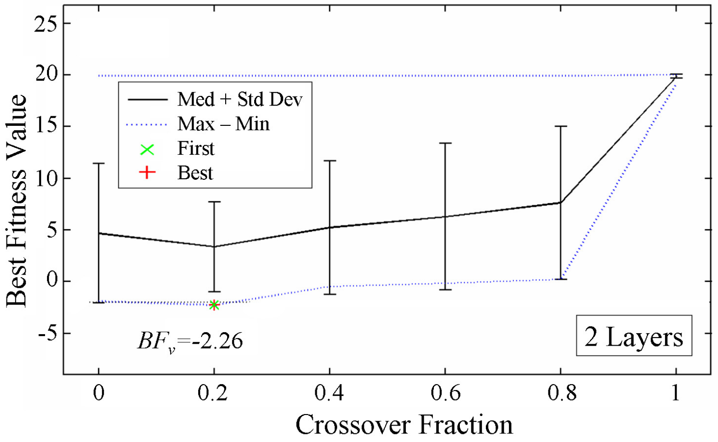

Figure 7.12: Best fit value as function of the crossover fraction resulting from the preliminary search of a bilayer having maximum overall thickness of 125 μm and reflection coefficient always below mask M_1.

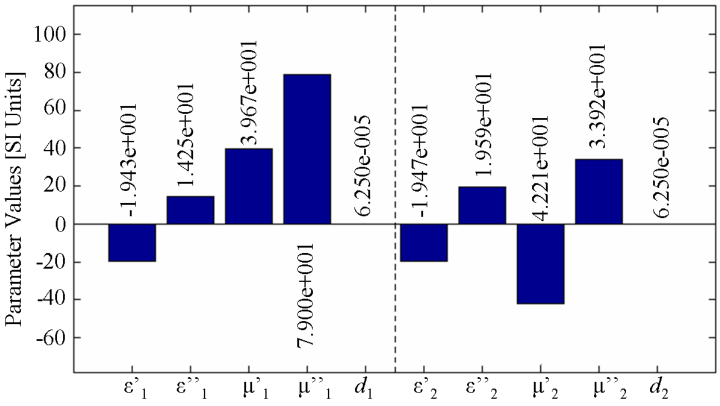

Figure 7.13: Parameters of the two-layer best panel (ENM-DNM) having thickness of 125 μm, constrained by mask M_1.

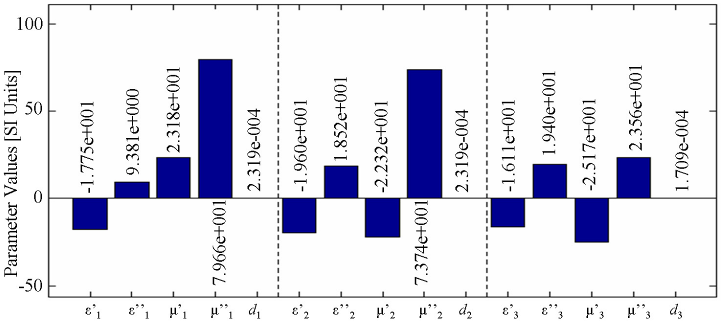

Figure 7.14: Parameters of the three-layer best panel (ENM-DNM-DNM) having thickness of 634.7 μm, constrained by mask M_2.

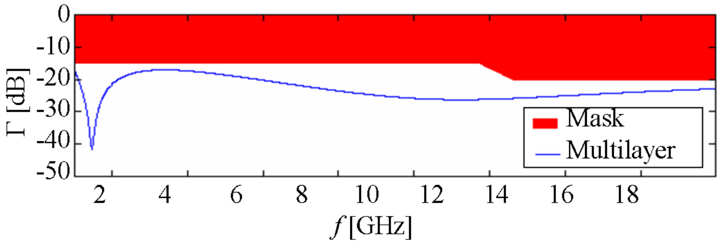

Figure 7.15: Frequency spectra of Γ_{dB} of the three-layer panel with thickness of 634.7 μm and design mask M_2 for 1 GHz $\leq f \leq 18$.

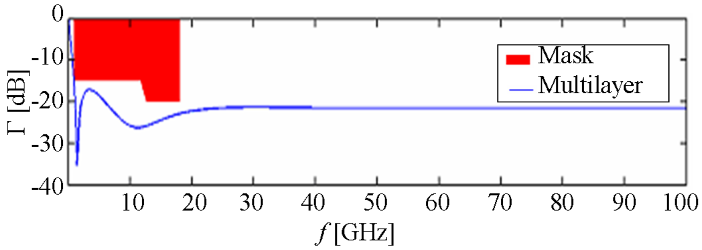

Figure 7.16: Frequency spectra of Γ_{dB} of the three-layer panel with thickness of 634.7 μm and design mask M_2 for 1 GHz $\leq f \leq 100$.

A further investigation is performed applying the mask:

$$M_2 = \begin{cases} -15, & \text{for } 1 \leq f < 12 \text{ GHz} \quad (7.38a) \\ -20, & \text{for } 12 \leq f \leq 18 \text{ GHz.} \quad (7.38b) \end{cases}$$

The resulting panel has three metamaterial layers (ENM-DNM-DNM) and thickness of 634.7 μm. The electrical and geometrical parameters of each layer are reported in Fig. 7.14. The amplitude frequency spectra of the reflection coefficient of the panel is reported in Fig. 7.15 and 7.16, and compared with mask M_2. It should be noted that the implemented GA procedure is very efficient. The computational time on a laptop computer is within the hour. It is also pointed out that the obtained result is absolutely revolutionary because the GA search performed applying the constraints of maximum panel thickness of 1 mm and masks M_1 or M_2 did not provide any solution when traditional materials were considered.

7.4 Conclusion

This Chapter describes an equivalent circuit approach for the design of innovative electrically thin absorbing screens, realized by a lossy dielectric as lossy sheet, a metafilm bilayer as spacer, and a PEC as back surface. The proposed method allows to quantitatively define the electrical parameters and thickness of the layers of the TSS in order to obtain the desired EM absorption properties. The obtained results demonstrate that the use of layers made by materials having negative electrical parameters is not required in order to realize a narrow-band TSS. At the contrary a broadband TSS can be only realized by using as spacer the ENM/MNM bilayer. An approach based on a genetic algorithm (GA) optimization procedure is then developed. The procedure is able to extract the electrical and geometrical parameters of each layer of the screen, starting from constraints on the maximum allowed reflection coefficient in a given frequency range, and the maximum thickness of the panel. The tool is developed and implemented. The critical aspect related to the presence of local minima is dealt by properly defining the strategy for creation and generation of tentative solution vectors to be used in the optimization process. The application of the tool to multilayer EMAS including metamaterials demonstrated that very thin absorbers, having sub-wavelength dimensions can be designed. For some combination of material parameters a bilayer of only 125 μm in thickness is obtained, enforcing maximum reflection coefficient of -15 dB over the entire frequency range from 6 GHz-18 GHz. It should be also pointed out however, that the numerical experiments of this paper deal only with ideal metamaterials: actually further GA searches should be done considering that, at the current state of art, negative materials behaviour can be obtained only within narrow selected frequency range. This is the scope of further studies. Moreover, an other critical aspect related to the real exploitation of the result of the presented analysis concerns the realization of thin layer of metamaterial. To this purpose, the powerful of nanotechnology should be investigated.

Chapter 8

Conclusions

Chapter 9

Acronyms

List of Figures

List of Tables

Bibliography

[1] M. Crawford and G. Koepke, *Design, evaluation, and use of a reverberation chamber for performing EM susceptibility/ vulnerability measurements — NBS Tech. Note 1092*. NBS, Boulder, CO, 1986.

[2] P. Corona, J. Ladbury, and G. Latmiral, “Reverberation-chamber research-then and now: a review of early work and comparison with current understanding,” *IEEE Transactions on Electromagnetic Compatibility*, vol. 44, no. 1, pp. 87–94, Feb. 2002.

[3] D. A. Hill, *Electromagnetic Theory of Reverberation Chambers — NIST Tech. Note 1506*. NIST, Boulder, CO, Dec. 1998.

[4] P. Corona, A. D. Bonitatibus, and E. Paolini, “In order to evaluate in reverberating chambers the radiated power of transmitting equipments,” in *Proc. IEEE Int. Symp. Electromagnetic Compatibility*, 1981, pp. 1–3.

[5] IEC-CENELEC, *Radio-interference measurements and statistical methods*, 2003, no. 61000.

[6] J. Ladbury, G. H. Koepke, and D. G. Camell, “Evaluation of the nasa langley research center mode-stirred chamber facility,” *NIST Technical Note 1508*, 1998.

[7] J. G. Kostas and B. Boverie, “Statistical model for a mode-stirred chamber,” *IEEE Transaction on Electromagnetic Compatibility*, vol. 33, pp. 366–370, 1991.

[8] A. Papoulis, *Probability, Random Variables, and Stochastic Processes*. McGraw Hill, 1965.

[9] G. Matthaei, L. Young, and E. M. T. Jones, *Microwave Filters, Impedance-Matching Networks, and Coupling Structures*. Boston, MA: Artech House, 1980.

[10] J. M. Dunn, "Local, high-frequency analysis of the fields in a mode-stirred chamber?" *IEEE Trans. Electromagnetic Compatibility*, vol. 48, no. 2, pp. 304–310, May 2006.

[11] S. Greco, A. Ferretti, and M. S. Sarto, "EMC testing of wireless systems by the use of reverberation chambers," in *EMC Europe Workshop*, Sept. 2005, pp. 322–325.

[12] *National Instruments, website: http://www.ni.com*.

[13] *Testing and Measurement Techniques — Reverberation Chamber Test Methods*. IEC 61000-4-21, 2005.

[14] T. Nguyen, "RF loading effects of aircraft seats in an electromagnetic reverberating environment," in *Proceedings of 18th Digital Avionics Systems Conference*, vol. 2, Oct. 1999, pp. 10.B.5–1–10.B.5–7.

[15] M. O. Hatfield, D. M. Johnson, T. A. Loughry, A. R. Ondrejka, R. T. Johnk, G. J. Freyer, and M. B. Slocum, *Phase II: Demonstration test of the electromagnetic reverberation characteristics of a transport size aircraft — Report No. NSWCDD/TR- 97/84*. NS WC Dahlgren Division, 1997.

[16] M. O. Hatfield, "A calibration procedure for reverberation chambers," in *IEEE International Symposium*, vol. 2, Aug. 2000, pp. 621–626.

[17] K. R. Goldsmithm and P. A. Johnson, "Design, construction, computational EM modelling, and characterisation of an aircraft sized reverberation chamber and stirrer," in *Digital Avionics Systems Conference*, vol. 1.

[18] D. R. Kemp, “A proposed HIRF test facility for aircraft testing,” in *Digital Avionics Systems Conference*, vol. 1, Oct. 1997, pp. 4.2–22–4.2–25.

[19] G. J. Freyer and M. O. Hatfield, “Aircraft test application of reverberation chambers,” in *IEEE International Symposium on Electromagnetic Compatibility*, Aug. 1994, pp. 491–496.

[20] D. A. Hill, M. T. Ma, A. R. Ondrejka, M. L. Crawford, and R. Johnk, “Aperture excitation of electrically large, lossy cavities,” *IEEE Trans. on EMC*, vol. 36, no. 3, Aug. 1994.

[21] C. L. Holloway, D. A. Hill, J. M. Ladbury, and G. Koepke, “Requirements for an effective reverberation chamber: unloaded or loaded,” *IEEE Trans. Electromagnetic Compatibility*, vol. 48, no. 1, pp. 187–194, Feb. 2006.

[22] M. D’Amore, D. A. Lampasi, S. Pisa, L. Podestà, M. S. Sarto, and A. Tamburrano, “Feasibility of electromagnetic detection of cellular phones aboard aircraft,” in *Proc. EMC Europe Workshop on Electromagnetic Compatibility of Wireless Systems*, Sept. 2005, pp. 45–48.

[23] D. A. Hill, “Wave integral representation for fields in reverberation chambers,” *IEEE Trans. on EMC*, vol. 40, no. 3, pp. 209–217, Aug. 1998.

[24] S. Greco, D. A. Lampasi, and M. S. Sarto, “Electromagnetic characterization of a field sensor for the localization of gsm cellular phones aboard an aircraft,” *IEEE Transactions on EMC*, vol. 50, no. 3, pp. 755–758, Aug. 2008.

[25] L. Podestà, et al., *Dispositivo di rilevamento di condizioni di funzionamento di telefoni cellulari (in Italian)*. patent n. RM2003A000231.

[26] S. Pisa, M. Cavagnaro, E. Piuzzi, and V. Lopresto, “Numerical-experimental validation of a GM-FDTD code for the study of cellular phones,” *Microwave and Optical Technology Letters*, vol. 47, no. 4, pp. 396–400, Nov. 2005.

[27] G. Kuriger, H. Grant, A. Cartwright, and D. Heirman, “Investigation of spurious emissions from cellular phones and the possible effect on aircraft navigation equipment,” *IEEE Trans. Electromagnetic Compatibility*, vol. 45, no. 2, pp. 79–85, May 2003.

[28] B. Strauss, M. G. Morgan, J. Apt, and D. D. Stancil, “Unsafe at any airspeed? — cellphones and other electronics are more of a risk than you think,” *IEEE Spectrum*, vol. 43, no. 3, pp. 44–49, Mar. 2006.

[29] E. Ross, *Personal Electronic Devices and Their Interference With Aircraft Systems, NASA/CR–2001–210866*. ViGyan, Inc., Hampton, Virginia, June 2001.

[30] *Guidance on allowing transmitting portable electronic devices (T-PEDs) on aircraft*. Radio Technical Commission for Aeronautics (RTCA), July 2004.

[31]

[32] K. Muller, *Use of electronic devices aboard aircraft*. Research Report FE-Nr. L-5/98-50 173/98.

[33] S. Greco and M. S. Sarto, “Low-Q reverberation chamber to reproduce aircraft-like EM environment,” in *Proc. EMC Europe 2006*, Sept. 2006, pp. 502–507.

[34] M. D’Amore, S. Greco, D. A. Lampasi, L. Podestà, and M. S. Sarto, “Electromagnetic detection system of cellular phones aboard aircraft,” in *EMC Europe Workshop*, June 2007, pp. 1–4.

[35] K. Malaric, J. Bartolic, and R. Malaric, “Measurement of GSM phone emission,” in *Proc. 21st IEEE Instr. Meas. Tech. Conf. IMTC*, vol. 1, May 2004, pp. 263–266.

[36] D. A. Lampasi and L. Podestà, “Distributed network for accurate indoor localization of mobile phones,” in *Proc. 24th IEEE Instr. Meas. Tech. Conf. IMTC*, May 2007, pp. 1–6.

[37] M. Laurenti and M. S. Sarto, “3D-FDTD modelling of the EM field distribution produced by portable electronic devices aboard aircraft,” in *EMC Europe Workshop*, Sept. 2005, pp. 33–36.

[38] M. P. Robinson, J. Clegg, and A. C. Marvin, “Radio frequency electromagnetic fields in large conducting enclosures: effects of apertures and human bodies on propagation and field-statistics,” *IEEE Trans. Electromagnetic Compatibility*, vol. 48, no. 2, pp. 304–310, May 2006.

[39] D. L. Herrick, *Apparatus and method for locating cellular telephones*. US Patent 5512908, Apr. 1996.

[40] D. L. Herrick, et al., *Apparatus and method for finding a signal emission source*. US Patent 6580915, Apr. 1997.

[41] M. W. Kroll, *Aircraft internal EMI detection and location*. US Patent 6580915, June 2003.

[42] M. S. Aspesi, et al., *EMI source detector*. US Patent 5543779, Aug. 1996.

[43] IEEE-EMC-Society, *IEEE Standard Method for Measuring the Effectiveness of Electromagnetic Shielding Enclosures*, 1997, no. 299.

[44] M. S. Sarto, F. Sarto, M. C. Larciprete, M. Scalora, M. D’Amore, C. Sibilia, and M. Bertolotti, “Nanotechnology of transparent metals for radio frequency electromagnetic shielding,” *IEEE Trans. Electromagnetic Compatibility*, vol. 45, no. 4, pp. 586–594, Nov. 2003.

[45] T. A. Loughry, *Frequency stirring: An alternate approach to mechanical mode-stirring for the conduct of electromagnetic susceptibility testing–Report No. PL–TR–91–1036*. Phillips Laboratory–Kirtland–AFB (NM), Nov. 1991.

[46] *Testing and Measurement Techniques — Reverberation Chamber Test Methods*. IEC 61000-4-21, 2003.

[47] C. Holloway, J. Ladbury, J. Coder, G. Koepke, and D. Hill, “Measuring shielding effectiveness of small enclosures/cavities with a reverberation chamber,” in *IEEE International Symposium on EMC*, July 2007.

[48] S. Greco and M. S. Sarto, “New hybrid mode-stirring technique for se measurement of enclosures using reverberation chambers,” in *IEEE International Symposium on EMC*, July 2007.

[49] A. C. Marvin, Y. Cui, and D. A. Lampasi, “Finding the representative contents for the measure of shielding effectiveness,” in *IEEE Int. Symp. on EMC*, Aug. 2005.

[50] W. W. Salisbury, *Absorbent body for electromagnetic waves*. US. Patent 2 599 944, 1952.

[51] K. J. Vinoy and R. M. Jha, *Radar Absorbing Materials*. Boston: Kluwer Academic Publishers, 1996.

[52] R. W. Ziolkowski and N. Engheta, “Metamaterial special issue introduction,” *IEEE Transactions on Antennas and Propagation*, vol. 51, no. 10, pp. 2546–2549, Oct. 2003.

[53] A. Alù, F. Bilotti, N. Engheta, and L. Vegni, “A thin absorbing screen using metamaterial complementary pairs,” in *ICEAA 2005*, Sept. 2005.

[54] N. Engheta, “An idea for thin subwavelength cavity resonators using metamaterials with negative permittivity and permeability,” *IEEE Antennas Wireless Propagat. Lett.*, vol. 1, no. 1, pp. 10–13, 2002.

[55] S. Zouhdi, A. H. Sihvola, and M. Arsalane, “Advances in electromagnetics of complex media and metamaterials.” Eds. Norwell, MA: Kluwer–NATO Science Series, p. 19.

[56] B. Chambers and A. Tennant, “Optimised design of Jaumann radar absorbing materials using a genetic algorithm,” *Radar, Sonar and Navigation*, pp. 23–30, Feb. 1996.

[57] S. K. Goudos and J. N. Sahalos, "Design of broadband radar absorbing materials using particle swarm optimization," in *EMC Europe Int. Symposium*, Sept. 2006.

[58] G. V. Eleftheriades and K. G. Balmain, *Negative-Refraction Metamaterials: Fundamental Principles and Applications*. John Wiley and Sons and IEEE Press, June 2005.